REPORT

SOLAR SYSTEM FORMATION

Lifetime of the solar nebula constrained by meteorite paleomagnetism

Huapei Wang,[1]*† Benjamin P. Weiss,[1] Xue-Ning Bai,[2] Brynna G. Downey,[1] Jun Wang,[3] Jiajun Wang,[3] Clément Suavet,[1] Roger R. Fu,[1] Maria E. Zucolotto[4]

A key stage in planet formation is the evolution of a gaseous and magnetized solar nebula. However, the lifetime of the nebular magnetic field and nebula are poorly constrained. We present paleomagnetic analyses of volcanic angrites demonstrating that they formed in a near-zero magnetic field (<0.6 microtesla) at 4563.5 ± 0.1 million years ago, ~3.8 million years after solar system formation. This indicates that the solar nebula field, and likely the nebular gas, had dispersed by this time. This sets the time scale for formation of the gas giants and planet migration. Furthermore, it supports formation of chondrules after 4563.5 million years ago by non-nebular processes like planetesimal collisions. The core dynamo on the angrite parent body did not initiate until about 4 to 11 million years after solar system formation.

Theoretical studies suggest that magnetic fields mediated the global evolution and structure of protoplanetary disks by transporting angular momentum and driving stellar accretion (1). They also directly influence disk dynamics by generating turbulence and launching disk winds (1). These processes strongly affect the sequence of planet formation, including the formation of chondrules (2) and the accretion of planetesimals (3). Recent astronomical observations (4) have provided evidence for large-scale magnetic fields in protoplanetary disks, and recent paleomagnetic measurements of chondrules from the Semarkona meteorite (5) have found that the midplane solar nebula magnetic field was 5 to 50 µT in the terrestrial-planet region sometime between ~1 and 3 million years (My) after solar system formation [defined here as the crystallization age of calcium- and aluminum-rich inclusions (CAIs) at 4567.30 ± 0.16 million years ago (Ma) (6)]. These field intensities are consistent with those predicted for typically observed protostellar accretion rates of ~10^{-8} solar masses ($M_\odot$) per year (7). Because the presence of ionized nebular gas is necessary to sustain magnetic fields against diffusive decay, these data indicate that the nebula persisted for at least 1 to 3 My after solar system formation.

It remains unknown when the solar nebula magnetic field and the gaseous nebula itself dispersed. The dispersal times of the field and nebula set the time scale for stellar accretion, the formation of the gas giants, and the epoch of large-scale planetary migration and have major implications for dust dynamics and disk structure (8), the final sizes eccentricities of the terrestrial planets (9), and the viability of hypothesized chondrule and planetesimal formation mechanisms involving nebular gas or magnetic fields. For example, disk gravitational instabilities could in principle have formed the giant planets in <0.1 My, while core accretion is favored by longer (several to perhaps >10 My) time scales (10).

There are currently no direct, accurately dated meteoritic constraints on the lifetime of the nebula and nebular magnetic fields in the early solar system (11, 12). Astronomical observations have inferred that half of all protoplanetary disks around Sun-like young stellar objects (YSOs) disperse somewhere between ~2 and 6 My after formation (13, 14), with this large age uncertainty due to difficulties in determining YSO ages (13). In addition to this uncertainty in the median disk lifetime, it is also unknown where our own solar system lies in the distribution of disk lifetimes. To characterize late-stage nebular magnetism and constrain the lifetime of the early solar nebula, we studied the paleomagnetism of angrites, a group of ancient basaltic achondritic meteorites (15) containing fine grains of ferromagnetic magnetite grains. Paleomagnetism combined with radiometric ages can provide a direct and precisely dated measurement of the nebular field strength in the terrestrial planet–forming region.

Because angrites are samples of a differentiated planetesimal that formed an early metallic core (15), their paleomagnetism also offers the opportunity to characterize planetesimal core dynamo

activity. The small radii (~10^2 km) of planetesimals allow the study of dynamo generation in bodies smaller than planets that have distinct thermal evolution parameters (16). However, a key unknown about planetesimal dynamos has been their onset time. Some theoretical studies have suggested that they might occur instantaneously after large-scale melting (17, 18), whereas others have argued that dynamos should be delayed by several to tens of My or longer (19, 20). Paleomagnetic measurements on angrites of different ages could establish the temporal history of the angrite parent body dynamo and, in particular, its onset time.

Angrites are among the oldest known and most pristine planetary igneous rocks and have very precisely dated formation ages due to their high U/Pb compositions (15). We studied three volcanic angrites: D'Orbigny, Sahara 99555, and Asuka 881371, which have pyroxene Pb/Pb ages of 4563.37 ± 0.12 My (21), 4563.54 ± 0.14 My (21), and 4562.4 ± 1.6 My (15), respectively. Because these meteorites cooled rapidly (10° to 50°C/hour) (22), they should have acquired thermoremanent magnetization (TRM) just ~3.8 My after solar system formation if an ambient field was present. Angrites are thought to have originated from the inner solar system [<~5 astronomical units (au)] (23) and so should provide field records from the midplane of the terrestrial planet–forming region. We also analyzed the younger plutonic angrite Angra dos Reis, which has a pyroxene Pb/Pb age of 4556.51 ± 0.11 My (21) and cooled at >1000°C/My (24). All of these meteorites are essentially unshocked, unbrecciated, and unmetamorphosed since final cooling (15). In particular, at least D'Orbigny and Angra dos Reis have never subsequently been heated above the ~500°C U/Pb phosphate closure temperature (21, 24, 25), and all three angrites have whole-rock (U-Th)/He ages within the uncertainties of their Pb/Pb pyroxene formation ages (26). Rock magnetic measurements and synchrotron transmission x-ray microscopy (18, 27) demonstrate that the major magnetization carriers in angrites are pseudo–single domain magnetite and titanomagnetite grains (and possibly also iron sulfides in Angra dos Reis). Such magnetite has higher coercivity (i.e., resistance to being remagnetized by applied fields) and is more stable during laboratory heating than the multidomain iron-nickel minerals that dominate most basaltic achondrite groups. Recovered the day after it fell to Earth (15), Angra dos Reis largely avoided weathering after landing and remagnetization by collectors' hand magnets.

A previous paleomagnetic study of D'Orbigny, Asuka 881371, and Angra dos Reis identified natural remanent magnetization (NRM) interpreted as evidence for dynamo action on their parent planetesimal (18). This conclusion rested largely on the high-fidelity record in Angra dos Reis, which was the only large meteorite studied that was not affected by magnet overprints. However, the previous study was unable to employ thermal demagnetization, a key technique for isolating primary magnetization. To address this limitation, we conducted thermal demagnetization and thermal

[1]Department of Earth, Atmospheric and Planetary Sciences, Massachusetts Institute of Technology, Cambridge, MA, USA. [2]Institute for Theory and Computation, Harvard-Smithsonian Center for Astrophysics, Cambridge, MA, USA. [3]National Synchrotron Light Source-II, Brookhaven National Laboratory, Upton, NY, USA. [4]Museu Nacional, Rio de Janeiro, Brazil.
*Corresponding author. Email: huapei@mit.edu †Present address: China University of Geosciences, 388 Lumo Road, Wuhan, Hubei 430074, China.

paleointensity analyses in the Massachusetts Institute of Technology (MIT) Paleomagnetism Laboratory using a 2G Enterprises Superconducting Rock Magnetometer (SRM) in combination with a recently developed controlled-atmosphere system optimized for the oxygen fugacity conditions of angrite petrogenesis (*28*). We found that for atmospheres with oxygen fugacities ranging from approximately 0 to 1 dex below the iron-wüstite buffer, magnetic carriers in D'Orbigny and Sahara 99555 are largely thermochemically stable during heating up to ~400° to 500°C, whereas Angra dos Reis is largely stable up to ~200°C (supplementary text). We also conducted new nondestructive alternating field (AF) demagnetization, as well as anhysteretic remanent magnetization (ARM), isothermal remanent magnetization (IRM), Shaw (*29*) and Thellier-Thellier (*30*) paleointensity analyses.

Our thermal demagnetization of Angra dos Reis shows that it contains a low-temperature (LT) component that demagnetizes up to ~200°C and a high-temperature (HT) component that unblocks between ~200°C and up to >~300°C. The LT and HT components have similar directions to low-coercivity (LC) (unblocking below ~15 mT) and high-coercivity (HC) (stable to >290 mT) components, respectively, previously identified by AF demagnetization from mutually oriented samples (*18*). A positive fusion-crust baked contact test and the high stability and unidirectionality of the HT/HC component in Angra dos Reis confirm the previous conclusion (*18*) that it is a TRM from primary cooling on the angrite parent body (supplementary materials). Using previously published ARM paleointensity data (*18*), we find that the HT/HC component formed in a field of ~17 µT (with a minimum value of 8.5 µT), consistent with previous results (*18*) (supplementary text).

AF demagnetization revealed that the NRMs of interior samples of D'Orbigny and Sahara 99555 consist of LC components that unblock up to ~4 to 10 mT and ~6 to 10 mT, respectively. Additional AF and thermal demagnetization showed that, after the removal of the LC components, middle-coercivity (MC)/middle-temperature (MT) components unblock up to ~65 mT and ~50 mT and up to ~200°C, respectively (Figs. 1 and 2 and supplementary text) (*31*). High ratios of NRM to IRM (ranging from ~10 to 100%) (tables S2 and S3) over the coercivity range of the LC components and a failed fusion-crust baked contact test for D'Orbigny (*18*) demonstrate that the LC components are likely overprints from hand magnets, as previously suggested (*18*). However, our experiments show that the MC/MT components are also likely overprints because they demagnetize at lower temperatures (Fig. 2, A and B) and AF levels (fig. S8, A and B) than laboratory-applied total ARM with a bias field of 20 µT (an analog for TRM acquired in a ~4-µT field using a TRM/ARM ratio of 5) (supplementary text), which persists to >400°C and >100 mT. Instead, the MT components demagnetize at similar AF levels as a partial thermoremanent magnetization (pTRM) acquired by heating to ~200° to 300°C in a ~10-µT field (Fig. 2, C and D, and table S4).

This indicates that there exists a population of grains with high coercivities (>70 mT) and unblocking temperatures (>200°C) that are essentially unmagnetized. This lack of high-stability NRM is also manifested by the fact that after removal of the MC/MT components, the remaining magnetization directions of mutually oriented samples are collectively scattered (fig. S6) and have weak paleointensities (tables S2 and S3). The low peak 125° to 225°C unblocking temperature of the MT component in D'Orbigny suggests it could be a viscous remanent magnetization (VRM) acquired in Earth's field (supplementary text). On the other hand, the 200° to 425°C peak blocking temperature of the MT component for Sahara 99555 may be too high for it to be a terrestrial VRM, whereas a fusion-crust baked contact indicates that fusion crust–rich samples do not have strong MC components (supplementary text). Instead, the MT component in Sahara 99555 may be a weak thermal overprint from later magmatism on the angrite parent body during the epoch
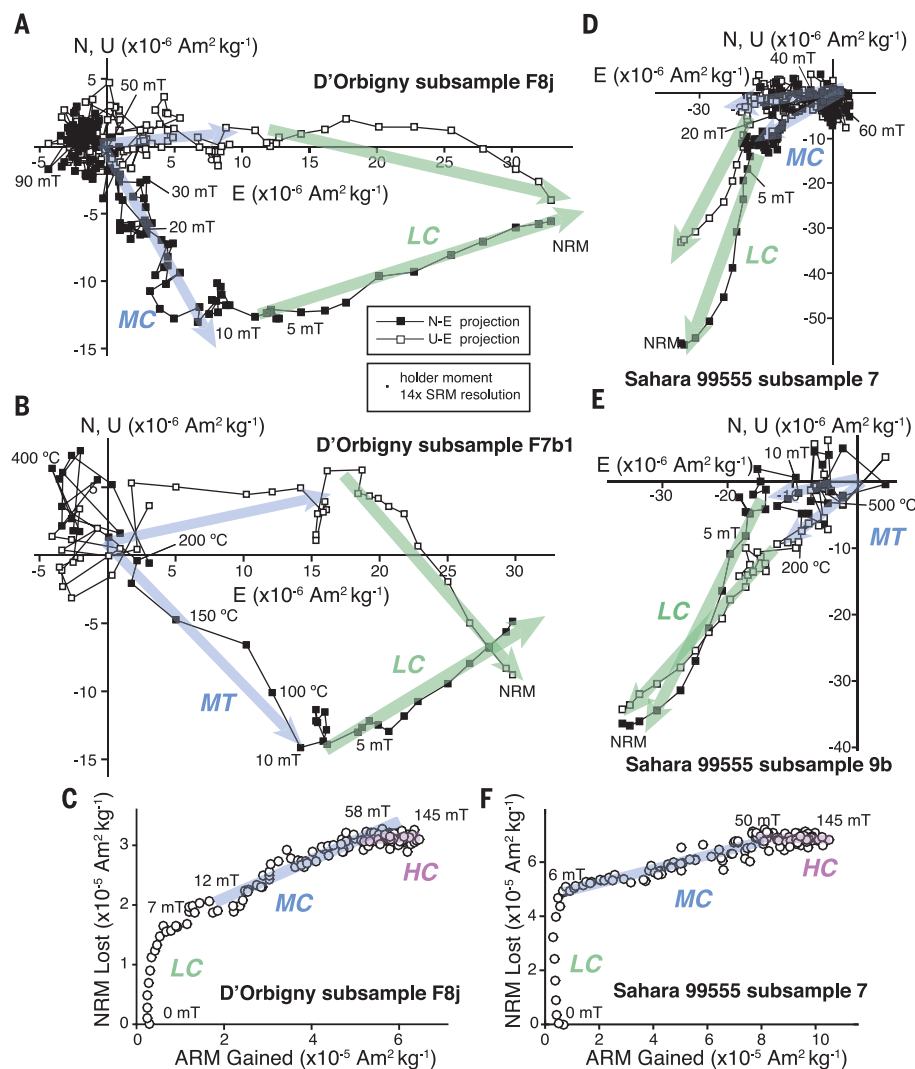
Fig. 1. Demagnetization and paleointensity analyses of volcanic angrites. Two-dimensional projection of the end points of the natural remanent magnetization (NRM) vector during alternating field (AF) demagnetization and thermal demagnetization for D'Orbigny subsamples F8j and F7b1 (**A** and **B**) and Sahara 99555 subsamples 7 and 9b (**D** and **E**). Open (filled) symbols represent projections on the up-east (U-E) and northeast (N-E) planes. Low coercivity (LC) and medium coercivity (MC)/medium temperature (MT) components are labeled with blue and green arrows, respectively. Selected AF and thermal demagnetization steps are labeled. The size of the square in the bottom legend denotes the moment per unit mass of sample (assuming a 100-mg sample) for the sample holder (i.e., GE 124 quartz glass sample mounts and quartz glass sample handling rod) and is ~14 times the intrinsic resolution of the MIT SRM (supplementary text and fig. S5). (**C** and **F**) Anhysteretic remanent magnetization (ARM) paleointensities estimated from NRM lost during AF demagnetization as a function of ARM gained (in a 50-µT bias field) for D'Orbigny subsample F8j (C) and Sahara 99555 subsample 7 (F). Blue and purple lines denote MC and HC magnetization ranges, respectively. The HC paleointensities are 0.4 ± 0.6 µT (C) and −0.1 ± 0.6 µT (D).

of dynamo activity, possibly associated with formation of the plutonic angrites at 11 My after solar system formation (18).

After removal of the MC components by AF demagnetization to 45 to 65 mT, D'Orbigny and Sahara 99555 subsamples contain only directionally unstable HC magnetization that is nonunidirectionally oriented across the parent samples. This magnetization is nevertheless at least two orders of magnitude above the sensitivity of the MIT SRM (supplementary text). Our ARM and IRM acquisition and demagnetization experiments yield HC paleointensity values < ~1 μT (Fig. 1, C and F, and figs. S7 and S11). Based on the vector mean of the subsample paleointensities for D'Orbigny and Sahara 99555, we further estimate an upper limit on the paleointensities from the HC range of 0.3 μT (best estimate), or possibly as high as 0.5 μT considering systematic uncertainties in calibration coefficients associated with the ARM and IRM paleointensity methods (supplementary

text). Our reanalysis of previous AF demagnetization data for Asuka 881371 (18) indicates that the meteorite only contains a weak LC component blocked up to 4.2 mT (likely terrestrial VRM), along with a substantial quantity of unmagnetized grains in an HC range extending up to 81.4 mT with near-zero paleointensity (−0.3 ± 0.5 μT) (supplementary text). The lack of NRM in the most stable grains of the three volcanic angrites indicates that there was no detectable magnetic field during initial cooling below the Curie temperature on the angrite parent body, such that the residual scattered HC magnetization is likely a combination of spurious remanence acquired during demagnetization and spontaneous magnetization. We conclude that, with the advantage now provided by controlled-atmosphere thermal demagnetization, the previous angrite paleomagnetic study (18) inappropriately interpreted MC component of D'Orbigny as a primary TRM acquired on the angrite parent body. Here, we

have shown that of the four studied angrites, only the younger (i.e., plutonic) angrite Angra dos Reis records a dynamo field, which was active by 11 My after solar system formation.

In contrast, we have found that the volcanic angrites D'Orbigny, Sahara 99555, and Asuka 881371 initially cooled in no detectable magnetic field (<0.3 μT) at ~4 My after solar system formation. This suggests that the angrite parent body dynamo field and any crustal remanent fields were absent at this time. Because the angrites cooled through their magnetization acquisition temperature rapidly (over ~10 to 60 hours) relative to the expected time scale of nebular field variations [tens of years at 2 to 3 au from the Sun (32)], they should have been magnetized by any local external fields (33). Given that the angrite parent body was likely rotating [which would produce a measured paleointensity that is on average half that of the actual ambient field strength (5)], this means that the local nebular field, as well as any other external fields from the young Sun and solar wind, was <0.6 μT at that time. Assuming the angrite parent body originated in the region of the present-day asteroid belt and that three meteorites studied here did not cool simultaneously, our three meteorite paleointensity constraints apply to three separate azimuthally distributed locations distributed along the angrite parent body's orbital ellipse in the midplane at ~2 to 3 au from the Sun.

Magnetic field variations on scales comparable to the disk scale height (~0.1 au at 2 to 3 au from the Sun) should be smoothed out on time scales well below an orbital period (several years at this orbital distance) due to the high resistivities expected for protoplanetary disks (supplementary text). Therefore, these near-zero field conditions likely extended throughout the terrestrial planet–forming region at this time. Combining our results with previous chondrule paleointensities (5), this suggests that the nebular field declined from ~5 to 50 μT at ~1 to 3 My to <0.6 μT at ~3.8 My after solar system formation (i.e., at ~4563.46 ± 0.09 Ma given the mean of the pyroxene Pb/Pb ages of D'Orbigny and Sahara 99555) (Fig. 3).

Assuming that magnetic fields played a dominant role in regulating the evolution of the solar nebula, our field constraint indicates that by this time, the Sun's accretion rate dropped to below 10^{-9} $M_\odot$ year^{-1} or possibly even below 10^{-10} $M_\odot$ year^{-1} (with the exact upper limit depending on the nature of the specific magnetic mechanisms that drove accretion earlier in solar system history) (supplementary text). However, in the absence of a nebular magnetic field, purely hydrodynamic processes, such as the vertical shear instability (34), may also contribute to the disk angular momentum transport. Although further studies are needed, our current understanding suggests that these hydrodynamic processes are unlikely to operate efficiently in the inner solar nebula (supplementary text).

The above upper limits on the accretion rate are 10 to 100 times below those inferred from chondrule paleointensity measurements at 1 to 3 My after solar system formation (5). Both
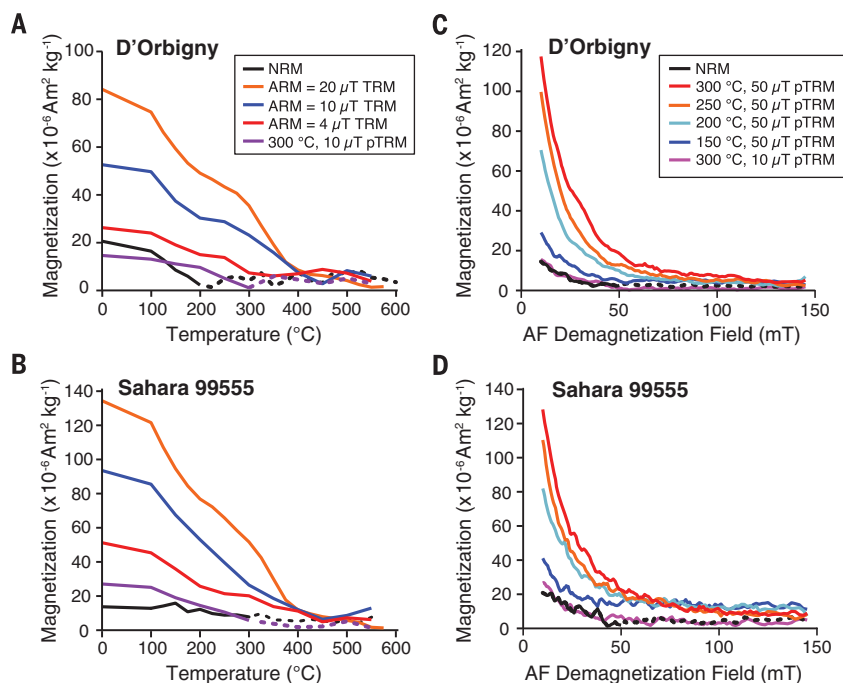
Fig. 2. Demagnetization spectra of volcanic angrites. (**A** and **B**) Thermal demagnetization spectra of NRM (black line) compared with thermal demagnetization of ARM and partial thermoremanent magnetization (pTRM) for D'Orbigny (A) and Sahara 99555 (B). The ARMs were imparted with (i) a 600-μT bias field in a 290-mT alternating field (AF), here divided by a plot scaling factor of 6 to normalize to a 100-μT bias field ARM, which is equivalent to total TRM acquired in a 20-μT bias field (orange line); (ii) a 50-μT bias field in a 260-mT AF, equivalent to total TRM acquired in a 10-μT field (blue line); (iii) a 20-μT bias field in a 260-mT AF, equivalent to total TRM acquired in a 4-μT field (red line). The TRM-equivalent fields for these ARMs were estimated using TRM/ARM = 5. The pTRMs were imparted by cooling from 300°C in a 10-μT bias field (purple line). Demagnetization of NRM was conducted on D'Orbigny and Sahara 99555 subsamples F7b1 and 9b, respectively. Demagnetization of ARM was conducted on (i) F8n and 10a, (ii) F8g1 and 3b1, and (iii) F8g2 and 3b2 for D'Orbigny and Sahara 99555, respectively. Demagnetization of pTRM was conducted on D'Orbigny and Sahara 99555 subsamples F7e and 7, respectively. (**C** and **D**) AF demagnetization spectra of NRM compared to AF demagnetization of pTRM. The pTRMs were acquired in a 50-μT bias field cooling from 300°C (red line), 250°C (orange line), 200°C (light blue line), 150°C (dark blue line), and in a 10-μT bias field cooling from 300°C (purple line). The D'Orbigny subsample is F8e (all curves five-point boxcar-smoothed) and the Sahara 99555 subsample is 7 (all curves three-point boxcar-smoothed). Thermal demagnetization and partial TRM acquisition were conducted in the oxygen fugacity controlled atmosphere. Data for (A) and (B) can be found in data S2.

Fig. 3. Timeline for early solar system magnetism and the solar nebula. Black crosses show magnetic field paleointensity constraints from chondrules from the LL3.00 chondrite Semarkona (5); the volcanic angrites D'Orbigny, Sahara 99555, and Asuka 881371; and the plutonic angrite Angra dos Reis, along with associated uncertainties in age and intensity (vertical and horizontal error bars). Volcanic angrite paleointensities are upper limits only. Time scale is referenced to formation of CAIs, here assumed to be 4567.30 ± 0.16 Ma (6). Blue boxes show inferred constraints on the solar nebula background magnetic field. For Semarkona, the nebular field could be an order of magnitude weaker than the measured chondrule paleointensity measurements (cross) if the local field were enhanced by nebular shocks (5). For volcanic angrites, the nebular field upper limit shown is twice the measured paleointensity upper limits (to correct for rotation of the angrite parent body). Red lines show inferred dispersal time of the solar nebula and the onset time of the angrite parent body dynamo. Green shading indicates equivalent evolutionary stages of young stellar objects (6, 11). Dashed lines indicate the lower limits for two nebular field angular momentum transport mechanisms (magnetorotational instability or large-scale laminar field and magnetized disk winds) at 2.5 au distance from the Sun and assuming a solar accretion rate of $10^{-8}\ M_\odot\ year^{-1}$ (supplementary materials).
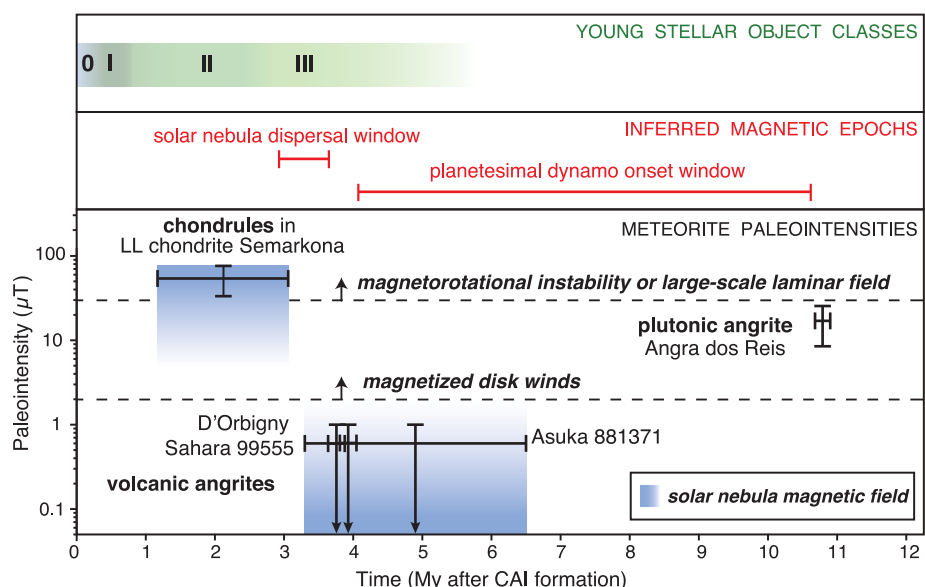
astronomical observations and theory have found that such a decline in accretion rates is associated with near-total dissipation of the nebula, with disk dispersal occurring in just 10^5 years (7). By implication, our near-zero paleointensities therefore suggest that by ~3.8 My after solar system formation, the nebular gas itself in our solar system had similarly dispersed. This is compatible with the observed ~2- to 6-My characteristic lifetimes for extrasolar protoplanetary disks (13, 14).

The timing of the solar nebula dispersal has major implications for the formation of the giant planets. The minimum nebular lifetime of ~1 to 3 My is likely not so short as to require the giant planets to have formed by very rapid mechanisms such as collapse due to gravitational instabilities (10). Nevertheless, the giant planets must still have largely finished accreting their gaseous envelopes by ~3.8 My after solar system formation, which strains some variants of the rock–ice core accretion model (particularly for Uranus and Neptune) (10). The nebula lifetime constraint sets a 3.8-My time scale for the orbital migration of all planets via gas-disk interactions in the solar system, which strongly influenced their final orbital locations (35). Migration of Jupiter and Saturn in turn influenced the overall solar system architecture (36). Additionally, chondrules younger than ~3.8 My after solar system formation, such as those in CB chondrites (37), would have required non-nebular and nonmagnetic formation mechanisms [e.g., planetesimal collisions (38)], rather than nebular shocks (39), X-winds (40), or current sheets (2).

Although the oldest investigated angrites formed in no detectable paleomagnetic field, we have confirmed that Angra dos Reis cooled in a ~17-μT field at ~11 My after solar system formation. This late age [postdating >95% of observed protoplanetary disk lifetimes (14)] suggests that the field source was internally generated, possibly by a core dy-

namo or, conceivably, crustal remanence produced by an earlier dynamo. Therefore, the angrite parent body dynamo did not initiate until sometime between ~4 and ~11 My after solar system formation (Fig. 3). This late timing is consistent with recent planetesimal thermal evolution models invoking shallow magma oceans (41), which predict that planetesimal dynamos would not initiate until the core began to crystallize. It is also consistent with thermal evolution models invoking large-scale magma oceans that considered thermal blanketing of the core by ^{26}Al decay in the mantle (19, 20), which would delay thermal convection dynamos until several My after accretion [which occurred <0.25 My after solar system formation for the angrite parent body (42)] and differentiation, assuming negligible quantities of ^{60}Fe in the core.

We conclude that our paleomagnetic analyses of three volcanic angrites, in combination with previous analyses of Semarkona chondrules, suggest that the early solar system midplane magnetic field at ~2 to 3 au declined from ~5 to 50 μT at ~1 to 3 My after solar system formation to less than 0.6 μT sometime before ~3.8 My after solar system formation, consistent with the rapid dispersal of the solar nebula by this time. Our constraint on the timing of the nebula dispersal is consistent with theoretical predictions and astronomical observations of the lifetimes of extrasolar protoplanetary disks. It sets a deterministic time scale for many aspects of solar system formation and evolution, including the accretion time scale of the Sun, formation mechanisms for young chondrules, and the formation and orbital migration time scales of the planets.

REFERENCES AND NOTES

1. N. J. Turner et al., in *Protostars and Planets VI*, H. Beuther, R. S. Klessen, C. P. Dullemond, T. Henning, Eds. (Univ. of Arizona Press, Tucson, 2014), pp. 411–432.
2. C. P. McNally, A. Hubbard, C.-C. Yang, M.-M. Mac Low, *Astrophys. J.* **791**, 62 (2014).
3. A. Johansen, M.-M. Mac Low, P. Lacerda, M. Bizzarro, *Sci. Adv.* **1**, e1500109 (2015).
4. I. W. Stephens et al., *Nature* **514**, 597–599 (2014).
5. R. R. Fu et al., *Science* **346**, 1089–1092 (2014).
6. J. N. Connelly et al., *Science* **338**, 651–655 (2012).
7. R. Alexander, I. Pascucci, S. Andrews, P. Armitage, L. Cieza, in *Protostars and Planets VI*, H. Beuther, R. S. Klessen, C. P. Dullemond, T. Henning, Eds. (Univ. of Arizona Press, Tucson, 2014), pp. 475–496.
8. T. Takeuchi, P. Artymowicz, *Astrophys. J.* **557**, 990–1006 (2001).
9. J. Kominami, S. Ida, *Icarus* **167**, 231–243 (2004).
10. R. Helled et al., in *Protostars and Planets VI*, H. Beuther, C. P. Dullemond, R. S. Klessen, T. K. Henning, Eds. (Univ. of Arizona Press, Tucson, 2014), pp. 643–666.
11. M. Chaussidon, M.-C. Liu, in *The Early Earth: Accretion and Differentiation*, J. Badro, M. Walter, Eds. (American Geophysical Union, Washington, DC, 2015), pp. 1–26.
12. F. A. Podosek, P. Cassen, *Meteoritics* **29**, 6–25 (1994).
13. C. P. M. Bell, T. Naylor, N. J. Mayne, R. D. Jeffries, S. P. Littlefair, *Mon. Not. R. Astron. Soc.* **434**, 806–831 (2013).
14. E. E. Mamajek, in *Exoplanets and Disks: Their Formation and Diversity*, T. Usuda, M. Ishii, M. Tamura, Eds. (2009), vol. 1158, pp. 3–10.
15. K. Keil, *Chem. Erde Geochem.* **72**, 191–218 (2012).
16. B. P. Weiss, J. Gattacceca, S. Stanley, P. Rochette, U. R. Christensen, *Space Sci. Rev.* **152**, 341–390 (2010).
17. L. T. Elkins-Tanton, B. P. Weiss, M. T. Zuber, *Earth Planet. Sci. Lett.* **305**, 1–10 (2011).
18. B. P. Weiss et al., *Science* **322**, 713–716 (2008).
19. J. H. Roberts, A. S. Rivkin, N. L. Chabot, Thermal challenges for recording an ancient core dynamo on Vesta. *Workshop on Planetesimal Formation and Differentiation* **1768**, abstr. #8033 (2013).
20. M. G. Sterenborg, J. W. Crowley, *Phys. Earth Planet. Inter.* **214**, 53–73 (2013).
21. S. J. McKibbin, T. R. Ireland, Y. Amelin, P. Holden, *Geochim. Cosmochim. Acta* **157**, 13–27 (2015).
22. T. Mikouchi, M. Miyamoto, G. McKay, L. Le, *Meteorit. Planet. Sci.* **36** (suppl.), A134 (2001).
23. P. H. Warren, *Earth Planet. Sci. Lett.* **311**, 93–100 (2011).
24. Y. Amelin, M. Sapah, *Met. Soc. Abs.* **75**, 5199 (2012).
25. A. R. Sarafian et al., Wet angrites? A D/H and Pb-Pb study of silicates and phosphates. *Lunar Planet Sci. Conf. XLVI*, abstr. #1542 (2015).
26. H. Busemann, S. Lorenzetti, O. Eugster, *Geochim. Cosmochim. Acta* **70**, 5403–5425 (2006).
27. Materials and methods are available as supplementary materials.

28. C. Suavet, B. P. Weiss, T. L. Grove, *Geochem. Geophys. Geosyst.* **15**, 2733–2743 (2014).
29. J. Shaw, *Geophys. J. Int.* **39**, 133–141 (1974).
30. L. Tauxe, H. Staudigel, *Geochem. Geophys. Geosyst.* **5**, Q02H06 (2004).
31. One Sahara 99555 subsample was stable to >145 mT. The two thermally demagnetized Sahara 99555 samples exhibited a small amount of additional unblocking (equal to 5 to 10% of NRM) up to ~375° to 425 °C.
32. G. Lesur, M. W. Kunz, S. Fromang, *Astron. Astrophys.* **566**, A56 (2014).
33. X. N. Bai, *Astrophys. J.* **791**, 137 (2014).
34. R. P. Nelson, O. Gressel, O. M. Umurhan, *Mon. Not. R. Astron. Soc.* **435**, 2610–2632 (2013).
35. W. Kley, R. P. Nelson, *Annu. Rev. Astron. Astrophys.* **50**, 211–249 (2012).
36. K. J. Walsh, A. Morbidelli, S. N. Raymond, D. P. O'Brien, A. M. Mandell, *Nature* **475**, 206–209 (2011).
37. E. R. D. Scott, *Annu. Rev. Earth Planet. Sci.* **35**, 577–620 (2007).
38. A. N. Krot, Y. Amelin, P. Cassen, A. Meibom, *Nature* **436**, 989–992 (2005).
39. S. J. Desch, H. C. Connolly Jr., *Meteorit. Planet. Sci.* **37**, 183–207 (2002).
40. F. H. Shu, H. Shang, T. Lee, *Science* **271**, 1545–1552 (1996).
41. W. Neumann, D. Breuer, T. Spohn, *Earth Planet. Sci. Lett.* **395**, 267–280 (2014).
42. M. Schiller, J. N. Connelly, A. C. Glad, T. Mikouchi, M. Bizzarro, *Earth Planet. Sci. Lett.* **420**, 45–54 (2015).

SUPPLEMENTARY MATERIALS

www.sciencemag.org/content/355/6325/623/suppl/DC1
Materials and Methods
Supplementary Text
Figs. S1 to S20
Tables S1 to S5
Data S1 to S3
References (*43–151*)

Editor's Summary

Meteorite magnetism in the early solar system

The young solar system contained a disc of gas and dust within which planet formation occurred. The disc eventually dissipated after the Sun ignited and the planets formed, but exactly when that happened has been difficult to determine. Wang *et al.* measured tiny magnetic fields preserved in angrites, an ancient type of meteorite. They interpret a drop in magnetic field strength about 4 million years after the solar system formed as a sign that the gas had cleared—along with the magnetic field that it carried. The results will enhance our understanding of planet formation, both in our solar system and around other Sun-like stars.

Science, this issue p. 623

Article Tools	Visit the online version of this article to access the personalization and article tools: http://science.sciencemag.org/content/355/6325/623
Permissions	Obtain information about reproducing this article: http://www.sciencemag.org/about/permissions.dtl

Supplementary Materials for

Lifetime of the solar nebula constrained
by meteorite paleomagnetism

Huapei Wang,* Benjamin P. Weiss, Xue-Ning Bai, Brynna G. Downey,
Jun Wang, Jiajun Wang, Clément Suavet, Roger R. Fu, Maria E. Zucolotto

*Corresponding author. Email: huapei@mit.edu

This PDF file includes:

> Materials and Methods
> Supplementary Text
> Figs. S1 to S20
> Tables S1 to S5
> References

Other Supplementary Material for this manuscript includes the following:
(available at www.sciencemag.org/cgi/content/full/355/6325/623/DC1)

> Data S1 to S3 (as zipped files)

A. Materials and Methods

1. Magnetic properties of angrites

A previous petrographic study of Angra dos Reis found that it contains pseudo single domain titanomagnetite (approximate composition magnetite$_{25.6}$-ulvöspinel$_{65.1}$-spinel$_{6.4}$) and iron sulfides (*43*). The thermomagnetic curve of Angra dos Reis has inflections at ~250 ºC, ~350 ºC and ~550 ºC (*18*), indicative of phases with multiple Curie points and/or thermal alteration during the heating process in air. Severe thermochemical alteration is confirmed by the large differences between the heating and cooling curves (*18*).

We conducted thermomagnetic measurements on the volcanic angrites using an Alpha Precision Instruments translation Curie balance at the Rutgers Paleomagnetism Laboratory in a bias field of 0.15 T. Our measurements on D'Orbigny confirm previous observations (*18*) of a dominant Curie temperature near ~575 ºC, indicating near-stoichiometric magnetite. Electron microscopy data confirm the presence of nearly pure magnetite along with a diversity of Ti- and Al-rich spinels (*18*). Our Curie balance measurements also showed that Sahara 99555 contains near-stoichiometric magnetite (Fig. S1). Likewise, titanomagnetite has also been reported in Asuka 881371 (*44*). The thermomagnetic curves of D'Orbigny (*18*) and Sahara 99555 (Fig. S1) exhibit moderate repeatability between the heating and cooling curves, indicating lack of major thermally-induced alteration [compare with the very poor repeatability typically observed for extraterrestrial iron-nickel bearing samples (*45*)].

Previous room temperature hysteresis measurements of D'Orbigny, Asuka 881371 and Angra dos Reis (*18*) found that their ratios of saturation remanence to saturation magnetization (M_r/M_s) and coercivity of remanence to coercivity (B_{cr}/B_c) fall mainly in the pseudo-single domain region (*46, 47*), similar to other angrites (*48*). Angra dos Reis has a coarser ferromagnetic grain size relative compared to D'Orbigny. Our measurements of Sahara 99555 using a Princeton Measurements Corporation Micromag 2900 alternating gradient force magnetometer (AGFM) in the Rutgers Paleomagnetism Laboratory found that it has hysteresis properties nearly identical to those of D'Orbigny (Table S1).

First-order reversal curves (FORC) (*49, 50*) have been widely used to characterize rock magnetic properties of ferromagnetic minerals in rocks and sediments [e.g. ref. (*51, 52*)]. We conducted FORC measurements on the three angrites using the Rutgers AGFM (field increments of 0.6 mT; number of curves 513; measurement time of ~10 hours) and AGFM of the same model at the Massachusetts Institute of Technology (MIT) (field increments of 2.0 mT; number of curves 163; measurement time of ~1.5 hours). We processed the data using the software package FORCinel v. 2.0 (*53*) with a smoothing factor of 6 (for the Rutgers AGFM) and 3 (for the MIT AGFM) (Fig. S2). The FORC diagrams of unheated angrites provide further evidence that their magnetic minerals are in the pseudo-single domain size range. FORC measurements on D'Orbigny and Sahara 99555 on fresh samples and again after heating them to 600 ºC in air observed growth of a modest quantity of middle-coercivity grains due to the heating. By comparison, the FORC diagram of the fresh Angra dos Reis subsample differed greatly from a subsample heated to 700 ºC, indicating severe thermochemical alteration from the heating process. The shorter central ridge of the fresh Angra dos Reis sample relative to the fresh D'Orbigny and Sahara 99555 samples indicates a coarser grain size for Angra dos Reis (Fig. S2).

The observed differences in domain state between the various angrites are in good agreement with the fact that D'Orbigny and Sahara 99555 are volcanic rocks with quenched, glassy textures and Angra dos Reis is a coarser-grained plutonic rock. These data also indicate

1

that D'Orbigny and Sahara 99555 are more suitable for thermal demagnetization and paleointensity experiments than Angra dos Reis due the latter meteorite's susceptibility to thermochemical alteration. Further evidence for this conclusion is provided in Sections A5 and A6.

Overall, we see that angrites are unusually good paleomagnetic field recorders among known basaltic achondrite groups, most of which contain multidomain metal that experiences extreme alteration during heating and can undergo complex recrystallization during primary cooling on the parent body (*16*). Pseudo-single domain materials like the angrites have found to robustly and stably record paleomagnetic fields (*54-56*) and are commonly used for paleomagnetic investigations on Earth and elsewhere in the solar system. Such investigations have demonstrated primary magnetizations in rocks billions of years old using conglomerate (*57, 58*), fold (*59*), baked contact (*60, 61*), and reversal (*62*) tests.

2. Transmission X-ray microscopy of D'Orbigny and Angra dos Reis

To better characterize the sizes of the ferromagnetic grains within D'Orbigny and Angra dos Reis, we conducted synchrotron-based full-field transmission hard X-ray microscopy (TXM) (*63*) using a recently developed transmission hard X-ray microscope at beamline X8C (*63*) at the National Synchrotron Light Source (NSLS), Brookhaven National Laboratory (BNL). This technique has recently been shown to be capable of imaging sub-micrometer-sized magnetite grains within geological samples (*64*). Although TXM is not capable of imaging at the ~nm resolution of transmission electron microscopy (TEM) (*65*), TXM has the major advantage over TEM in that it enables three dimensional volumetric analyses over much larger fields of view (tens of μm). The ability of the TXM to scan a small volume of sample (~10^2-10^3 μm in size) greatly increased the chance of locating and imaging the low abundance of magnetic grains in our meteorites.

We mounted ~millimeter-sized particles from each meteorite on tungsten carbide pins with a tip diameter of ~50 μm using nearly X-ray transparent epoxy. The sample mounts were then placed on a kinematic holder on a stage with translation and rotational motion capability. To target the magnetization-carrying iron minerals, we used an X-ray energy of 7.2 keV, just above the iron absorption K-edge (7.112 keV) (*66*), to allow for maximum X-ray absorption for maximum contrast. We acquired images with a fields-of-view of 20 μm × 20 μm for D'Orbigny and 40 μm × 40 μm for Angra dos Reis. Without binning, the size of each pixel was 10 nm for D'Orbigny and 20 nm for Angra dos Reis. We first scanned the angrite grains using a fast mosaic mode by binning 8×8 pixels (for an effective pixel size of 80 nm for D'Orbigny and 160 nm for Angra dos Reis). Then we switched to a slower but higher resolution mode with 2×2 pixel binning (for an effective pixel size of 20 nm for D'Orbigny and 40 nm Angra dos Reis). We then stitched together mosaic TXM images from these multiple fields-of-view. Although the effective spatial resolution of the TXM used to image nanoparticles in a 20 μm × 20 μm field-of-view is ~50 nm (*63*), the small amount of X-ray absorption from an individual ~100-nm-sized ferromagnetic grain is still too weak to produce enough contrast to provide detectable image (*64*).

For D'Orbigny, we could not detect any ferromagnetic grains within the igneous matrix (Fig. S3A). The absence of observed Fe-rich crystals larger than ~100-200 nm within D'Orbigny suggests that the majority of the magnetization-carrying grains are smaller than this size, consistent with the overall fine pseudo-single domain grain size of this meteorite.

By comparison, we clearly observed ~2-5 μm sized iron-rich grains for Angra dos Reis (Fig. S3B). X-ray absorption near edge structure (XANES) spectroscopy is very sensitive to composition and so can be used to constrain the mineralogy of these grains. For example, magnetite and iron standards (measured by the same TXM in this study) and a replotted iron sulfide standard sample from another instrument (*67*) show distinctive XANES spectral features (Fig. S3C). Based on the overall spectral shape and absorption edge position of each spectrum, which were normalized to similar scales using K-edge absorption differences below and above that of iron (Fig. S3C), we found that the iron-rich mineral grains (marked as #1, #2, #3 and #4 in Fig S3B) within Angra dos Reis are consistent with being (titano)magnetite, in agreement with our expectation from hysteresis and thermomagnetic data. Overall, the TXM-determined magnetite grain sizes are in good agreement with the hysteresis (Table S1) and FORC data (Fig. S2) indicating a pseudo-single domain grain size for both meteorites and a finer grain size for D'Orbigny relative to Angra dos Reis.

3. Demagnetization of natural remanent magnetization (NRM) in D'Orbigny and Sahara 99555

3.1. Samples, magnetometer and analysis software. Our samples of D'Orbigny were from the same deep-interior parent sample studied by Weiss et al. (*18*) (labeled "Fx" where x is the subsample number) (Fig. S4A). Our samples of Sahara 99555 were drawn from a chip containing fusion crust on one side from the American Natural History Museum (sample #5008), with 6 subsamples taken more than 5 mm away from fusion crust (Fig. S4B). All subsamples from a given meteorite in this study are mutually oriented with respect to one another and, for D'Orbigny, with respect to the subsamples in Weiss et al. (*18*). Subsamples subjected to AF were mounted on GE 124 quartz glass 2.5 cm rounds using cyanoacrylate cement, respectively (holder moments including cement $<1 \times 10^{-11}$ Am^2). Sample preparation and storage were conducted in a class ~10,000 magnetically shielded clean laboratory (DC field <150 nT) in the MIT Paleomagnetism Laboratory.

Nearly all moment measurements were acquired with a 2G Enterprises Superconducting Rock Magnetometer (SRM) 755 in the MIT Paleomagnetism Laboratory, situated inside a magnetically shielded room (DC field <150 nT). Each moment measurement consists of 4 repeat measurement taken at 0º, 90º, 180º and 270º rotations of the sample; these four measurements are then corrected for rotation and averaged (*68*). We conducted two experiments to characterize the moment resolution of the MIT SRM. First, we acquired 300 repeat measurements (each consisting of the aforementioned 4 rotations) with no sample in the SRM bore. Of these 300 measurements, 95% had moments of $\leq 0.99 \times 10^{-12}$ Am^2 (Fig. S5A-D). Second, we acquired 300 repeat measurements of D'Orbigny sample F8j after it was AF demagnetized. This distribution had a mean value of 1.7×10^{-9} Am^2 (given by the sample's moment) and a 3 standard deviation (3-σ) variation of 1.9×10^{-12} Am^2 (Fig. S5E-H).

NRM components were identified using principal component analysis (PCA) (*69*) and analyzed using the PaleoMag software package (*70*) and MATLAB.

3.2. Alternating field (AF) demagnetization. We conducted automated AF demagnetization of NRM as well as automated isothermal remanent magnetization (IRM) and anhysteretic remanent magnetization (ARM) and demagnetization [see ref. (*68*)]. For each AF demagnetization step, we acquired at least three moment measurements: we first applied the AF in the *x*, *y* and *z* directions, making a moment measurement after the latter application; we then applied an AF in

the *x* direction, followed by a second moment measurement; and finally applied an AF in the *y* direction, followed by a third moment measurement. We then averaged these three measurements to suppress any gyroremanent magnetization (GRM) following the Dunlop-Zijderveld protocol (*71*). For many AF steps, we repeated the above 3-measurement sequence several times to reduce spurious ARM noise associated with imperfections with the AF waveform. For the angrites, we used AF step increments of 0.5 to 2.0 mT up to a peak AF field of 145 mT. Our typical AF experiment for each subsample required about 10-30 hours and collected ~600-2000 individual magnetic moment measurements. For the plots and analyses, we averaged all the measurements (ranging from 3 to 12 individual measurements) from each AF demagnetization level.

The main source of uncertainty in our measurements of the angrite samples subjected to AF demagnetization is the spurious remanence associated with the imperfect AF waveform mentioned above [see ref. (*72*)]. To demonstrate this, following the 300 measurements of the moment D'Orbigny sample F8j (Fig. S5E-H), we subjected the sample to 300 repeated three-axis AF steps with a peak field of 50 mT, measuring the sample moment after each AF application. The sample moment 3σ variation about the mean value is 1600× larger than the intrinsic SRM sensor resolution and 600× larger than noise associated with measuring a sample of comparable moment magnitude (Fig. S5I-L).

We AF demagnetized 9 new subsamples from D'Orbigny (Table S2) and 11 subsamples from Sahara 99555, focusing in particular on 6 deep (> 3 mm from fusion crust) subsamples (Table S3). The directions of the low-coercivity (LC) components (demagnetized by ~4-10 mT; Fig. 1A, B) in D'Orbigny progressively rotate from west to east during a traverse across a ~2 cm size parent sample (Fig. S6A). Combined with the high ratios of vector change of NRM to IRM acquisition to the same LC AF demagnetization level ($\Delta NRM/IRM_{LC}$) (0.3-1.2) (Tables S2) within this coercivity range, this indicates that the LC components are IRM overprints. Likewise, the LC components in Sahara 99555 (demagnetized by ~6-10 mT; Fig. 1D, E) are unidirectional across the ~1 cm diameter parent sample and present in both fusion-crusted and interior (> 3 mm deep) subsamples (Fig. S6B). Combined with the LC components' high values of $\Delta NRM/IRM_{LC}$ (0.5-0.7) (Table S3), this indicates that they too are IRM overprints. We conclude that the LC components for D'Orbigny and Sahara 99555 are IRM overprints, probably by collectors' magnets [see ref. (*16*)].

The middle-coercivity (MC) components of most subsamples of D'Orbigny (Fig. 1A) and interior (>3 mm from fusion crust) subsamples of Sahara 99555 (Fig. 1D) unblock from the end of the LC component up to ~65 mT (Table S2) and ~50 mT (Table S3), respectively (with one exceptional Sahara 99555 subsample stable to >145 mT). They are approximately unidirectional throughout the parent D'Orbigny sample (Fig. S6C) and throughout the interior portion of Sahara 99555 (Fig. S6D). The MC components gradually decay during AF demagnetization, with the NRM direction slowly becoming increasingly noisier with increasing AF demagnetization level. As a result, our choice of the upper limit of the MC component is somewhat arbitrary, such that some subsamples of each meteorite still show very weak directional stability above the values listed in Tables S2 and S3. Although the NRMs of both samples are essentially demagnetized after removal of the MC component, our paleointensity experiments (Section A4) demonstrate that both meteorites have significant quantities of grains with coercivities >50-70 mT that are not carrying NRM [analogous to previous observations of young mare basalts (*73*)]. As a result, paleointensities for both meteorites in the high-coercivity (HC) range (from ~50-70 mT to 145 mT) are within error of zero (Fig. 1C, F, S7, Tables S2 and S3, and Section A4).

The MC component in D'Orbigny in this study was previously labeled as a "HC" component by Weiss et al. (*18*), who estimated that it was stable up to 150 mT. We have renamed this component here because of our recognition from demagnetization of more D'Orbigny material that some samples are completely demagnetized by only 70 mT (with the others showing only weak directional stability and no intensity decay above this level), such that most grains with coercivities >70 mT are essentially unmagnetized. We now refer to the latter as the HC range.

AF demagnetization in the HC range produces only a bundle of noisy points around the origin without any consistent decay in moment magnitude, likely due to spurious ARM acquisition (*73*) (Fig. 1A, D). PCA of this AF range for D'Orbigny and Sahara 99555 produces scattered best-fit directions (Fig. S6E, F). Total ARM (AF of 145 mT, bias field of 50 µT, an analog for total thermoremanent magnetization (TRM) acquired in a 10-µT field, using a TRM/ARM ratio of 5) given to both D'Orbigny and Sahara 99555 persists during AF demagnetization to >100 mT (Fig. S8A, B), indicating that the ferromagnetic grains within the HC range are capable of acquiring high-stability magnetization. This indicates the absence of a magnetic field on the angrite parent body at ~4 million years (My) after solar system formation. The weak, directionally unstable (Figs. 1A, D) and nonunidirectional (S6E, F) remanence in the HC range is likely a combination of spurious remanence due to imperfections in the AF waveform (*72*) and possibly also spontaneous remanence (*74*).

We end this section by discussing our AF demagnetization analyses of the exterior samples from Sahara 99555. We found that the NRMs of fusion-crusted (~0-1 mm deep) and adjacent samples (~1-3 mm deep) after demagnetization to 10 mT have different intensities and directions compared to subsamples from the interior (>3 mm deep) (Fig. S4B, C). In particular, the magnetization blocked above 10 mT for these samples differs by ~90º from the MC direction identified in deeper samples. This fusion crust baked contact test demonstrates that Sahara 99555 has not been completely remagnetized since landing on Earth and, in particular, that is original ferromagnetic minerals have not been destroyed by terrestrial weathering. This provides powerful evidence that interior samples have the capability to retain pre-terrestrial records of paleomagnetic fields. Furthermore, the lack of a strong MC component in fusion-crusted samples supports the hypothesis that the MC component in interior samples is pre-terrestrial.

3.3. Thermal demagnetization. We conducted combined AF and thermal demagnetization of NRM experiments on two subsamples from each of D'Orbigny and Sahara 99555. We first applied stepwise AF demagnetization at intervals of 0.5 mT up to a maximum field of 10 mT to remove the LC weak IRM overprints. Then we switched to thermal demagnetization at intervals of 25 ºC starting from 100 ºC with soak times of ~30-60 minutes at peak temperature. This thermal demagnetization employed our new controlled atmosphere system (*28*) using an oxygen fugacity (fO$_2$) set to approximately to that of the iron-wüstite (IW) buffer to mitigate thermochemical alteration (see Section A5). This value was identified based on previous studies that found angrites crystallized under approximately IW-1 to IW+1 conditions (*15, 75-77*).

We found that the peak unblocking temperature of the NRM of D'Orbigny is only ~200 ºC. Likewise, most of the NRM of Sahara 99555 demagnetizes by ~200-300 ºC (although there is weak directional stability to 400 ºC). Unlike for AF demagnetization, during which the MC component exhibited a high-coercivity tail such that the NRM for some subsamples exhibited directional stability without intensity decay up to relatively high AF levels (145 mT), thermal demagnetization completely removed the middle-temperature (MT) component by

5

~200-400 ºC, leaving no higher-temperature tail. These NRM unblocking temperatures are well below the ~580 ºC peak Curie temperature of volcanic angrites (Fig. S1) as well as the peak >450 ºC unblocking temperature of total ARM (AF of 145 mT, bias field of 50 µT, an analog for total TRM acquired in a 10-µT field, using a TRM/ARM ratio of 5) (Fig. 2A, B). PCA of the high-temperature (HT) range for D'Orbigny and Sahara 99555 yields scattered best-fit directions (Fig. S6E, F). The resultants of the unit vectors of the HC/HT directions are 2.3 and 2.6 for the eleven D'Orbigny subsamples (nine HC and two HT directions) and five interior Sahara 99555 subsamples (three HC and two HT directions), meaning that we cannot reject the hypothesis that they are drawn from a random distribution at the 95% confidence level as specified by a Watson test (*78*). The slight clustering of the HC and HT directions is due to the fact that AF demagnetization did not entirely remove the partial TRM (pTRM) originated MC components, which persisted slightly into the HC magnetization range. In summary, thermal demagnetization confirms the existence of a significant population of essentially unmagnetized grains with blocking temperatures >~200ºC.

The MT component is therefore a magnetic overprint. Néel theory (*79*) and its extension to pseudo-single domain grains (*80*) indicates that the ~125-225 ºC peak 1-h unblocking temperature of the MT component for D'Orbigny is marginally consistent with origin of the MT component as a VRM acquired on Earth, given the likely <50 ka terrestrial ages of most non-Antarctic meteorites (*81*) (we know of no terrestrial ages measured for D'Orbigny and Sahara 99555). Although the 6-14 µT paleointensities for the MT component as determined by the Shaw and Thellier-Thellier methods (see Section A4) is lower than the present ~30 µT intensity of the equatorial geomagnetic field, D'Orbigny was not in a fixed orientation since landing on Earth, which could explain its low paleointensity. Unfortunately, previous VRM acquisition and VRM decay experiments on D'Orbigny (*18*) and additional experiments on D'Orbigny subsample F8j conducted as part of this study observed non-linear acquisition rates with log(time) and high heterogeneity amongst subsamples. As a result, we cannot quantitatively estimate the Earth field VRM for volcanic angrites with reasonable accuracy

The ~200-400 ºC peak 1-h unblocking temperatures of the MT component for Sahara 99555 may be marginally too high for its MT component to be a terrestrial VRM. Likewise, the starting ~100 ºC unblocking temperatures for the MT component in Sahara 99555 suggest that its MT component is marginally stable against remagnetization in the terrestrial field since the meteorite's arrival on Earth. Additionally, a fusion crust baked contact test supports a pre-terrestrial origin of the MC/MT component for Sahara 99555 (Section A3.2). Instead of VRM, the MC/MT component in Sahara 99555 may be a pTRM overprint from reheating on the angrite parent body following the meteorite's formation. The unblocking relationships discussed above suggest Sahara 99555's MT component would be marginally stable against remagnetization over the last 4.5 Ga in the asteroid belt [assuming a constant blackbody temperature of 150-180 K (*16*)] as well as marginally stable during the meteorite's transfer to Earth [assuming a constant blackbody temperature of 273 K and a transfer time to Earth from the asteroid belt given by Sahara 99555's cosmic ray exposure age of ~7 My (*15*)]. In support of this hypothesis, U-Pb data for phosphate in Sahara 99555 indicate a weak disturbance at ~3.5 ± 1.7 My after crystallization (*82*), suggestive of a modest (< 500 ºC) thermal event at this time. Because this age is within error of the formation age of the oldest known plutonic angrite (NWA 2999/6291, which has a Pb/Pb age of 4560.74 ± 0.42 My ago), the thermal event may have been associated with magmatism associated with the emplacement of plutonic angrites. In further support of this hypothesis, the paleointensities of the MT components in volcanic angrites

as determined by the Shaw and Thellier-Thellier methods range are 7-10 µT (Section A4), within error of that of Angra dos Reis (Section A6). Therefore, although we cannot exclude a terrestrial VRM origin for the MC/MT component in Sahara 99555, we favor its origin as a partial thermal overprint acquired after the onset of the angrite parent body dynamo.

4. Paleointensity data for volcanic angrites
4.1. Overview and methodology. We conducted paleointensity experiments for the HC range in D'Orbigny and Sahara 99555 using the ARM and IRM methods. We also conducted paleointensity experiments on the MT ranges of these meteorites using a pTRM-based Shaw method and the Thellier-Thellier method. Finally, we computed new ARM and IRM paleointensities for Asuka 881371 by reprocessing previous measurements (*18*). We use these data to further constrain the origin of the NRM components and place an upper limit on the field present during primary cooling.

4.2. D'Orbigny and Sahara 99555
4.2.1. ARM and IRM paleointensities. Because our thermal stability tests (Section A5) show that volcanic angrites significantly thermochemically alter at temperatures above ~400 ºC, it is difficult to obtain accurate paleointensity limits on the HC/HT magnetization range using heating methods. Therefore, we employed non-heating methods that compare the NRM intensity to that of laboratory ARM and IRM (Fig. S7).

Our ARM and IRM paleointensity methods are as follows. We begin by using the orthogonal vector endpoint plots of demagnetization of NRM (e.g., Fig. 1A, D) to identify demagnetization directional trends and changes in demagnetization direction. In combination with PCA, these yield the NRM components and their associated AF ranges (see Section A3.2 and Tables S2, S3). We then plot the magnitude of the initial NRM minus the magnitude of remanence removed during each AF demagnetization step (ΔNRM) versus the magnitude of ARM acquisition (bias field of 50 µT) at each AF level (ΔARM) and versus the magnitude of saturation IRM (SIRM) removed by each AF demagnetization step (ΔSIRM). The ARM and IRM paleointensity estimates are given by $P_{ARM} = (\Delta NRM/\Delta ARM) \times (b/f')$ and $P_{IRM} = (\Delta NRM/\Delta IRM) \times a$, for bias field b and empirically determined coefficients f' and a. For a given component, ΔNRM, ΔARM, and ΔIRM are taken over the component's AF range as identified by PCA. Note that we do not identify the ranges for ΔNRM, ΔARM, and ΔIRM using perceived changes in slope in the paleointensity plots; the latter can be somewhat subjective when the trends are curved as they are here for the MC range (likely due to the fact we are using AF demagnetization to isolate what we interpret to be pTRM or VRM, which may not have a single, well-defined coercivity at which they are fully AF demagnetized).

A slight difference in the present approach compared to the multi-vectoral approach described of ref. (*73*) is that we simply plot the changed in magnitude of the NRM rather than vector-subtracted NRM anchored to the beginning point of each magnetization component. This subtle change does not significantly alter paleointensity estimates for robust origin-trending HC components, but will provide more accurate HC paleointensity estimates under the assumption of an underlying origin-trending NRM that is obscured by spurious remanence. Note also that this approach will yield slightly negative paleointensities when the NRM in the HC range grows in magnitude (i.e., due to the acquisition of spurious magnetization from AF demagnetization), although in practice such paleointensities are essentially always within error of zero.

To avoiding exposing all of our valuable subsamples to strong laboratory-applied fields, we did not conduct ARM or IRM acquisition measurements on all subsamples. Instead, we used the average ARM acquisition curves and AF demagnetization of SIRM curves from their sister subsamples from each meteorite (Fig. S9). Our data show that the ARM and SIRM curves for different subsamples are very similar (Fig. S9), indicating that the rock magnetic properties of the meteorites are mostly homogeneous.

As in ref. (73), we report uncertainties on each paleointensity by calculating the 95% confidence interval on the ΔNRM/ΔARM and ΔNRM/ΔSIRM slope using Student's two-tailed t-test. These uncertainties do not take into account the poorly constrained values of f' and a. Previous meteorite paleointensity studies have used the mean values for these coefficients derived from studies of a wide range of lithologies and mineralogies. However, unlike those previous studies, here we have a variety of powerful datasets (TXM images and XANES spectra, FORC diagrams, and studies of terrestrial analog samples from the Galapagos described below) that constrain the grain size and shapes of the ferromagnetic minerals, leading us to use slightly adjusted values of f' and a compared to the mean values reported in ref. (73).

For volcanic angrites, given the estimated magnetite grain size of ~50-200 nm as deduced from rock magnetic experiments and TXM images (Sections A1 and A2), we adopted a conservative nominal $f' = 5$ and minimum value of 3.3 based on a previous quantitative study of ARM properties as a function of magnetite grain size (83) (Fig. S10). To further test the validity of this f' value, we conducted ARM paleointensity experiments on 6 ocean island basaltic lava samples from the Galapagos archipelago with known thermal paleointensity values (~4 μT) and that have similar rock magnetic properties to the volcanic angrites (84). In particular, the Galapagos lava samples have M_r/M_s ratios ranging from 0.12 to 0.29 and f' values ranging from 3.2 to 9.5 (Table S1). In stark contrast with the volcanic angrites, NRM and total ARM (AF of 145 mT, bias field of 50 μT, an analog for TRM acquired in a 10-μT field) persist to >100 mT during AF demagnetization (Fig. S8C), indicating that the ferromagnetic grains within the HC range carry TRM formed during cooling from above the Curie temperature in a paleomagnetic field. This supports our conclusion that an $f' = 5$ is reasonable for estimating HC paleointensities for the volcanic angrites and an $f' = 3.3$ will provide a conservative upper limit on these paleointensities. Furthermore, guided again by ref. (83) and our grain size estimates, we adopted a nominal average IRM paleointensity calibration factor $a = 1000$ and maximum value of $a = 1500$ (Fig. S10B). The nominal f' and a values used here are a factor of 2.5 and 1/3, respectively, of those used by Weiss et al. (18) to calculate paleointensities of the MC component in D'Orbigny (in fact, as shown at the end of Section 4.2.3, our thermal remagnetization experiments show that the values used by Weiss et al. (18) are accurate for the MC range). The new values here should be more accurate for the HC range because of our additional constraints on the grain size and the fact that we are calculating paleointensities over a higher coercivity range (~60-145 mT) relative to the typical range used in ref. (18) (~7-50 mT) [see coercivity-dependence of f' and a in Fig. 3 of ref. (83)].

We calculated paleointensities for the HC range of subsamples from D'Orbigny (~60 to 145 mT) and Sahara 99555 (~50 to 145 mT) (Fig. 1C, F, S7, and S11). Due to spurious ARM noise affecting the NRM demagnetization path and our origin-anchoring vector subtraction method, we expect near-zero (and sometimes negative) paleointensity values if the HC range does not contain a TRM acquired in the presence of a significant paleomagnetic field. We found that typical HC magnetization paleointensities for both D'Orbigny and Sahara 99555 are within ±1.0 μT of zero (Table S2 and S3), indicating no resolvable paleomagnetic field.

Each subsample of a given meteorite yields an upper limit on the paleointensity of the field in which it cooled. However, because these paleointensity limits are largely determined by spurious remanence acquired during the demagnetization process, they are likely extreme upper limits on the true paleofield intensity. In fact, because the magnetization directions inferred from PCA fits to the HC range are highly scattered (Fig. S6E, F), the net moment of the parent meteorite reassembled from such samples would be weaker than the moments of the individual subsamples. By implication, a more stringent lower limit on the true HC paleointensity can be estimated by calculating the vector mean of the paleointensities of the subsamples for each meteorite. Using our nominal calibration coefficients ($f' = 5$ and $a = 1000$), we find that the vector mean ARM and IRM HC paleointensities using nine D'Orbigny subsamples are 0.2 µT and 0.3 µT (Table S2), with a grand ARM and IRM HC paleointensity mean of 0.3 ± 0.1 µT. For three Sahara 99555 subsamples, we also find vector mean ARM and IRM HC paleointensities of 0.2 µT and 0.3 µT (Table S3), respectively, with a grand mean of 0.3 ± 0.1 µT. If we instead consider the $f' = 3.3$ lower bound and the $a = 1500$ upper bound, we obtain upper limits on the ARM and IRM vector paleointensities for both D'Orbigny and Sahara 99555 of 0.3 µT and 0.5 µT.

4.2.2. Shaw paleointensities. Because the MT component mainly unblocks below the ~400-500 ℃ temperature at which thermochemical alteration is limited (see Section A5), its paleointensity is measurable using thermal methods. We obtained pTRM-based Shaw thermal paleointensity estimates (*29*) as part of a broader series of experiments aimed at assessing the thermal alteration of angrites. Specifically, after we AF demagnetized the NRM of fresh samples, we conducted stepwise ARM acquisition in a 50-µT bias field up to a peak AF of 145 mT, followed by AF demagnetization to 145 mT. We then gave the samples a pTRM in a 50-µT field in IW conditions. We then AF demagnetized this pTRM (Fig. 2C, D). We repeated these ARM acquisition, AF demagnetization and pTRM acquisition, and AF demagnetization sequences at progressively higher heating temperatures. The pTRM gained (ΔpTRM) during the pTRM acquisition experiments to 150-300 ℃ can be used to calculate a paleointensity by ΔNRM/ΔpTRM × b for bias field b (Table S4). To avoid the LC weak IRM overprints, we used the ΔNRM and ΔpTRM values of the residual moments of NRM and pTRM after AF demagnetization of 10 mT, respectively. Our pTRM paleointensity method is very similar to the Shaw paleointensity method (*29*), with the only difference that we gave the samples pTRM in stead of total TRM from cooling from the Curie temperature. We obtained a mean MT Shaw paleointensity for the three volcanic angrites of 8.1 ± 1.4 µT from the temperature ranges of 200 ℃, 250 ℃ and 300 ℃ (Table S4). Furthermore, pTRM acquired by cooling from 300 ℃ in a field of 10 µT (Fig. 2C, D, purple lines) showed similar AF stability to that of NRM (Fig. 2C, D, black lines), consistent with the NRM itself being a pTRM acquired during heating to this temperature.

4.2.3. Thellier-Thellier paleointensities. To obtain another paleointensity estimate for the MC component, we also conducted Thellier-Thellier double-heating paleointensity experiments using the IZZI [in-field, zero-field (IZ), zero-field, in-field (ZI)] protocol (*30*) on three D'Orbigny and one Sahara 99555 subsamples (Table S5). Prior to starting the experiments, the sample NRMs were AF demagnetized to 10 mT to remove the LC overprint. Starting from room temperature (referred to as 0 ℃), we used the following temperature steps and field-application protocol: 100℃ (ZI), 125 ℃ (IZ), 150 ℃ (ZI), 175 ℃ (IZ), 200 ℃ (ZI), 225 ℃ (IZ), 250 ℃ (ZI),

275 ºC (IZ) and 300 ºC (ZI). We also incorporated four pTRM checks following the zero-field heating steps (150 ºC back to 100 ºC, 200 ºC back to 150 ºC, 250 ºC back to 200 ºC, 300 ºC back to 250 ºC). We used $fO_2 \sim$ IW-1 for all heating steps and a laboratory field of 10 µT for the in-field heating steps. We depict the results using a standard Arai plot (*85*) showing NRM lost during thermal demagnetization versus pTRM gained in the laboratory field during progressive heating (Fig. S12A, B).

Because Thellier-Thellier experiments can be contaminated by IRM overprints (*86*) like those expected from meteorite collectors' hand magnets, we AF demagnetized the samples to 10 mT to remove the LC IRM overprint prior to beginning the above heating schedule. To accurately compare the subsequently acquired pTRMs to the AF demagnetized NRM, we should in principle AF demagnetize each in-field heating pTRM acquisition step also to 10 mT. However, we deliberately chose not to AF demagnetize the pTRMs to 10 mT after each pTRM acquisition step in order to avoid introducing spurious ARM noise to our already very weakly magnetized sample. To correct for this omission, we made use of our previously measured pTRM AF demagnetization spectra (Fig. 2C, D), which show that the ratio of non-AF demagnetized pTRM to that of pTRM that has been AF demagnetized to 10 mT ($pTRM_{AF10\,mT}$) is ~2 for pTRM acquisition temperatures from 150ºC to 300ºC (Fig. S12C, D). So we used a nominal factor of 2 to calibrate the paleointensities. Hence the calibrated MC paleointensities should be twice of those estimated directly from the NRM-pTRM slope in the Arai plots (Fig. S12A, B).

Arai plots of all four subsamples (Fig. S12) are approximately linear from room temperature to 175-200 ºC. After correcting for the 10 mT AF demagnetization pre-treatment (see previous paragraph), this yields Thellier-Thellier MT paleointensities of 7.0 µT to 13.9 µT (Table S5). Three of the four MT component paleointensities pass several thermochemical alteration quality criteria established for Earth rocks (Table S5). Furthermore, the Thellier-Thellier paleointensities for all four subsamples for the higher temperature range from 175-200 ºC to 250 ºC are essentially within error of zero, consistent with a lack of NRM blocked in this range. However, because the paleointensities above 200 ºC do not pass stringent thermochemical alteration quality criteria for terrestrial rocks, we cannot reliably estimate the HT paleointensities using the Thellier-Thellier method. Note that the evidence for modest alteration indicated by the quality criteria does not contradict our conclusion that the NRM is mostly stable at these temperatures for three reasons. First, the maximum absolute difference produced by the 200 ºC pTRM check from 250 ºC normalized to the pTRM acquired at 200 ºC ranges from -14% to 4%, indicating that the near-complete removal of the stable NRM by this temperature is due thermal demagnetization rather than alteration. Second, thermal demagnetization shows that the NRM is removed at temperatures well below those required to remove ARM (Fig. 2C, D). Finally, our thermal alteration tests show that the samples are still relatively unaltered up to temperatures of 400 ºC (Section A5).

These are good agreements between the Thellier-Thellier paleointensities and Shaw paleointensities for the MT component. On the other hand, the Shaw and Thellier-Thellier MT paleointensities are a factor of ~3 larger than the ARM and IRM MC paleointensities. Because the Shaw and Thellier-Thellier paleointensities should be more accurate than the ARM and IRM paleointensities, this suggests that we should probably use $a = 3000$ and $f' = 1.7$ for the latter rather than our nominal values of $a = 1000$ and $f' = 5$, which were optimized for the >60 mT AT range. This is consistent with the fact that these coefficients have been found to increase by a

factor of 2-3 over the AF range from 20-50 mT and may continue to increase at higher AF levels (*83*).

4.3. Reanalysis of Asuka 881371. Weiss et al. (*18*) conducted AF demagnetization and paleointensity studies of a 66-mg subsample of angrite Asuka 881371 (split 63).   The NRM was unstable during AF demagnetization (Fig. S13A), which suggested that the sample was at most weakly magnetized. By averaging multiple AF steps, Weiss et al. (*18*) found that after removal of an LC overprint blocked up to ~9 mT interpreted to be a VRM from residence on Earth, the NRM vector remained approximately stationary during AF demagnetization in the HC range from ~9 mT up to at least 150 mT. Therefore, an origin-trending characteristic NRM component was not isolated either because (i) this component did not exist (such that the HC range was pinned zero-field remanence) or (ii) because its decay was obscured by the acquisition of spurious remanence from the AF demagnetization process.

A powerful way of assessing the origin of the HC magnetization would be to compare PCA fits for this AF range for multiple mutually oriented subsamples, as we have done here for the other angrites: if these are scattered (clustered), this would indicate that the HC range did not (did) contain a true NRM record of a paleofield. Unfortunately, this test was not possible because Weiss et al. (*18*) were only permitted to analyze a single subsample of this small meteorite.

Weiss et al. (*18*) obtained a paleointensity estimate for the HC range under the assumption of an underlying NRM component using two different approaches. The first [method (i)] used least squares slopes observed in the NRM-ARM and NRM-IRM demagnetization plots (the same method described in Section A4.2, with the important exception that NRM vector subtraction was conducted relative to the AF step at the start of the HC range rather than relative to the origin) and yielded paleointensities ranging from 2.1 ± 0.8 to 2.7 ± 1 µT. Although the 95% confidence intervals on the slope fits exclude zero field values, the NRM vector did not trend toward the origin over the HC range, suggesting that the non-zero slopes reflect spurious remanence acquired during AF demagnetization rather than true decay of the NRM intensity. This is why Weiss et al. (*18*) reported a second paleointensity estimate [method (ii)] using the "residual REM" method (i.e., taking the ratio of the NRM remaining after removal of the LC component to the ARM and IRM after demagnetization to an equivalent AF level), which yielded values of ~2 µT. However, the REM method requires assuming the existence of an underlying NRM component, which is called into question by the unstable NRM (Fig. S13A).

A better approach for computing the paleointensity is one that does not assume an underlying NRM component [unlike method (ii)] while also being less susceptible to the effects of spurious remanence acquisition than is method (i). The paleointensity approach described in Section A4.2, which considers moment magnitude rather than vector subtraction, is just such an approach.   This new analysis yields paleointensities of only -0.3 ± 0.4 µT (ARM) and -0.3 ± 0.3 µT (IRM) from AF levels between 4.2 and 81.4 mT (Fig. S13B, C). This demonstrates that magnetization in the HC range has a paleointensity indistinguishable from zero [ARM and IRM paleointensity mean of -0.3 ± 0.5 µT (error range represents uncertainties of calibration factors *f'* and *a*)].

Taking the grand mean of D'Orbigny, Sahara 99555, and Asuka 881371's ARM and IRM paleointensity upper limits with the nominal calibration coefficients, we obtain an overall upper limit of <0.3 µT on the strength of the paleomagnetic field on the angrite parent body about 4 My after solar system formation.

5. Thermal stability tests on D'Orbigny and Sahara 99555

To characterize the thermochemical alteration stability of angrites, we conducted several rock magnetic measurements after laboratory heating under various conditions. Starting with fresh samples, we measured stepwise IRM acquisition curves up to 1 T, stepwise AF demagnetized the applied IRMs, gave the samples additional 1 T IRMs, and then heated the samples to a particular temperature in zero field. The goal of the latter measurements was to determine when alteration might set in during thermal demagnetization of NRM. We then stepwise AF-demagnetized the thermally demagnetized IRM and again measured the stepwise IRM acquisition curves up to 1 T. The goal of the latter measurements was to assess the maximum possible stability expected for IRM and, by implication, NRM. This sequence of measurements was then repeated for increasingly higher heating temperatures. We conducted this entire sequence of measurements at temperatures up to 600 ºC for two fresh D'Orbigny subsamples heated in $fO_2 \sim$ IW and ~IW-1 conditions (Fig S13A-D).

The maximum temperature for which D'Orbigny's mass-normalized IRM for heated samples differs by less than a factor of 2 from that of unheated samples is 400 ºC and 500 ºC for IW and IW-1 conditions, respectively (Fig. S14A, C), indicating that the meteorite is relatively thermochemically stable below these temperatures under these fO_2 conditions. Furthermore, AF demagnetization of thermally-demagnetized IRM data (Fig. S14B, D) shows that that IRM is mostly not removed until after heating to 500 ºC. These observations are important because they allow us to use the lack of any stable magnetization remaining after thermal demagnetization of the NRM to ~200 ºC (Fig. 1B) as evidence for near-zero field conditions during primary cooling of the meteorite. We also conducted similar experiments on a fresh subsample of Sahara 99555 using $fO_2 \sim$ IW, which showed almost the same results. Note that the reason the meteorites experienced alteration above 400 ºC may be explained by the fact that the oxygen fugacities of volcanic angrites are thought to have changed by up to 2 log units over the course of their crystallization (*76*), a scenario that is not perfectly reproduced by our choice of a fixed fO_2 buffer in each experiment.

We also conducted ARM thermal stability tests (*87*) for both D'Orbigny and Sahara 99555. After we AF demagnetized the NRM of fresh samples (Fig. 2C and D), we conducted stepwise ARM acquisition in a 50-μT bias field up to a peak AF of 145 mT. We then gave the samples each a pTRM to a given temperature in a 50-μT field in IW conditions. We then AF demagnetized this pTRM to 145 mT, applied the same ARM and AF demagnetized this ARM to 145 mT. We repeated these pTRM acquisition, AF demagnetization, ARM acquisition and AF demagnetization sequences at progressively higher heating temperatures (Fig. S15). The results show that the NRMs carried by D'Orbigny and Sahara are consistent with being pTRMs acquired in a ~20-μT field from cooling from 150 ºC, a ~10-μT field from cooling from 200 ºC or a ~5-μT field from cooling from 300 ºC (Fig. 2C, D and Table S4). With the ARM tests showing that the two meteorites are still mostly thermochemically stable at 300 ºC (but significantly alter above ~400 ºC), we conclude that the MC components of D'Orbigny and Sahara 99555 cannot be total TRMs cooling from the magnetite Curie temperature (580 ºC) in the presence of more than a few μT of paleomagnetic field on the angrite parent body. Instead, the close approximation of their NRM by pTRMs at ~150-300 ºC supports an origin as a pTRM or VRM overprint.

In conclusion, the thermal stability tests of D'Orbigny and Sahara 99555 showed that they are mostly thermochemically stable up to ~400 ºC under the controlled oxygen fugacity conditions of our NRM thermal demagnetization experiments. Thus, the rapid decrease of NRM

with increasing heating temperature below 200 ºC (Figs. 1B, E and 2A, B) is not due to thermochemical alteration, but due to unblocking of the MT components, which are most likely overprints.

6. Paleomagnetism of Angra dos Reis

Weiss et al. (*18*) concluded that the younger plutonic angrite Angra dos Reis records a ~17 µT paleomagnetic field on the angrite parent body. Previous AF demagnetization showed that the NRM carried by Angra dos Reis persisted to above 290 mT (replotted in Fig. S16A, B) and has similar AF stability as ARM (Fig. S8D), which suggested that the NRM is a total TRM produced during cooling from the titanomagnetite Curie temperature (~400-500 ºC) (*88*). To further test this conclusion, we present here a new analysis of the fusion crust test, new thermal demagnetization analyses, and refinement of the paleointensity analyses using TXM data. We thermally demagnetized 2 new subsamples of Angra dos Reis (Fig. S16C, D) drawn from the same American Museum of Natural History parent sample (#4790) studied by Weiss et al. (*18*) (labeled "AMC*x*", where *x* is the subsample number). We also conducted rock magnetic studies on other chips from the same parent sample.

6.1. Fusion crust baked contact test on Angra dos Reis. A pre-terrestrial origin for Angra dos Reis' NRM is strongly supported by the fusion crust baked contact test of Weiss et al. (*18*). The latter showed that the NRM of Angra dos Reis of fusion crusted samples and interior samples are almost antipodal, indicating that the interior NRM was acquired before atmospheric entry (*18*). We further explore the fusion crust test of Weiss et al. (*18*) by demonstrating that there is a baked zone that contains both a preterrestrial NRM component and a component from atmospheric passage. Although Weiss et al. (*18*) found that such components are not readily revealed by AF demagnetization (likely because they have overlapping coercivity spectra), we show here that the NRM directions and intensities of these samples are consistent with what is expected for a baked zone. In particular, we found that samples taken from within 1-2 mm depth of the fusion crust have a similar direction and intensity (Fig. S17). Starting from ~5 mm away from the fusion crust, the NRM reaches a different constant direction and intensity characteristic of deeper interior samples and that is nearly antipodal to that of the exterior (Fig. S17). The zone between these two regions (i.e., 2-4 mm from the fusion crust) has an NRM with direction and intensity in agreement with the vector sum of the fusion crust and interior NRMs (which predicts a much weaker moment given the antipodal orientation of the interior and exterior directions) (Fig. S17). This fusion crust test provides strong evidence in support of the hypothesis that the NRM of the interior of Angra dos Reis is a TRM record of a planetesimal dynamo field on the angrite parent body.

6.2. Thermal demagnetization of Angra dos Reis. Prior to thermal demagnetization of NRM, we conducted IRM thermochemical stability tests and IRM thermal demagnetization experiments following the methods described above for D'Orbigny and Sahara 99555. Our IRM thermal stability experiments showed that Angra dos Reis is thermochemically stable at ~100 ºC (Fig. S14E, G). However, at ~200 ºC, it starts to experience thermochemical alteration as indicated by a factor-of-2 increase in the IRM acquisition curve. Its AF demagnetization of heated IRM curves decreased to almost zero at 400 ºC (Fig. S14F, H), indicating that the meteorite lost almost all of its IRM by this temperature due to severe thermochemical alteration along with thermal unblocking. This alteration may be occurring due to the presence of troilite,

which has been observed to be problematic during thermal demagnetization of mare basalts (*89*). The thermal unblocking may be a reflection of the presence of titanomagnetite, which typically has a lower Curie temperature (~400-500 ºC) than stoichiometric magnetite (580 ºC).

Because the above experiments indicate that Angra dos Reis is thermochemically stable to ~200 ºC, we conducted thermal demagnetization of NRM of two deep interior subsamples. Since previous AF demagnetization of NRM of Angra dos Reis has shown that it has not been contaminated by IRM overprints (*18*), we did not pre-treat the samples with AF demagnetization. These thermal demagnetization experiments were conducted under two different oxygen fugacity conditions: $fO_2 \sim$ IW for subsample AMC15b1 and $fO_2 \sim$ IW-1 for subsample AMC11. The trend of the NRM during thermal demagnetization (Fig. S16C, D) is similar to that during AF demagnetization (Fig. S16A, B). The remaining NRM is almost unchanged up to ~175-200 ºC but then decreases to the origin at ~325-350 ºC. As was observed for thermal demagnetization of IRM, this decrease in magnetization is likely due to thermochemical alteration along with thermal unblocking. Crucially, NRM thermally demagnetizes under IW-1 conditions at the same rate as ARM (a total TRM proxy) (Fig. S18), consistent with the NRM of Angra dos Reis being a total TRM. The relatively high temperature (>200 ºC) stability of the NRM indicates it is not likely dominated by terrestrial VRM, a conclusion strongly supported by previous VRM acquisition experiments (*18*) [note that this meteorite fell on Earth in only A.D. 1869 (*90*)]. Overall, the demagnetization characteristics of the NRM of Angra dos Reis indicate it has an origin as total TRM acquired on the angrite parent body ~11 My after solar system formation.

6.3. Paleointensity for Angra dos Reis. The above results indicate that Angra dos Reis contains a total TRM formed on its parent body. Unfortunately, thermochemical alteration during heating prevents the use of the Thellier-Thellier heating method to obtain an accurate paleointensity estimate. Instead, we compute ARM paleointensities following the techniques described in Section A4 and using the data of Weiss et al. (*18*).

Given its estimated magnetite grain size of ~2-5 μm as deduced from rock magnetic experiments and TXM images (Sections A1 and A2), we conclude that the nominal average $f' = 2$ and $a = 3000$ values previously used by Weiss et al. (*18*) are well justified (Fig. S10). Given that f' and a have been observed to vary by ranging from -33% to +100% and -50% to +50% of these nominal values, respectively, for the grain sizes in Angra dos Reis (*83*), we estimate a similar error for the ARM paleointensity. We conclude that the paleointensity for Angra dos Reis is 17 ± 8.5 μT.

7. Magnetic anisotropy of angrites
High anisotropy of remanence can render paleointensity estimates inaccurate (*91*). To assess this possibility for angrites, we measured the anisotropy of ARM for D'Orbigny, Sahara 99555 and Angra dos Reis. We imparted ARMs using a 260 mT AF along the three orthogonal directions on D'Orbigny subsamples F7g (50-μT bias field) and F8g (50-μT bias field), Sahara 99555 subsamples 3b (50-μT bias field) and 6d (50-μT bias field) and Angra dos Reis subsamples M1b (100-μT bias field) and M9 (600-μT bias field). We used the measured moments to calculate the magnitude of the maximum (τ_1), intermediate (τ_2), and minimum (τ_3) axes of anisotropy ellipsoid (*92*). Our results show that the angrites are only very weakly anisotropic, with anisotropy degrees ($P = \tau_1/\tau_3$) only up to ~1.3. We find that the shape factor [$T = (2 \times \ln \tau_2 - \ln \tau_1 - \ln \tau_3)/(\ln \tau_1 - \ln \tau_3)$] varies from -1 to 1 (Fig. S19). Because P is the maximum factor by which paleointensities need

to be anisotropy-corrected and is close to 1 for angrites, we chose not to anisotropy-correct the paleointensities in this study.

B. Supplementary Text

1. Constraints on the dispersal of the solar nebula

We have shown that the magnetic field in the angrite parent body region as recorded by the three volcanic angrites was $<\sim 0.6$ μT at ~ 3.8 My after solar system formation at three separate azimuthally-distributed locations along its elliptical orbit in the midplane at ~ 2-3 au from the Sun. An important question is whether the solar nebula field was still present elsewhere in the nebula other than the angrite parent body region. Below, we discuss this possibility and conclude that it is very unlikely. Then we show that the lack of a global field suggests that the nebular gas itself had likely dissipated by this time.

1.1. Meteoritic constraints on the lifetime of the solar nebula. Before continuing, we review the very few existing meteoritic constraints on the lifetime of the solar nebula. First, as stated in the main text, measurements of chondrules from the LL ordinary chondrite Semarkona indicate that a solar nebula magnetic field of intensity 5-50 μT existed in the terrestrial-planet region sometime between $\sim 2 \pm 1$ My after solar system formation (*5*). Second, the elemental compositions (e.g., Si/Mg and Fe/Mg) of chondrules differ from those of the matrices in CR chondrites even though the bulk composition of CR chondrites is solar. This indicates that both chondrules and matrix formed out of a single reservoir of solar composition, which may imply the existence of nebular gas at the time of their formation (*93*). If so, this would indicate that the nebular gas persisted until at least the formation of CR chondrules, currently estimated to be $\sim 3.6 \pm 1$ My after solar system formation from Pb/Pb and Al/Mg chronometry (*94, 95*). Collectively, these data indicate a minimum duration of between $\sim 2 \pm 1$ My after solar system formation for the nebular field and a minimum duration of 3.6 ± 1 My after CAI formation for the nebular gas.

There have been a few previous meteorite studies that have made differing proposals about when the nebula subsequently dissipated. First, a minimum mass solar nebula implies an initial midplane gas density for our solar system of at least 10^{-7} kg m^{-3} at 2 au (*96*). Compositional sorting of accretional layers in the Isheyevo meteorite has been invoked as evidence that nebular gas densities had declined in the asteroid belt to 10^{-8} to 10^{-9} kg m^{-3} by ~ 5 My after solar system formation (*97*). This result is surprising given the low likelihood of Isheyevo happening to accrete during the very short ($\sim 10^{5}$ yr) phase expected for the dispersal of the solar nebula (see Section B.1.2). On the other hand, the constraint from Isheyevo is indirect in that is based on a chondrule production model involving collisions of planetesimals that is not currently well-constrained [i.e., ref. (*98*)]. Furthermore, because no absolute U/Pb ages for Isheyevo's constituents have been published, the timing of this constraint is somewhat uncertain.

Second it has been argued that, unlike older chondrules, CB chondrules formed as a result of an impact on a planetesimal due to CB chondrites' lack of fine-grained matrix, relict grains in chondrules, and fine-grained matrix-like chondrule rims (*38*). The high impact velocities associated with this model may require an impactor with a highly eccentric orbit, which may imply that nebular gas had been depleted by the time of CB chondrule formation. Given the Pb/Pb ages of CB chondrules, this would suggest that the nebula had dissipated by 4.8 ± 0.3 after CAI formation (*99*).

Third, the absence of stable magnetization with unblocking temperatures above 250 ºC in the Kaba CV chondrite indicates that the field during magnetite formation was less than ~ 0.3-3 μT (*100*), with the uncertainty in this upper limit due to the uncertain efficiency of CRM

to TRM (thought to typically range from 0.1-1) (*101*).   Although there are no absolute radiometric age constraints on magnetite formation in Kaba, I/Xe and Mn-Cr data suggest that magnetite formation occurred at ~4-6 My after CAI formation (*100*).

1.2. Implications for the intensity of the global nebular field. We consider it unlikely that the three volcanic angrite samples formed at localized nonmagnetic regions embedded in a globally magnetized nebula. This is because protoplanetary disks are expected to be very weakly ionized, with magnetic Reynolds numbers $Re_M = c_s h \eta$ in the angrite parent body region (i.e., inner disk) on the order of 1 or less (*102-105*), where η, c_s and $h = c_s/\Omega$ are resistivity, sound speed and disk scale height, respectively and Ω is the orbital frequency. With the magnetorotational instability (MRI) suppressed (*106, 107*), magnetic structures on scales of h or less tend to dissipate within an orbital timescale (Ω^{-1}), while large-scale fields tend to diffuse towards a smooth distribution (*108*).

To quantify this process, we consider an extreme situation with the most inhomogeneous expected magnetic field distribution in which the disk ionization is so unrealistically high that the disk is fully MRI turbulent. We take the vertically stratified local shearing-box simulations of Bai and Stone (*109*), and compute the cumulative probability distribution function (CPDF) of magnetic field strength $P(<B)$, which is the probability of being located in a region with field strength smaller than B. These simulations assume that the disk is threaded by a weak net vertical magnetic field characterized by β_0, the ratio of midplane gas pressure to the pressure of the mean vertical field. We also performed an MRI simulation with zero net vertical field, B_z. In computing the CPDFs, data are taken from within $\pm h$ of the simulation box, spanning over more than 150 orbital periods at the saturated state of the MRI turbulence, and field strength is normalized to the root mean square field strength B_{rms}. The CPDF from these simulations are shown in Fig. S20. We see that (i) the probability decreases very rapidly towards $B<B_{rms}$, and (ii) the presence of net vertical flux makes the field distribution more homogeneous. We note that cooling of the volcanic angrites from their Curie temperature to final temperature (over which time the nebular field can be recorded) is of the order a few tens of hours or ~10^{-3} Ω^{-1} in the angrite parent body region. Because this is much less than the coherence time of the MRI (~ Ω^{-1}), our measured CPDF from individual snapshots can be considered as the CPDF experienced by the angrites. The fact that all three independent angrite samples have <0.6 µT paleointensities places a strong constraint on the strength of B_{rms}. Conservatively using the zero-net-flux case, we see that the probability that the B_{rms} is 10 times stronger than our 0.6 µT upper limit is only ~$0.027^3 = 2.0 \times 10^{-5}$.

The above shearing box simulations assumed a disk that does not contain gaps locally depleted in gas. However, global magnetohydrodynamic simulations (*110, 111*) of disks with gaps generated by gravitational torques from embedded planets have found that magnetic fields are efficiently advected into the gap region with the gas flow. Other global simulations (*112*) have also shown that magnetic fields are not excluded from gaps generated in the outer disk located just outside the dead zone (~10-50 au). This qualitatively indicates that the magnetic field intensity distribution expected in a nebula with planet-induced gaps should not differ much from that predicted above. Therefore, our <0.6 µT field constraint for the volcanic angrites still likely implies that the nebular field was globally <0.6 µT by 3.8 My after solar system formation.

1.3. Implications for accretion rates and the lifetime of the solar nebula. We now argue that the lack of a substantial magnetic field recorded by the volcanic angrites likely implies that the

nebular gas itself had essentially dissipated by the time of their formation. Our observation is based on the expectation that magnetic fields play a dominant role in disk angular momentum transport (*1*), which governs global disk evolution. The transport process proceeds either radially via the MRI (*113*) or large-scale laminar field (*33, 114*), or vertically via magnetized disk winds (*115, 116*). In all cases, the magnetically-driven accretion rate is proportional to the square of the field strength (*102, 117*), which implies that our upper limit on the field intensity has constrains the nebular accretion rate driven by magnetic fields.

However, before we discuss these implications in detail, we first discuss the possibility that purely hydrodynamic mechanisms can drive viscous accretion via the generation of turbulence [see ref. (*1*) for a brief overview]. Candidate mechanisms include the vertical shear instability (VSI, also known as the Goldreich-Schubert-Fricke instability) (*34, 118, 119*), the convective overstability (*120, 121*), and the zombie vortex instability [ZVI, (*122, 123*)]. The strength of the turbulence as measured by the Shakura-Sunyaev parameter, α (*124*), needs to exceed $\sim 10^{-3}$ or perhaps even 10^{-2} to achieve an accretion rate of 10^{-8} $M_\odot$ yr^{-1} in standard nebular models [e.g., (*125*)]. While the VSI can drive turbulence with $\alpha \sim 10^{-3}$, the onset of the VSI in the solar nebula requires the disk cooling time to be much shorter than the orbital time. However, for standard dust opacities, it has been shown that the VSI may only operate at intermediate radii between ~ 5-50 au (*126*). Furthermore, with substantial reduction of dust opacities due to planet formation, the VSI is likely suppressed over the entire disk (*126*). Turbulence from the convective overstability can also achieve $\alpha \sim 10^{-3}$ (*127*). However, the overstability is driven by an outward radial entropy gradient, which is not present in standard nebular models at least in the disk midplane region, thus undermining its importance in the solar nebula. Finally, the ZVI requires the gas to behave as nearly adiabatic. It is unclear whether the inner regions of the solar nebula satisfy this requirement. In addition, the level of turbulence resulting from the ZVI is likely weak, of the order $\alpha \sim 10^{-4}$ even in the optimistic scenario of constant vertical gravity (*128*). In summary, based on our current understanding, pure hydrodynamic processes are unlikely to play a dominant role in driving disk accretion and evolution, although more work is needed to fully assess each of the scenarios.

Depending on whether magnetically-driven angular momentum transport was radial or vertical, a field strength in the active regions of the disk of ~ 3 or 30 µT, respectively, at ~ 2-3 au, is consistent with accretion rates of 10^{-8} $M_\odot$ yr^{-1} (*5*), which is typical for rates inferred from nearby pre-main-sequence stars analogous to the proto-Sun (*129*). However, our field constraint likely applies to the midplane of the disk where the field may differ from that of the active surface layer. When the Hall effect is important, recent local numerical simulations have shown that the horizontal component of magnetic field near the disk midplane can be amplified or reduced depending on whether the net vertical nebular field is aligned or anti-aligned with the disk rotation axis (*33, 114, 130*). For a given accretion rate, the field strength would be in the previously estimated 3-30 µT range in the former case and a factor of ~ 2 smaller (setting the horizontal field to be zero) in the latter case. Therefore, we conclude that ~ 2-30 µT is the most conservative estimate of the range of field strength to account for a 10^{-8} $M_\odot$ yr^{-1} accretion rate. This is a factor of ~ 4-50 above our upper limit of ~ 0.6 µT, which instead yields an upper limit on the magnetically driven accretion rate of just 10^{-10} to 10^{-9} $M_\odot$ yr^{-1}. Such accretion rates are below that observed for nearly all transitional disks and indicate that the nebula had essentially completed dissipated at this time (*131*). These results do not support an earlier suggestion that a transition disk phase existed 1 My later in the solar system (*97*).

Observational surveys of pre-main-sequence stars show that dispersal of disks, as

18

indicated from the absence of infrared excess (from warm dust in disks), is accompanied by a substantial reduction of disk accretion rate (*132, 133*). In fact, a wide variety of observational tracers of disks very strongly correlate with one another, including hot (several thousand K) H_2 gas in the inner disk corona (*134*), and cold dust from millimeter observations [e.g., ref. (*135*)], suggesting that disk dispersal occurs nearly simultaneously across the entire disk (*7*). Additionally, relatively few (~10%) objects show evidence of partial disk clearing (*135-137*), and there is a dearth of objects with spectral properties intermediate between full disks and no disks (*138, 139*). These observations imply that disk dispersal is expected to be rapid, on the order of ~10^5 yr.

Such a fast disk dispersal rate is consistent with theoretical expectations. The mechanism of disk dispersal is thought to be a combination of angular momentum transport (accretion) and mass loss via photoevaporation and magnetized disk wind. The disk mass loss rate largely depends on the X-ray and ultraviolet luminosity from the protostar and typically reaches ~10^{-9}-10^{-8} $M_\odot$ yr^{-1} (*140-142*). Calculations show that once the stellar mass accretion rate falls below this mass loss rate, disk dispersal proceeds very rapidly (over ~10^5 yr) as the inner disk becomes starved of material (*7, 142, 143*).

Therefore, even if the solar nebula were still present at 3.8 My after solar system formation and undergoing stellar accretion at the upper limiting rate of 10^{-10} to 10^{-9} $M_\odot$ yr^{-1} permitted by our paleointensity data, the substantially reduced accretion rate would imply that it was in the final stages of rapid dispersal and would dissipate entirely within ~10^5 yr.
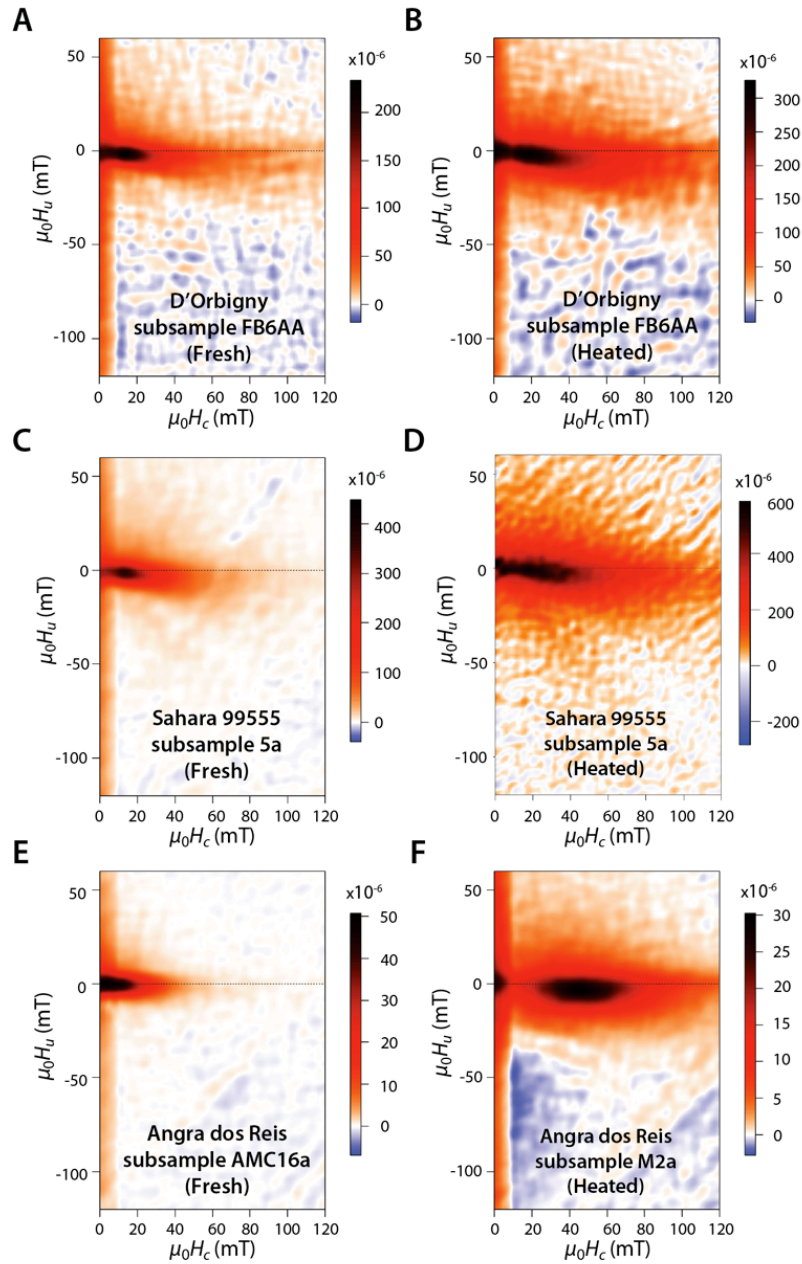
**Supplementary Figures**

Fig. S1
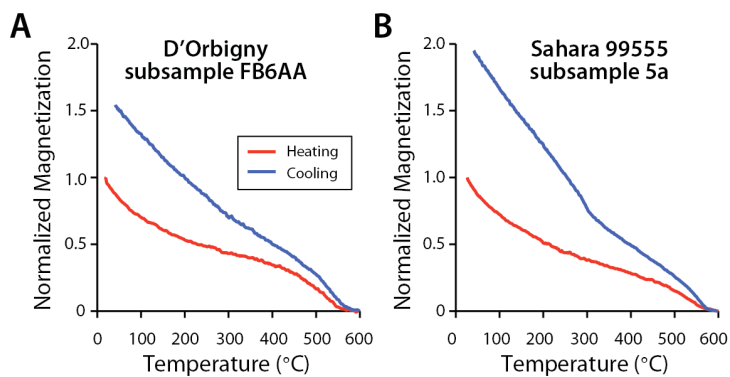
Thermomagnetic curves of angrites. Shown is the induced magnetization (normalized to the magnetization at the start of the experiment) during heating (red) and cooling (blue) in a bias field of 0.15 T in air as measured by a translation Curie balance. **(A)** D'Orbigny subsample FB6AA (18 mg). **(B)** Sahara 99555 subsample 5a (25 mg).

Fig. S2

FORC diagrams for angrites. Shown is $\mu_0 H_u$ (which quantifies the local interaction field) on the ordinate versus $\mu_0 H_c$ (coercivity) on the abscissa. The color bar shows the probability density of hysterons belonging to a given $\mu_0 H_u$ and $\mu_0 H_c$ [see refs. (*49, 50*)]. **(A)** Fresh D'Orbigny subsample FB6AA (18 mg); measured at Rutgers **(B)** D'Orbigny subsample FB6AA heated to 600 °C in air; measured at Rutgers. **(C)** Fresh Sahara 99555 subsample 5a (25 mg); measured at Rutgers. **(D)** Sahara 99555 subsample 5a heated in air; measured at MIT **(E)** Fresh Angra dos Reis subsample AMC16a (18 mg); measured at Rutgers **(F)** Angra dos Reis subsample M2a (4 mg) heated in argon to 700 °C by Weiss et al. (*18*); measured at Rutgers.

Fig. S3
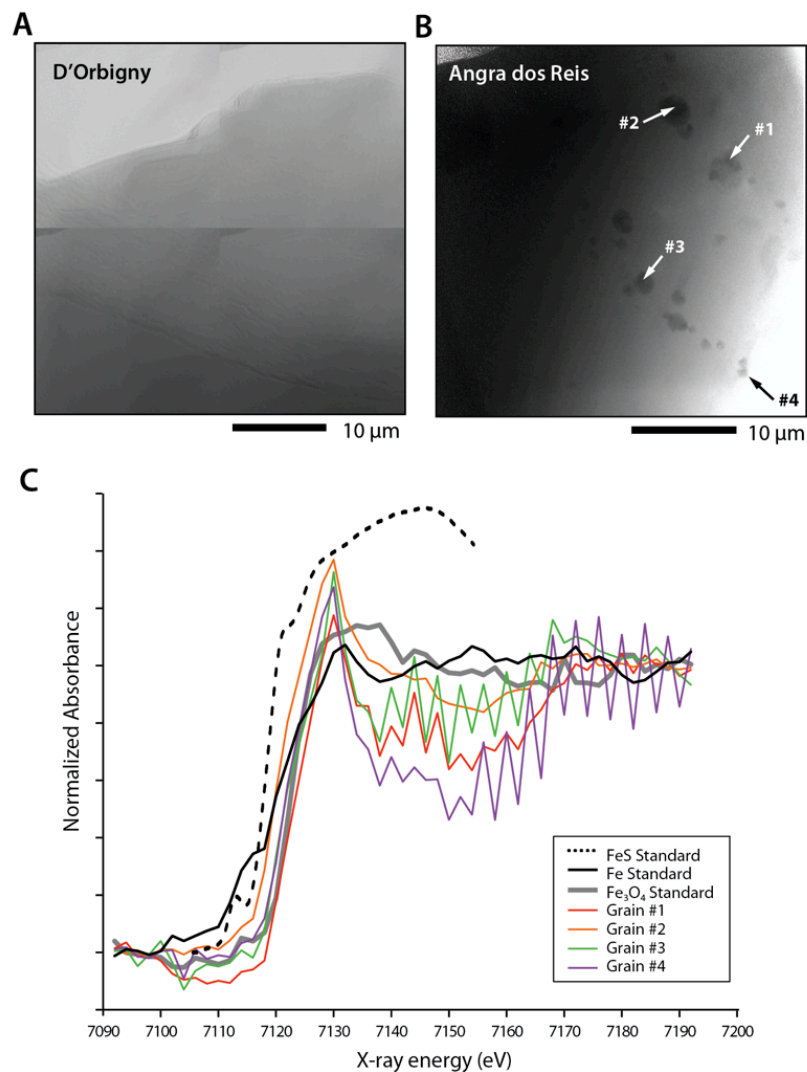
TXM results of angrites. **(A)** Mosaic TXM image of an area of D'Orbigny stitched together from four 20 μm × 20 μm images (2×2 pixel binning). **(B)** TXM image of an area of Angra dos Reis with 40 μm × 40 μm field of view (2×2 pixel binning). **(C)** Normalized XANES of the iron mineral grains within Angra dos Reis and standard samples.

Fig. S4
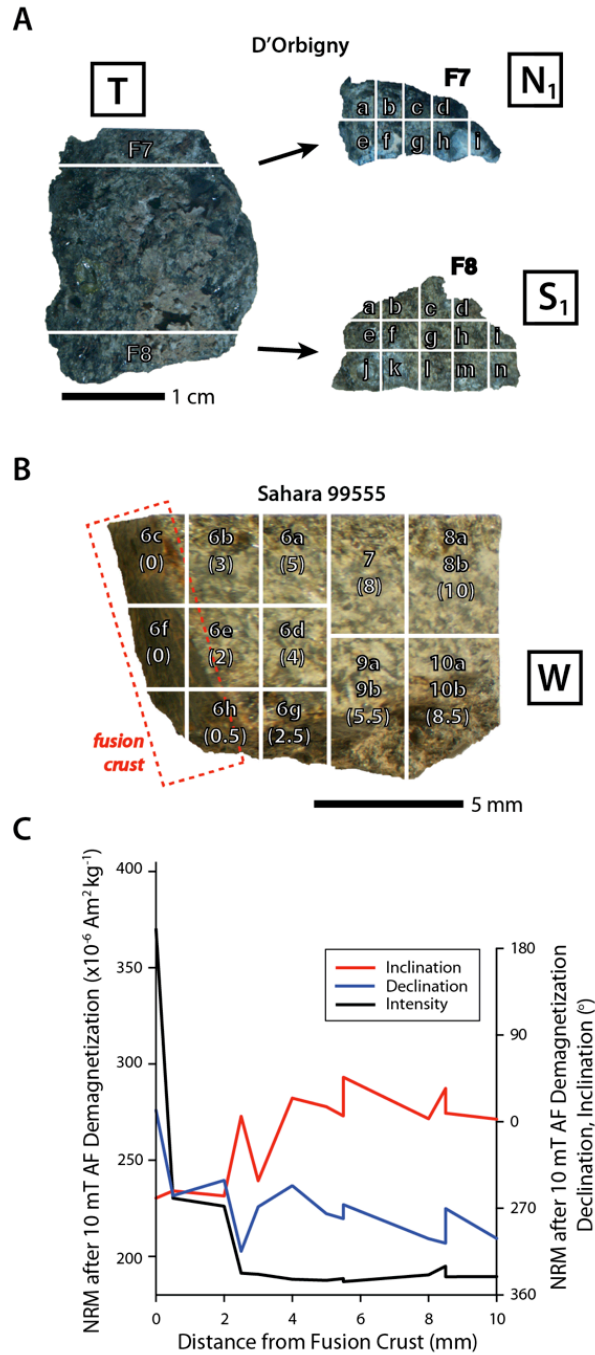
**Cutting diagram of D'Orbigny and Sahara 99555.** **(A)** Parent mass of D'Orbigny used for this paleomagnetic study. White lines are actual cutting lines, which divide the main mass into subsamples F7 and F8. Subsamples F7 and F8 were further cut into smaller subsamples labeled F7a to F7i and F8a to F8n, respectively. Boxes at right represent orientation cubes, which indicate the subsample orientations with respect to the parent meteorite (T = Top = inclination 0º; N = North = declination 90º; S = South = declination 270º; W = West = declination 360º). **(B)** Main mass of Sahara 99555 used for this paleomagnetic study. Shown are the fusion-crusted exterior (<1 mm depth, red dashed box), baked zone (~1-3 mm depth inward) and unbaked

23

interior (>3 mm depth inward). White lines denote sawcut planes, which divide the main mass into several subsamples. Parenthesized numbers under subsample names show the subsample distances from fusion crust in mm. All labeled subsamples except for 6c were measured and plotted in (C). **(C)** Mass-normalized NRM (AF demagnetized to 10 mT) intensity, inclination and declination of subsamples plotted against distance from fusion crust.

Fig. S5
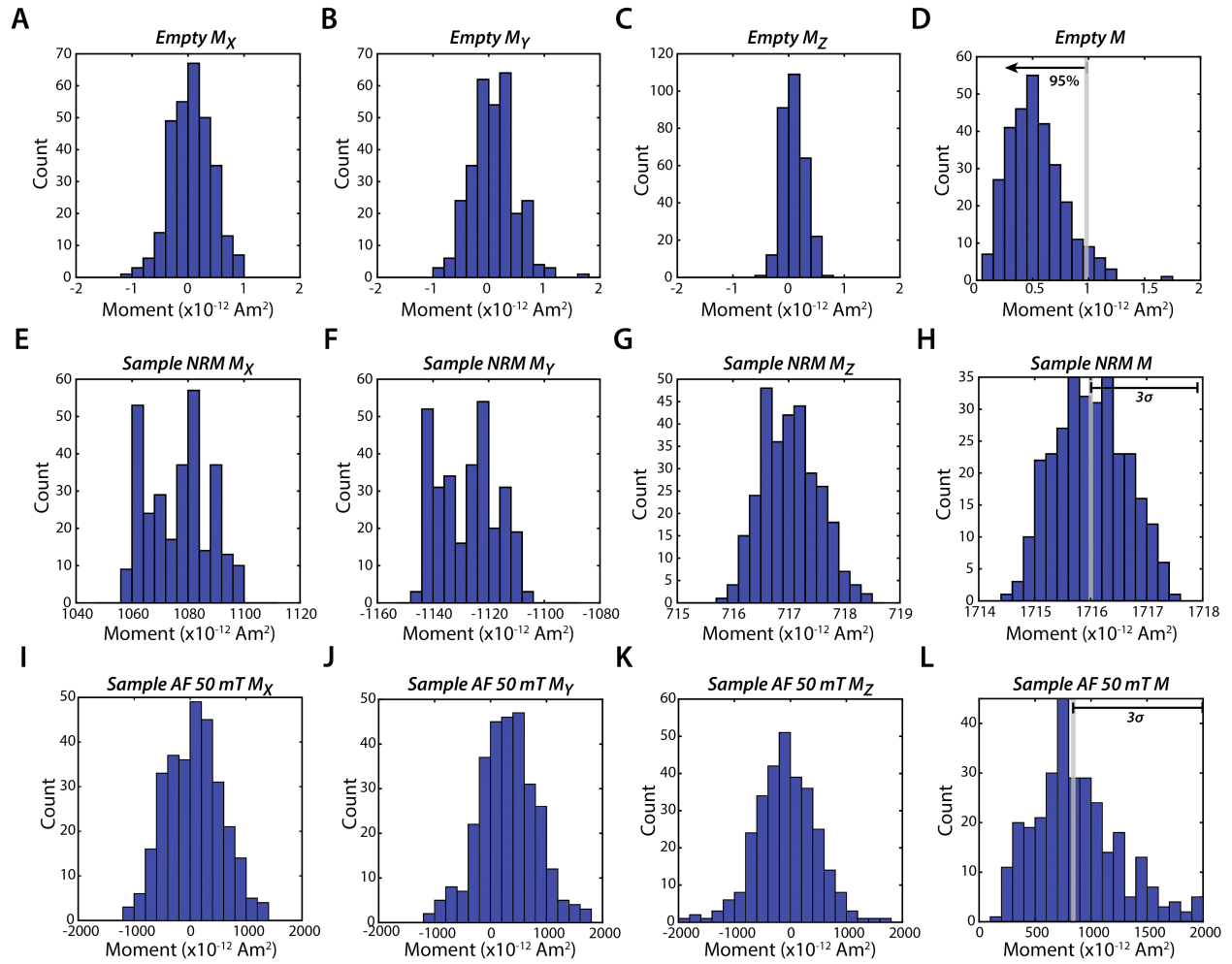
Measurements of moment magnetometry noise and spurious remanence from AF demagnetization. Shown in each panel is the distribution of 300 measurements made with the MIT SRM in the MIT Paleomagnetism Laboratory. The first, second, and third columns show the distributions of the components of the moment measured by *X*, *Y*, and *Z* axes of the SRM, M_X, M_Y, and M_Z, respectively. The fourth column shows the distributions of total moment $M = \sqrt{M_X^2 + M_Y^2 + M_Z^2}$. **(A-D)** Measurements with nothing inside the measurement bore, showing noise contribution only from SRM. **(E-H)** Measurements with DORBF8j in measurement bore after sample had been fully AF demagnetized, showing how noise scales to a sample with moment of 1.7×10^{-9} Am^2. **(I-L)** Measurements with of DORBF8j after repeat three-axis AF applications to a peak field of 50 mT. Vertical grey line in (D) denotes moment value exceeding 95% of measured values. Vertical grey lines in (H, L) denote mean value, and horizontal lines at top right denote 3 standard deviations (3σ) around this mean. This demonstrates that moment variations from spurious remanence acquired during the demagnetization process is 1600× larger than the intrinsic SRM sensor noise and 600× larger than noise associated with measuring a sample with moment of 1.7×10^{-9} Am^2.

Fig. S6
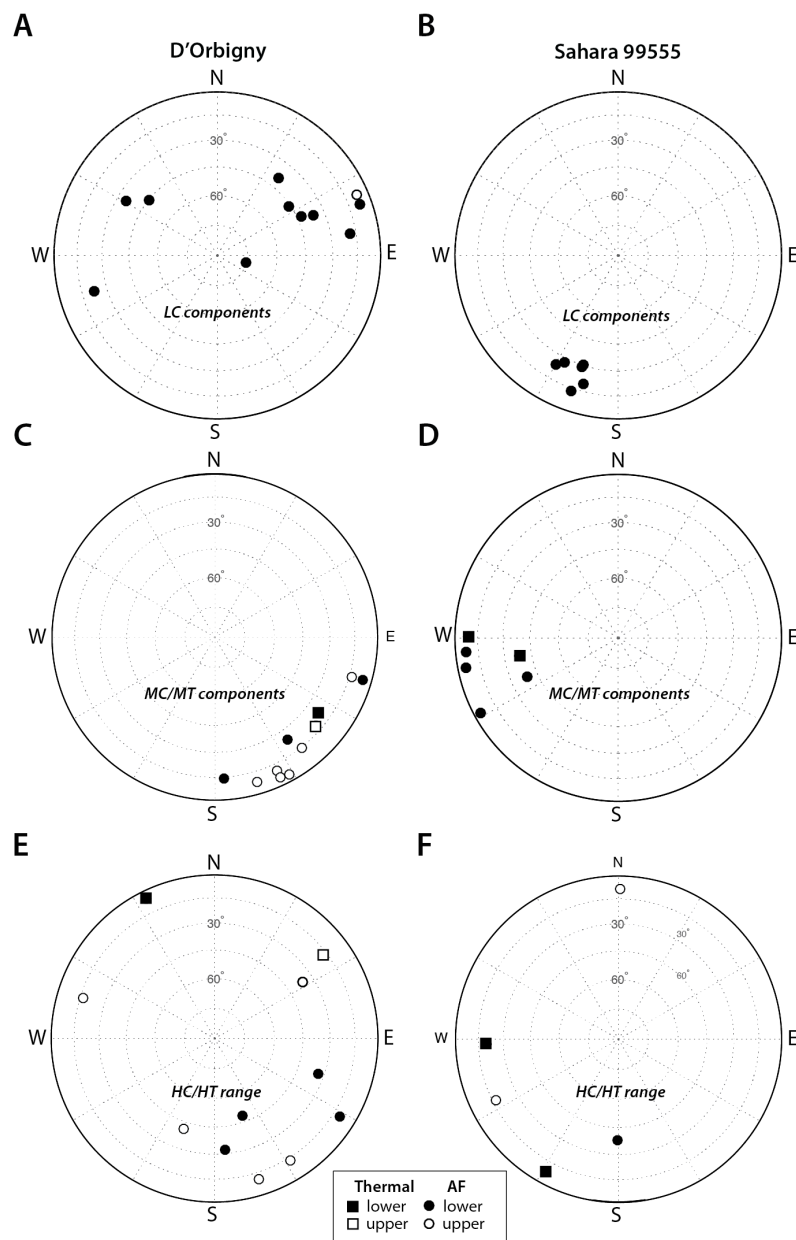
Directions of NRM components in volcanic angrites. **(A, C and E)** Equal area projection showing directions of LC, MC/MT and HC/HT components in mutually oriented D'Orbigny subsamples. **(B, D and F)** Equal area projection showing directions of LC, MC/HT and HC/HT components in mutually oriented interior (>3 mm from fusion crust) Sahara 99555 subsamples. Circles and squares represent PCA directions calculated from AF demagnetization steps and thermal demagnetization steps, respectively. Filled (open) symbols indicate downward (upward) directions.

26

Fig. S7

A — D'Orbigny subsample F7a

B — D'Orbigny subsample F7e

C — D'Orbigny subsample F7g

D — D'Orbigny subsample F7i

E — D'Orbigny subsample F8g

F — Sahara 99555 subsample 10b

**G** — Sahara 99555 subsample 10a
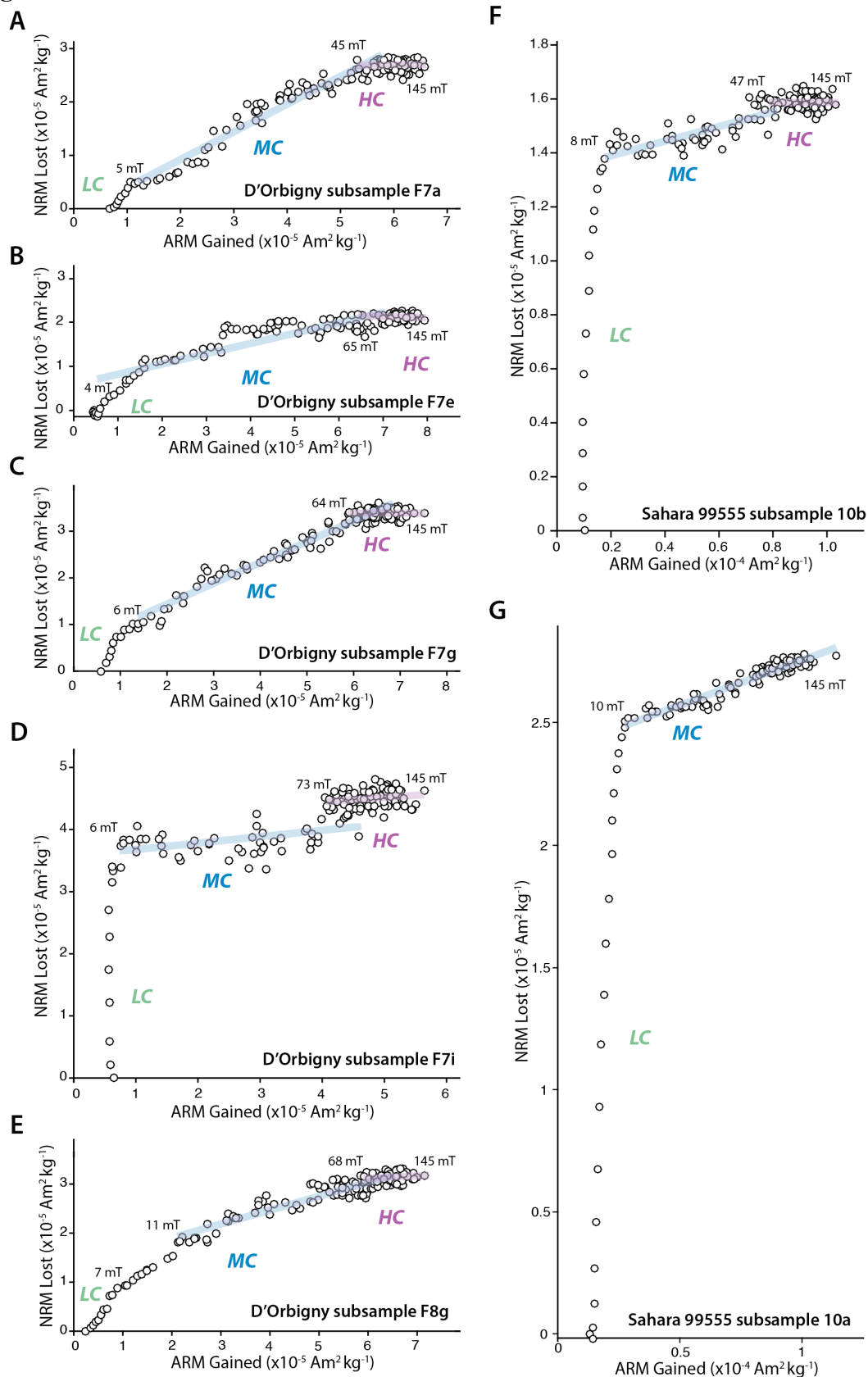
More examples of ARM paleointensity data for D'Orbigny and Sahara 99555. ARM paleointensities estimated from NRM lost during AF demagnetization versus ARM acquired. **(A)** D'Orbigny subsample F7a. HC paleointensity = 0.1 ± 0.7 µT. **(B)** D'Orbigny subsample F7e. HC paleointensity = -0.3 ± 0.7 µT. **(C)** D'Orbigny subsample F7g. HC paleointensity = 0.0 ± 0.7 µT. **(D)** D'Orbigny subsample F7i. HC paleointensity = 0.7 ± 0.8 µT. **(E)** D'Orbigny subsample F8g. HC paleointensity = 0.5 ± 0.8 µT. **(F)** Sahara 99555 interior subsample 10b. HC paleointensity = 0.1 ± 1.1 µT. **(G)** Sahara 99555 interior subsample 10a. HC paleointensity = 3.7 ± 0.2 µT. The ARMs were imparted in a bias field of 50 µT. Blue and purple lines denote MC and HC demagnetization ranges.

Fig. S8
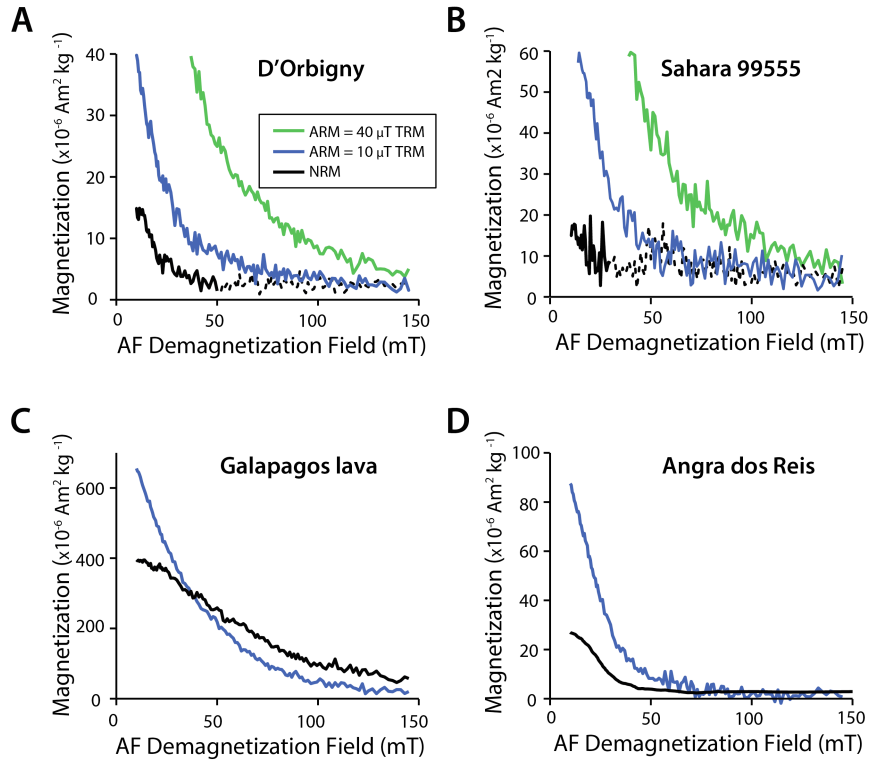
AF demagnetization spectra of NRM and ARM. **(A)** NRM for D'Orbigny subsample F8j (black line) and total ARMs (blue line: AF of 260 mT, bias field of 50 µT, which is equivalent to a total TRM acquired in a 10-µT field, using a TRM/ARM ratio of 5; green line: AF of 145 mT, bias field of 200 µT, which is equivalent to a total TRM acquired in a 40-µT field using a TRM/ARM ratio of 5) for the same subsample. **(B)** NRM for Sahara 99555 subsample 6g (black line) and total ARMs (blue line: AF of 145 mT, bias field of 50 µT, which is equivalent to a total TRM acquired in a 10-µT field using a TRM/ARM ratio of 5; green line: AF of 145 mT, bias field of 200 µT, which is equivalent to a total TRM acquired in a 40-µT field using a TRM/ARM ratio of 5) for the same subsample. **(C)** NRM for Galapagos lava specimen GA84.6p (black line) and total ARM (AF of 145 mT, bias field of 50 µT, which is equivalent to a total TRM acquired in a 10-µT field using a TRM/ARM ratio of 5) for the same specimen (blue line). **(D)** NRM for Angra dos Reis subsample AMC16 (76 mg, black line) and total ARM (peak AF of 260 mT, bias field of 50 µT, which is equivalent to a total TRM acquired in a 25-µT field using a TRM/ARM ratio of 2) for a chip (AMC16a, 17 mg) from subsample AMC16 (blue line). Data for (A) and (B) can be found in Database S3.

Fig. S9
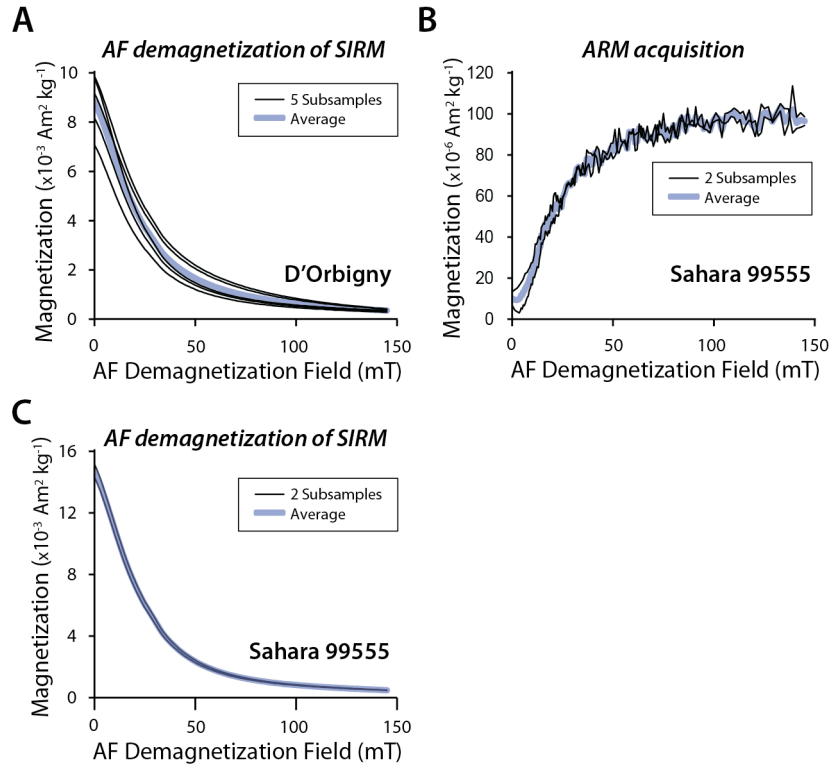
Averaged SIRM AF demagnetization and ARM acquisition. (A) AF demagnetization of SIRM for D'Orbigny subsamples F7a, F7e, F7i, F8i and F8n (thin black lines). Thick blue line is the average of these five subsamples. **(B)** ARM acquisition curves in a bias field of 50 µT for Sahara 99555 interior subsamples 7 and 10a (thin black lines). Thick blue line is the average of these two subsamples. **(C)** AF demagnetization of SIRM for Sahara 99555 interior subsamples 7 and 10a (thin black lines). Thick blue line is the average of these two subsamples.

Fig. S10
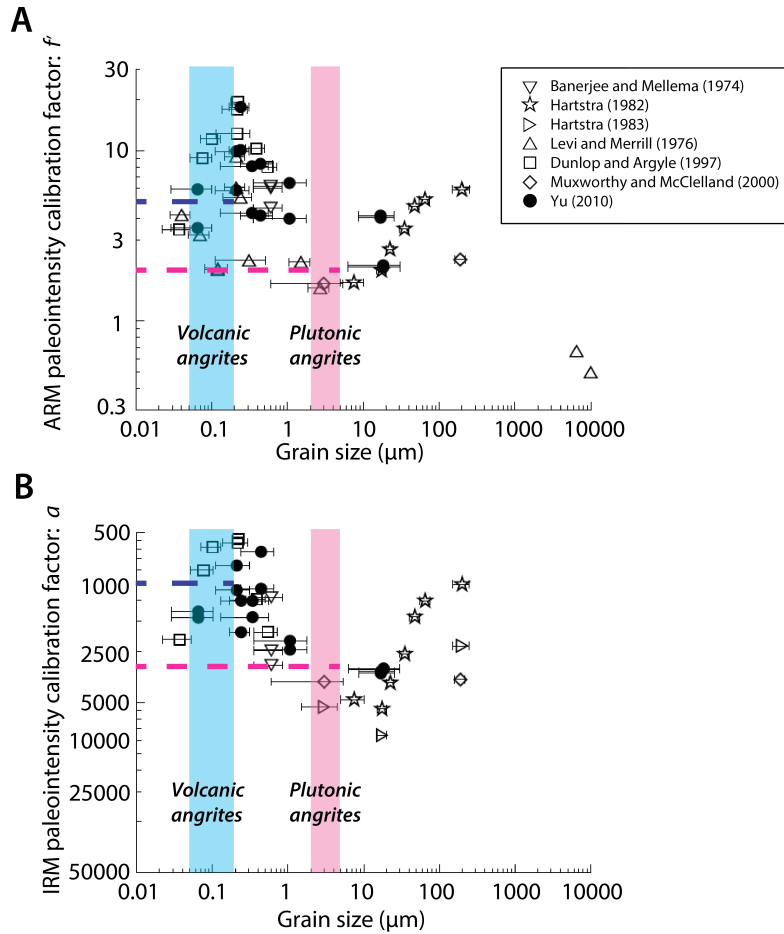
ARM and IRM paleointensity calibration factors. **(A)** ARM calibration factor *f'* versus magnetite grain size. **(B)** IRM calibration factor *a* versus magnetite grain size. Plots are modified from ref. (*83*). Blue and pink shading show estimated grain size ranges for the volcanic angrites and the plutonic angrite Angra dos Reis, respectively. Blue and pink dashed lines show corresponding inferred calibration factors. Data sources: Banerjee and Mellema (1974) [ref. (*144*)], Hartstra (1982) [ref. (*145*)], Hartstra (1983) [ref. (*146*)], Levi and Merrill (1976) [ref. (*147*)], Dunlop and Argyle (1997) [ref. (*148*)], Muxworthy and McClelland (2000) [ref. (*149*)] and Yu (2010) [ref. (*83*)].
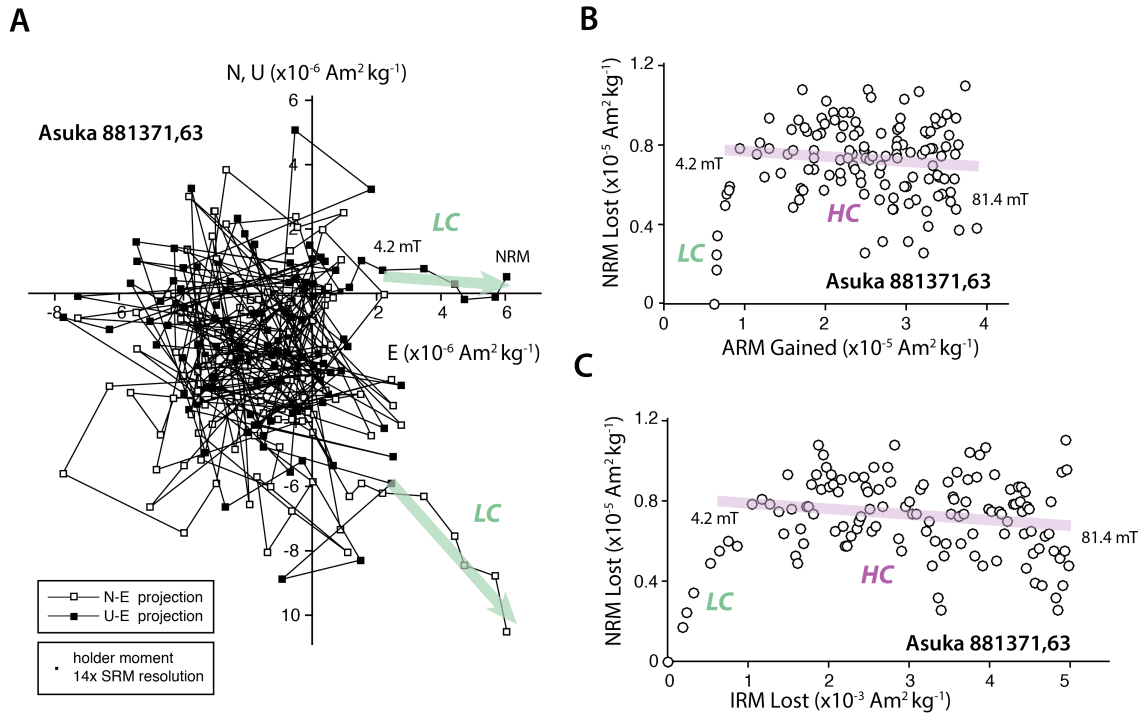
Fig. S11
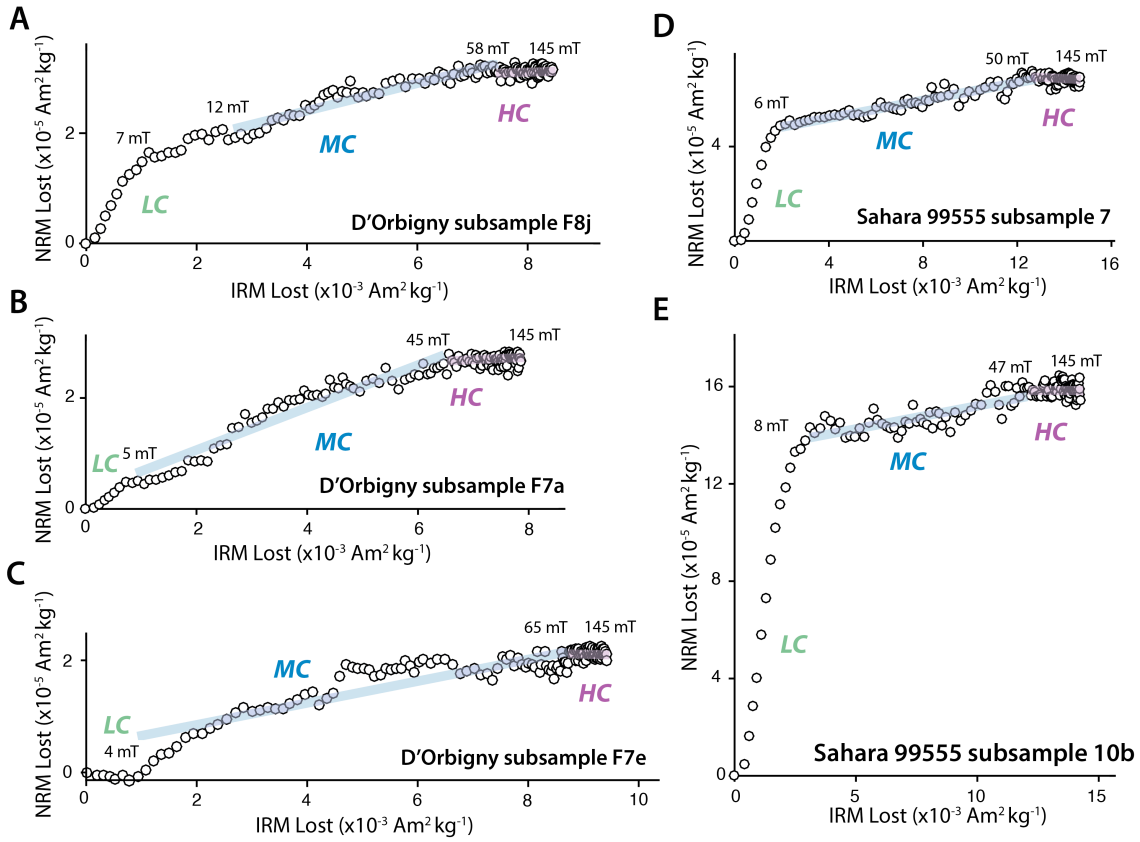
Examples of IRM paleointensity data for D'Orbigny and Sahara 99555. IRM paleointensities estimated from NRM lost during AF demagnetization versus SIRM lost during AF demagnetization. **(A)** D'Orbigny subsample F8j. HC paleointensity = 0.4 ± 0.6 µT. **(B)** D'Orbigny subsample F7a. HC paleointensity = 0.4 ± 0.6 µT. **(C)** D'Orbigny subsample F7e. HC paleointensity = -0.2 ± 1.0 µT. **(D)** Sahara 99555 interior subsample 7. HC paleointensity = -0.4 ± 0.7 µT. **(E)** Sahara 99555 interior subsample 10b. HC paleointensity = 0.1 ± 1.0 µT. Blue and purple lines denote MC and HC magnetization ranges.

Fig. S12
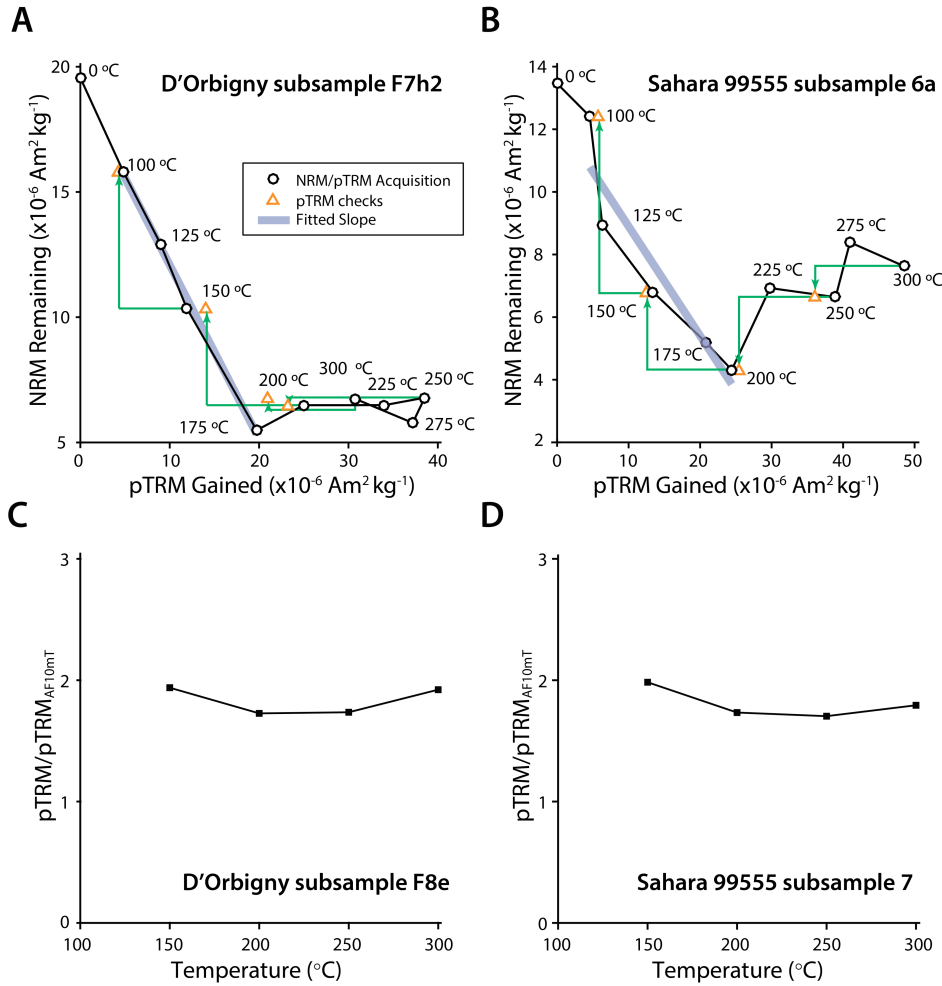
Thellier-Thellier paleointensity Arai diagrams for D'Orbigny and Sahara 99555. Arai diagrams showing NRM lost versus pTRM gained (black circles) including pTRM checks (orange triangles). **(A)** D'Orbigny subsample F7h2 (113 mg). The non-AF-corrected paleointensity is 6.9 µT over the temperature range of 100-175 °C. **(B)** Sahara 99555 subsample 6a (199 mg). The non-AF-corrected paleointensity is 3.5 µT over the temperature range of 100-200 °C. Thick blue lines are the least-squares fits over the temperature ranges. Green lines show the pTRM back-check temperatures. Numbers on the Arai diagrams indicate temperature steps in °C. **(C and D)** The ratio of pTRM to pTRM that has been AF demagnetized to 10 mT ($pTRM_{AF10mT}$) plotted versus the pTRM imparting temperature for D'Orbigny subsample F8e and Sahara 99555 subsample 7, respectively.

Fig. S13

Reanalysis of paleomagnetic data for Asuka 881371. (A) Two-dimensional projection of the endpoints of the NRM vector during progressive AF demagnetization for Asuka 881371 subsample 63. Open (closed) symbols represent projections on the up-east (U-E) and north-east (N-E) planes. Small square in bottom legend denotes the moment per unit mass of sample (for 66 mg sample) of the sample holder (i.e., GE 124 quartz glass sample mounts and quartz glass sample handling rod), which is ~14 times of the intrinsic resolution of the MIT SRM (Section A3.1 and Fig. S5). **(B)** ARM paleointensities for the HC range (4.2-81.4 mT) estimated from NRM lost during AF demagnetization as a function of ARM acquired (bias field of 50 µT). HC paleointensity = -0.3 ± 0.4 µT. **(C)** IRM paleointensities for the HC range (4.2-81.4 mT) estimated from NRM lost during AF demagnetization as a function of SIRM lost by AF demagnetization. HC paleointensity = -0.3 ± 0.3 µT. Green arrows denote LC magnetization ranges. Purple lines denote HC magnetization ranges. Using moment measurements from Weiss et al. (*18*).

IRM acquisition curves

**AF demagnetization of
thermally demagnetized SIRM**
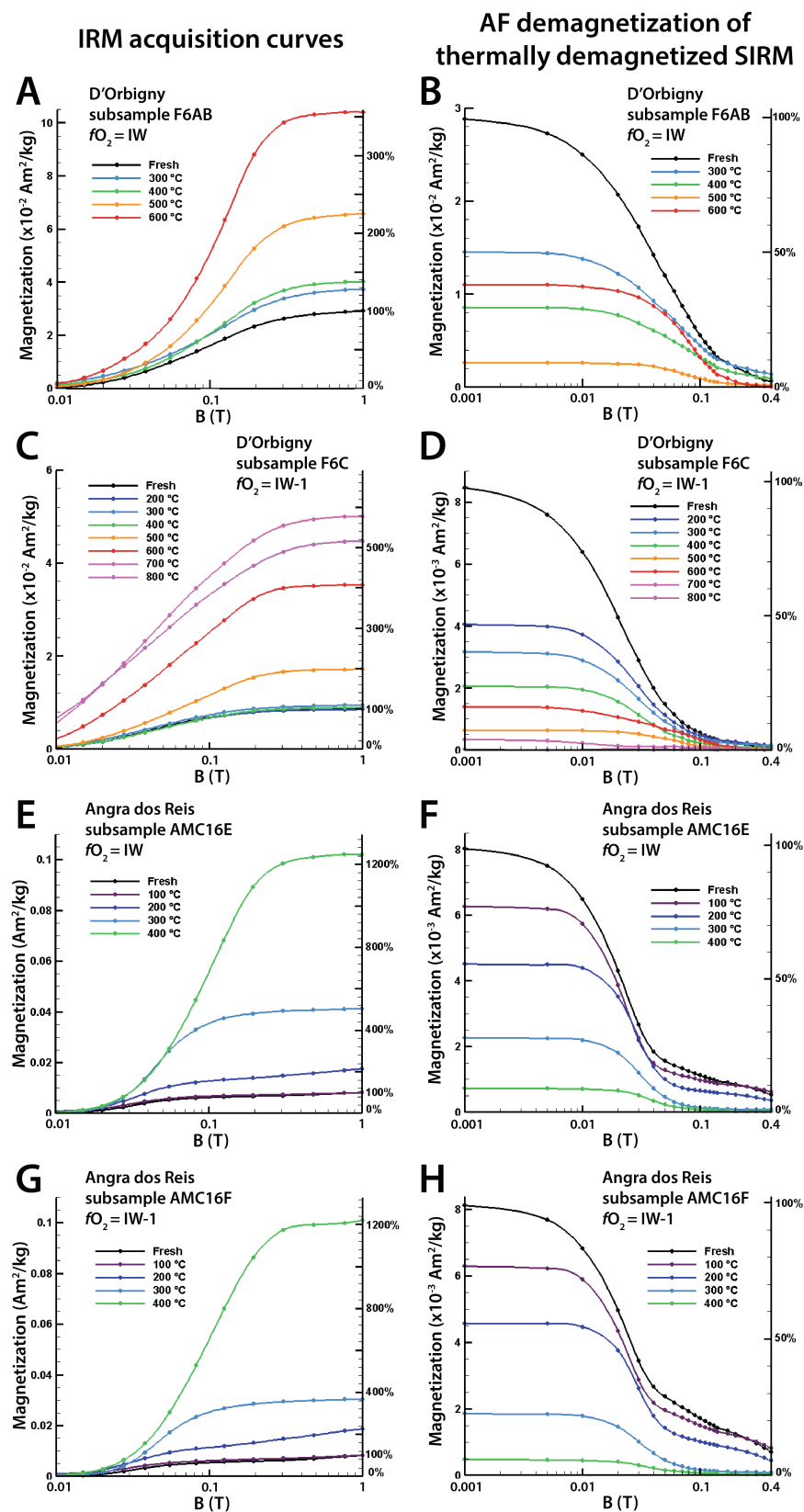
IRM acquisition curves and AF demagnetization of thermally demagnetized IRM. Starting with unheated samples, stepwise IRM acquisition was conducted up to 1 T followed by stepwise AF demagnetization. Then, the samples were given a 1 T IRM, heated in zero field under IW or IW-1 conditions, and then stepwise AF-demagnetized. We then stepwise AF-demagnetized this thermally demagnetized IRM and again measured the stepwise IRM acquisition curves up to 1 T. This sequence of measurements was then repeated for increasingly higher heating temperatures. **(A, B)** D'Orbigny subsample F6AB (4.8 mg) in IW conditions. **(C, D)** D'Orbigny subsample F6C (14.0 mg) in IW-1 conditions. **(E, F)** Angra dos Reis subsample AMC16E (8.6 mg) in IW conditions. **(G, H)** Angra dos Reis subsample AMC16F (13.9 mg) in IW-1 conditions.

Fig. S15
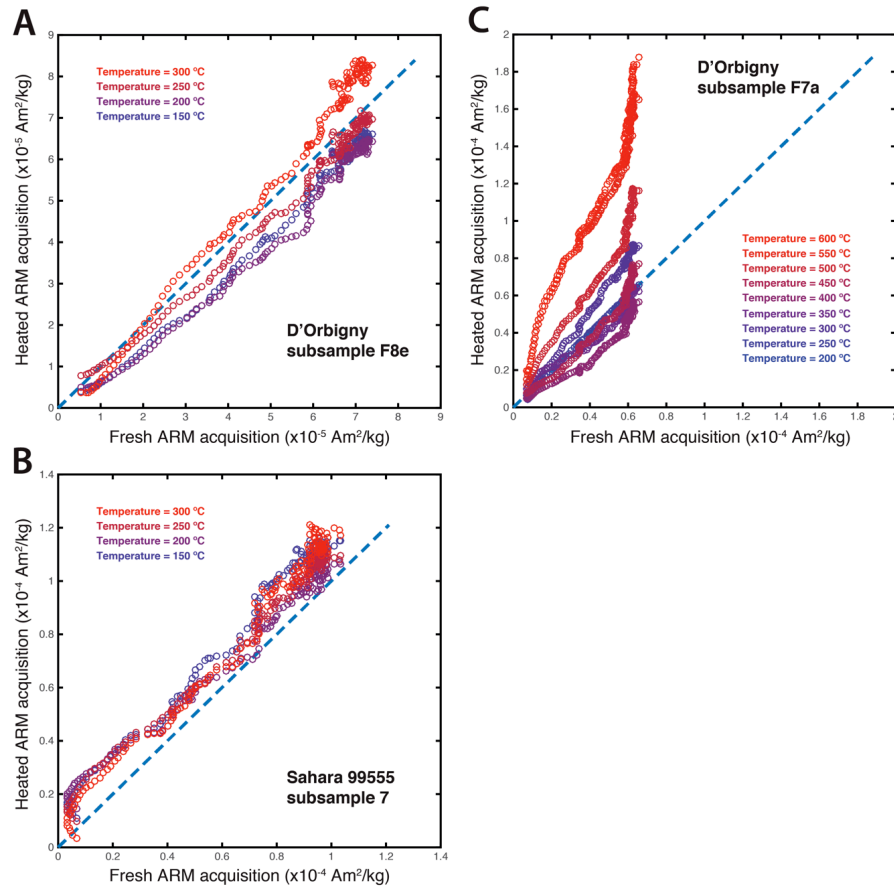
ARM thermal stability tests. Shown in is progressive ARM acquisition in a bias field of 50 µT of samples previously heated to various temperatures (given by various colors) versus progressive ARM acquisition in a bias field of 50 µT of the samples prior to any heating. **(A)** D'Orbigny subsample F8e. **(b)** Sahara 99555 subsample 7. **(C)** D'Orbigny subsample F7a. For (A) and (B), the heating steps were the pTRM acquisition experiments shown in Figure 2C and D. These pTRMs were AF demagnetized to 145 mT prior to conducting the ARM acquisitions shown here. Curves lying along the dashed blue reference line (slope of 1) are consistent with little thermal alteration.

Fig. S16
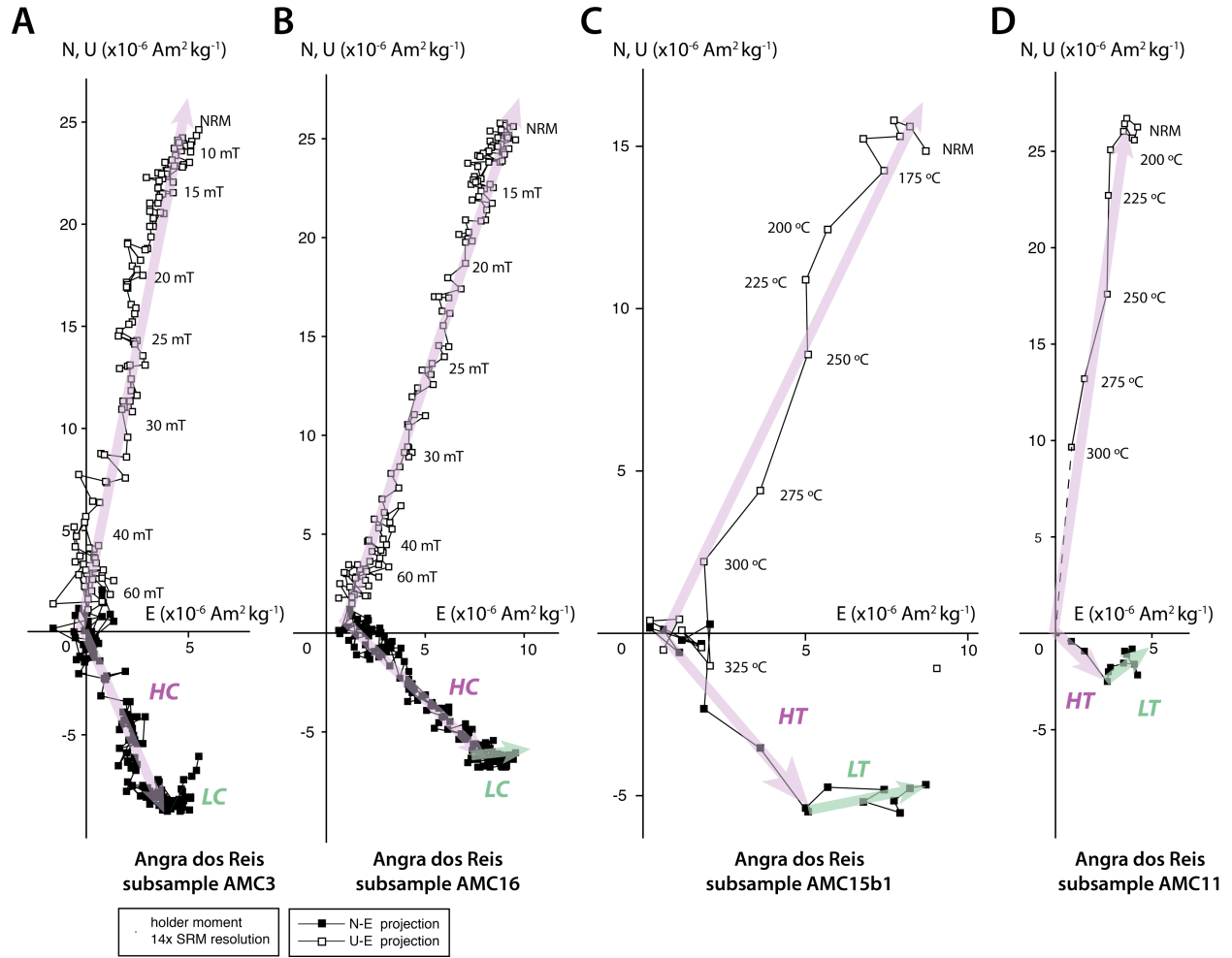
Paleomagnetic analyses of Angra dos Reis. **(A, B)** Two-dimensional projection of the endpoints of the NRM vector during progressive AF demagnetization for Angra dos Reis subsamples AMC3 (58 mg) and AMC16 (76 mg), respectively. Data from Weiss et al. (*18*). **(C)** Thermal demagnetization for Angra dos Reis subsample AMC15b1 (52 mg) in IW conditions. **(D)** Thermal demagnetization for Angra dos Reis subsample AMC11 (37 mg) in IW-1 conditions. Open (filled) symbols represent projections on the up-east (U-E) and north-east (N-E) planes. Small square in bottom legend denotes the moment per unit mass of sample (for 37 mg sample) of the sample holder (i.e., GE 124 quartz glass sample mounts and quartz glass sample handling rod), which is ~14 times of the intrinsic resolution of the MIT SRM (Section A3.1 and Fig. S5). Selected AF and thermal demagnetization steps are labeled. Green arrows show LC/LT components, purple arrows show HC/HT components.

Fig. S17
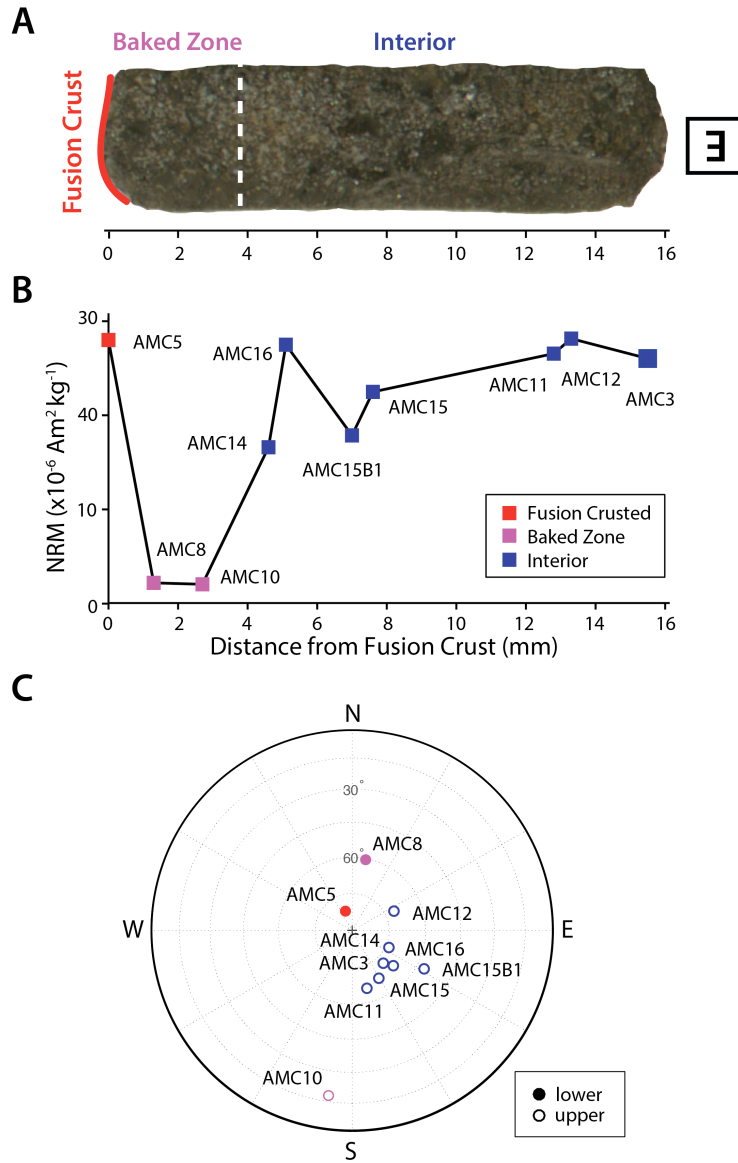
Fusion crust test for Angra dos Reis. (A) Main mass (sample AMC) of Angra dos Reis used for paleomagnetic studies by this study and by Weiss et al. (*18*). Shown here are the fusion-crusted exterior (<1 mm depth), baked zones (~1-3.5 mm depth) and unbaked interior (>3.5 mm depth). Letter in box represent orientation cube, which indicates meteorite orientation in mutual coordinate (E for East). **(B)** Mass-normalized NRM intensity of subsamples from fusion crust (red), baked zone (purple) and interior (blue) of sample shown in (A). **(C)** NRM directions of subsamples of subsamples in (B). Filled (open) symbols indicate downward (upward) directions. Subsample masses are 10 mg for AMC5, 37 mg for AMC8, 45 mg for AMC10, 73 mg for AMC14, 76 mg for AMC16, 52 mg for AMC15B1, 354 mg for AMC15, 37 mg for AMC11, 10 mg for AMC12, and 58 mg for AMC3.
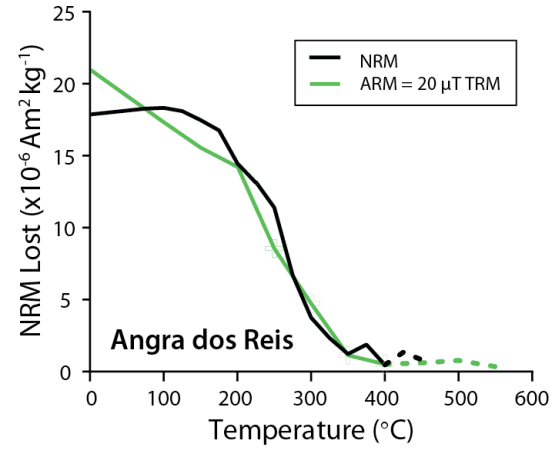
NRM and ARM thermal demagnetization spectra of Angra dos Reis. Thermal demagnetization spectra of NRM (black) and ARM (green: ARMs were imparted with a 260 mT AF in a 100-µT bias field, then divided by 2.5 to normalize to equivalent total TRM acquired in a 20-µT field, based on a TRM/ARM ratio of 2) for Angra dos Reis subsamples AMC15b1 (NRM, 52 mg) and M1b (ARM, 455 mg), respectively.

Fig. S19
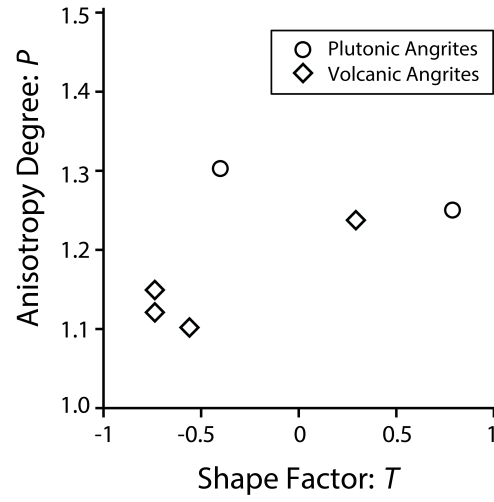
Anisotropy of ARM for angrites. Anisotropy degree (P) versus shape factor (T). Circles represent Angra dos Reis subsamples M1b (455 mg) and M9 (138 mg), diamonds represent D'Orbigny subsamples F7g (155 mg) and F8g (176 mg) and Sahara 99555 subsamples 3b (173 mg) and 6d (101 mg).

Fig. S20
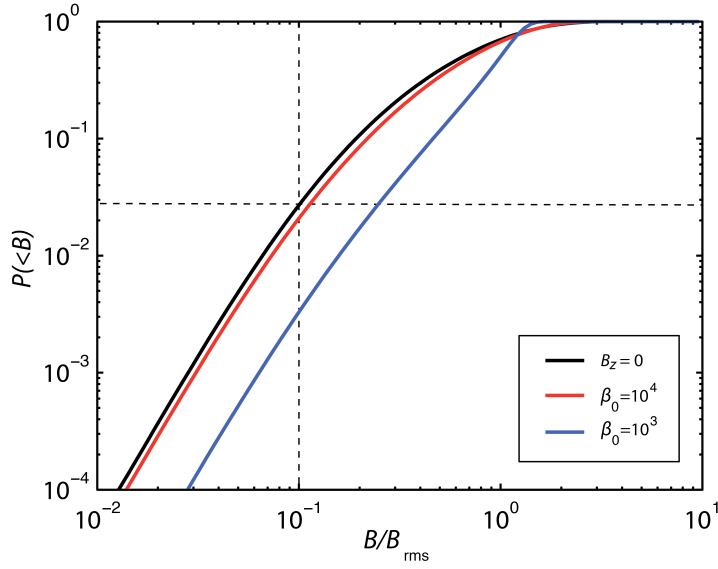
Solar nebula magnetic field model results. CPDF of magnetic field strength from the MRI turbulence, where field strength is normalized to the root-mean-square (rms) field strength. The three curves are based on MRI simulations with zero net vertical magnetic field (black line), weak net vertical field characterized by $\beta_0 = 10^4$ (red line) and stronger net vertical field with $\beta_0 = 10^3$ (blue line). Dashed lines mark that the probability of having $B < 0.1\ B_{rms}$ in any individual angrite is less than ~0.027.

Table S1. Magnetic hysteresis parameters, ARM paleointensity calibration factor (*f'*) and IRM paleointensity calibration factor (*a*) values for Galapagos lavas and angrites. The first column gives subsample name, the second column gives the subsample weight, the third column gives the ratio of saturation remanent magnetization (M_r) and saturation magnetization (M_s), the fourth column gives the coercivity (B_c), the fifth columns give the reference for the hysteresis data in the previous columns, the sixth column gives the TRM to ARM ratio for the HC AF range (50 mT to 145 mT for Galapagos lavas), which is used as ARM paleointensity calibration factor *f'*, and the seventh column gives the IRM paleointensity calibration factor *a*.

Specimen	Weight (mg)	M_r/M_s	B_c (mT)	Reference	f'^{*}	$a^{\dagger}$
Galapagos lava GA78.5	66	0.22	15.9	(*84*)	5.0	875
Galapagos lava GA79.4	14	0.20	12.8	(*84*)	6.4	1457
Galapagos lava GA79.5	29	0.12	6.6	(*84*)	3.2	1012
Galapagos lava GA84.1	46	0.29	20.0	(*84*)	3.6	2607
Galapagos lava GA84.6	46	0.26	19.2	(*84*)	9.5	1106
Galapagos lava GA85.4	53	0.21	8.8	(*84*)	4.6	582
D'Orbigny subsample 11	51	0.27	17.5	(*18*)	5	1000
D'Orbigny subsample 12	24	0.26	18.0	(*18*)	5	1000
Sahara 99555 subsample 5a	25	0.24	19.7	this study	5	1000
Asuka 881371 subsample 63	66	0.21	16.3	(*18*)	5	1000
Angra dos Reis subsample M2	90	0.09	13.5	(*18*)	2	3000
Angra dos Reis subsample 3S1	20	0.08	15.0	(*18*)	2	3000

Notes:

[*]A typical value of *f'* = 5, with a lower limit of *f'* = 3.3, is used for the volcanic angrites D'Orbigny, Sahara 99555, and Asuka 881371. A value of *f'* = 2, with an error range of (-33% to +100%), is used for the plutonic angrite Angra dos Reis.

[†]A typical value of *a* = 1000, with an upper limit of *a* = 1500, is used for the volcanic angrites D'Orbigny, Sahara 99555, and Asuka 881371. A value of *a* = 3000, with an error range of (-50% to +50%), is used for the plutonic angrite Angra dos Reis.

The chosen lower limits of *f'* and upper limit of *a* allow the upper limit of ARM and IRM paleointensities to be 50% larger than their typical values by using the chosen typical values of *f'* and *a*, respectively, for the volcanic angrites D'Orbigny, Sahara 99555, and Asuka 881371.

The chosen relative error ranges of *f'* and upper limit of *a* allow the relative error ranges of ARM and IRM paleointensities to be 50% of their typical values by using the chosen typical values of *f'* and *a*, respectively, for the plutonic angrite Angra dos Reis.

Table S2. NRM components inferred from PCA and associated paleointensities for D'Orbigny. The first column gives subsample name, the second column gives the mass, the third column gives the component (coercivity interval) names, the fourth and fifth columns give the starting and ending demagnetization steps, the sixth column gives the number of data points used in the component, the seventh column indicates whether the PCA fit is anchored to origin (ATO: Y for yes; N for no), and the eighth through tenth columns give the declination, inclination, and maximum angular deviation (MAD) values for the PCA fits (*69*). The eleventh through thirteenth columns give ΔNRM (the demagnetized portion of NRM during the specific AF interval), SIRM (saturation isothermal remanent magnetization), IRM$_{LC}$ (the IRM acquired by the subsample at a field level equivalent to the peak AF level of the LC component), the IRM pint (IRM paleointensity estimate, P_{IRM}), and the ARM pint (ARM paleointensity estimate, P_{ARM}). The uncertainty ranges are the 95% confidence intervals for a two-tailed Student's *t*-test. All nine D'Orbigny subsamples subjected to AF demagnetization are used in the HC vector mean values calculation. The ARM and IRM paleointensities were calculated using *f'* = 5 and *a* = 1000, respectively.

Subsample	Mass (mg)	Comp.	Start	End	N	ATO	Dec. (°)	Inc. (°)	MAD (°)	ΔNRM (10^{-6} Am²/kg)	IRM$_{LC}$ (10^{-6} Am²/kg)	ΔNRM/IRM$_{LC}$ ratio
F7a	182	LC	0 mT	5 mT	10	N	103.9	75.3	8.9	14.43	23.35	0.62
F7b1	70	LC	0 mT	6.5 mT	13	N	55.6	45.9	5.5	-	-	-
F7b2	102	LC	0 mT	5 mT	10	N	65.1	42.7	4.3	-	-	-
F7e	205	LC	0 mT	4 mT	8	N	253.8	22.5	9.4	7.22	7.61	0.95
F7g*	155	LC	0 mT	6 mT	18	N	67.3	36.4	12.4	22.62	-	-
F7i	81	LC	0 mT	6 mT	12	N	38.4	39.4	3.5	45.55	37.70	1.21
F8e*	266	LC	0 mT	9.5 mT	19	N	80.7	18.7	5.9	44.52	-	-
F8g*	176	LC	0 mT	7 mT	14	N	66.5	-7.6	13.6	19.02	-	-
F8i	33	LC	0 mT	6.5 mT	13	N	300.8	35.2	12.9	12.45	67.07	0.19
F8j*	238	LC	0 mT	7 mT	14	N	70.3	8.0	9.0	22.23	-	-
F8n	98	LC	0 mT	5 mT	10	N	309	45.3	11.4	12.30	41.20	0.30

Subsample	Mass (mg)	Comp.	Start	End	N	ATO	Dec. (°)	Inc. (°)	MAD (°)	ΔNRM (10^{-6} Am²/kg)	IRM pint (µT)	ARM pint (µT)
F7a	182	MC	5 mT	45 mT	61	Y	155	-10.5	11.3	23.88	3.9 ± 0.3	5.2 ± 0.4
F7b1	70	MT	10 mT	225 ºC	7	Y	131.2	-18.5	11.0	-	-	-
F7b2	102	MT	8 mT	125 ºC	7	Y	126	22.5	23.1	-	-	-
F7e	205	MC	4 mT	65 mT	84	Y	151.5	-4.6	12.4	22.51	2.0 ± 0.2	2.4 ± 0.3
F7g*	155	MC	6 mT	64 mT	78	Y	141.8	-14.6	10.0	25.80	3.6* ± 0.2	4.4 ± 0.2
F7i	81	MC	6 mT	40 mT	54	Y	176.3	14.1	20.0	6.26	1.0 ± 0.5	2.1 ± 0.4
F8e*	266	MC	9.5 mT	65 mT	72	Y	163.7	-8.2	12.2	13.19	2.1* ± 0.2	2.6 ± 0.2
F8g*	176	MC	11 mT	68 mT	72	Y	144.6	23.9	18.8	14.04	2.2* ± 0.2	2.9 ± 0.3
F8i	33	MC	6.5 mT	63 mT	59	Y	106.1	6.0	26.3	17.13	1.4 ± 0.3	2.0 ± 0.4
F8j*	238	MC	12 mT	58 mT	60	Y	154.9	-5.6	11.7	15.85	2.4* ± 0.2	3.3 ± 0.3
F8n	98	MC	8 mT	65 mT	75	Y	106.2	-13.4	19.4	24.24	2.5 ± 0.3	3.5 ± 0.4

Subsample	Mass (mg)	Comp.	Start	End	N	ATO	Dec. (°)	Inc. (°)	MAD (°)	SIRM (10^{-3} Am²/kg)	IRM pint (µT)	ARM pint (µT)
F7a	182	HC	45 mT	145 mT	81	Y	198.9	-41.2	39.0	8.19	0.4 ± 0.6	0.1 ± 0.7
F7b1	70	HT	225 ºC	575 ºC	15	Y	333.9	5.3	25.0	-	-	-
F7b2	102	HT	125 ºC	600 ºC	19	Y	52.5	-17.2	49.6	-	-	-
F7e	205	HC	65 mT	145 mT	61	Y	57.5	-36.1	46.5	9.80	-0.2 ± 1.0	-0.3 ± 0.7
F7g*	155	HC	64 mT	145 mT	62	Y	121.9	10.6	30.4	8.83*	0.8* ± 1.0	0.0 ± 0.7
F7i	81	HC	40 mT	145 mT	86	Y	160.1	48.4	47.3	7.08	0.9 ± 0.8	0.7 ± 0.8
F8e*	266	HC	65 mT	145 mT	61	Y	174.6	32.2	27.3	8.83*	0.7* ± 0.8	0.5 ± 0.6
F8g*	176	HC	68 mT	145 mT	58	Y	108.8	33.4	23.6	8.83*	0.6* ± 1.1	0.5 ± 0.8
F8i	33	HC	63 mT	145 mT	63	Y	162.5	-10.7	29.7	9.18	0.3 ± 1.2	-0.3 ± 0.8
F8j*	238	HC	58 mT	145 mT	68	Y	287.1	-16.9	29.4	8.83*	0.4* ± 0.6	0.4 ± 0.6
F8n	98	HC	65 mT	145 mT	61	Y	148.1	-13.2	43.2	9.88	0.4 ± 0.9	0.7 ± 0.9
HC vector mean values											*<0.3*	*< 0.2*

Notes:
[*]Paleointensities for these samples computed using average ARM and IRM values shown in Fig. S9.

Table S3. NRM components inferred from PCA and associated paleointensities for Sahara 99555 interior subsamples. Definitions are the same as in Table S2. Three Sahara 99555 subsamples (subsamples 7, 8a and 10b) are used in the HC vector mean values calculation.

Subsample	Mass (mg)	Comp.	Start	End	N	ATO	Dec. (°)	Inc. (°)	MAD (°)	ΔNRM (10^{-6} Am^2/kg)	IRM$_{LC}$ (10^{-6} Am^2/kg)	ΔNRM/IRM$_{LC}$ ratio
7	144	LC	0 mT	6 mT	12	N	197.7	30.4	5.6	53.07	106.87	0.50
8a*	106	LC	0 mT	10 mT	19	N	198.1	29.0	2.3	230.62	-	-
9a	72	LC	0 mT	10 mT	20	N	195.2	19.6	3.9	-	-	-
9b	83	LC	0 mT	9 mT	19	N	206.7	27.6	6.4	-	-	-
10a	100	LC	0 mT	10 mT	20	N	199.2	13.2	2.6	256.45	358.72	0.71
10b*	39	LC	0 mT	8 mT	15	N	209.8	24.1	6.2	143.80	-	-
										ΔNRM (10^{-6} Am^2/kg)	IRM pint (µT)	ARM pint (µT)
7	144	MC	6 mT	50 mT	64	Y	241.4	4.4	17.0	24.24	1.9 ± 0.2	2.6 ± 0.3
8a*	106	MC	10 mT	50 mT	56	Y	258.9	5.5	23.1	17.35	1.1* ± 0.3	1.4* ± 0.4
9a	72	MT	100 °C	375 °C†	13	Y	270.5	9.0	22.4	-	-	-
9b	83	MT	100 °C	425 °C†	16	Y	259.7	38.4	23.0	-	-	-
10a	100	MC	10 mT	145 mT	131	Y	246.9	39.2	14.6	25.24	2.5 ± 0.1	3.6 ± 0.2
10b*	39	MC	8 mT	47 mT	57	Y	264.7	7.1	21.0	23.90	2.0* ± 0.4	2.5 ± 0.5
										SIRM (10^{-3} Am^2/kg)	IRM pint (µT)	ARM pint (µT)
7	144	HC	50 mT	145 mT	76	Y	180.6	38.1	29.0	15.13	-0.4 ± 0.7	-0.1 ± 0.6
8a*	106	HC	50 mT	145 mT	76	Y	0.6	-8.7	46.2	14.73*	0.6* ± 0.8	0.1* ± 0.9
9a	72	HT	375 °C	600 °C	9	Y	208.8	8.0	37.8	-	-	-
9b	83	HT	425 °C	550 °C	11	Y	267.9	20.0	44.3	-	-	-
10a	100	-	-	-	-	-	-	-	-	14.33	-	-
10b*	39	HC	47 mT	145 mT	79	Y	243.6	-17.1	35.9	14.73*	0.1* ± 1.0	0.1* ± 1.1
HC vector mean values											*<0.3*	*<0.2*

Notes:
*Paleointensities for these samples computed using average ARM and IRM values shown in Fig. S9.
†Most unblocking occurred below 200 ºC, but a small unblocking tail continued up to these higher temperatures.

Table S4. Paleointensities for MT components by the pTRM Shaw method. The first column gives subsample name, the second column gives the pTRM paleointensity assuming sample was partially heated to 150 ºC, the third column gives the pTRM paleointensity assuming sample was partially heated to 200 ºC, the fourth column gives the pTRM paleointensity assuming sample was partially heated to 250 ºC, the fifth column gives the pTRM paleointensity assuming sample was partially heated to 300 ºC, the sixth column gives the mean pTRM paleointensity from the values in third through fifth columns (temperature ranges from 200 ºC to 300 ºC). The bottom row gives the overall mean pTRM paleointensity for these three volcanic angrite subsamples from 200 ºC to 300 ºC.

Subsample	150 ºC pint (µT)	200 ºC pint (µT)	250 ºC pint (µT)	300 ºC pint (µT)	200-300 ºC mean pTRM pint (µT)
D'Orbigny subsample F7a	-	9.9	7.5	7.1	8.2 ± 1.5
D'Orbigny subsample F8e	21.7	8.8	6.2	5.0	6.6 ± 2.0
Sahara 99555 subsample 7	23.0	12.1	9.0	7.5	9.5 ± 2.3
Mean pTRM paleointensity					**8.1 ± 1.4**

Table S5. Paleointensities from Thellier-Thellier experiments and their quality criteria. The first column gives subsample name, the second column gives the mass, the third column gives the temperature range used to calculate paleointensity, the fourth column gives the paleointensity (uncertainty ranges are the 95% confidence intervals for a two-tailed Student's t-test), the fifth column gives the number of points used to estimate paleointensity, the sixth column gives the NRM fraction used for the best-fit on an Arai diagram, the seventh column gives the gap factor that measures the average NRM lost between successive temperature steps of the segment chosen for the best-fit line on the Arai plot, the eighth column gives β, a measure of the relative data scatter around the best-fit line (equal to the ratio of the standard error of the slope to the absolute value of the slope), the ninth column gives the quality factor that measures the overall quality of the paleointensity estimate (i.e., combines the relative scatter of the best-fit line, the NRM fraction, and the gap factor), the tenth column gives n, the number of pTRM checks used for the best-fit segment, the eleventh column gives δCK, the maximum absolute difference produced by a pTRM check, normalized by the estimated total TRM, the twelfth column gives $DRAT$ (difference ratio), the maximum absolute difference produced by a pTRM check, normalized by the length of the best-fit line, the thirteenth column gives $CDRAT$, the cumulative DRAT (*150, 151*). We do not calculate δCK for the HT range because the slightly negative slopes of the best-fit lines on the Arai plot, which would imply low total TRMs, render this statistic meaningless.

Subsample	Weight (mg)	Temperature Range	Calibrated Paleointensity (μT)	N	f	g	β	q	n	δCK (%)	DRAT (%)	CDRAT (%)
DORBF7f*	154	100 - 175 ºC	11.7 ± 4.3	4	0.43	0.52	0.20	1.10	2	3.3	6.3	7.6
DORBF7h2	113	100 - 175 ºC	13.9 ± 1.1	4	0.54	0.64	0.04	7.88	2	7.9	12.0	8.8
DORBF8m*	199	100 - 175 ºC	12.1 ± 0.8	4	0.54	0.65	0.04	8.99	2	4.2	6.7	9.6
SAH99555,6a*	101	100 - 200 ºC	7.0 ± 2.6	5	0.64	0.70	0.21	2.15	3	3.3	5.1	5.3

Notes:
[*]These paleointensities pass typical thermochemical alteration criteria established for Earth rocks (i.e., $\delta CK < 7\%$, DRAT < 10%, and CDRAT < 10%) [see ref. (*151*)].

References

1. N. J. Turner *et al*., in *Protostars and Planets VI,* H. Beuther, R. S. Klessen, C. P. Dullemond, T. Henning, Eds. (University of Arizona Press, Tucson, 2014), pp. 411–432.

2. C. P. McNally, A. Hubbard, C.-C. Yang, M.-M. Mac Low, Temperature fluctuations driven by magnetorotational instability in protoplanetary disk. *Astrophys. J.* **791**, 62 (2014). doi:10.1088/0004-637X/791/1/62

3. A. Johansen, M.-M. Mac Low, P. Lacerda, M. Bizzarro, Growth of asteroids, planetary embryos, and Kuiper belt objects by chondrule accretion. *Sci. Adv.* **1**, e1500109 (2015). doi:10.1126/sciadv.1500109 Medline

4. I. W. Stephens, L. W. Looney, W. Kwon, M. Fernández-López, A. M. Hughes, L. G. Mundy, R. M. Crutcher, Z.-Y. Li, R. Rao, Spatially resolved magnetic field structure in the disk of a T Tauri star. *Nature* **514**, 597–599 (2014). doi:10.1038/nature13850 Medline

5. R. R. Fu, B. P. Weiss, E. A. Lima, R. J. Harrison, X.-N. Bai, S. J. Desch, D. S. Ebel, C. Suavet, H. Wang, D. Glenn, D. Le Sage, T. Kasama, R. L. Walsworth, A. T. Kuan, Paleomagnetism. Solar nebula magnetic fields recorded in the Semarkona meteorite. *Science* **346**, 1089–1092 (2014). doi:10.1126/science.1258022 Medline

6. J. N. Connelly, M. Bizzarro, A. N. Krot, Å. Nordlund, D. Wielandt, M. A. Ivanova, The absolute chronology and thermal processing of solids in the solar protoplanetary disk. *Science* **338**, 651–655 (2012). doi:10.1126/science.1226919 Medline

7. R. Alexander, I. Pascucci, S. Andrews, P. Armitage, L. Cieza, in *Protostars and Planets VI,* H. Beuther, R. S. Klessen, C. P. Dullemond, T. Henning, Eds. (University of Arizona Press, Tucson, 2014), pp. 475–496.

8. T. Takeuchi, P. Artymowicz, Dust migration and morphology in optically thin circumstellar gas disks. *Astrophys. J.* **557**, 990–1006 (2001). doi:10.1086/322252

9. J. Kominami, S. Ida, Formation of terrestrial planets in a dissipating gas disk with Jupiter and Saturn. *Icarus* **167**, 231–243 (2004). doi:10.1016/j.icarus.2003.10.005

10. R. Helled *et al*., in *Protostars and Planets VI,* H. Beuther, C. P. Dullemond, R. S. Klessen, T. K. Henning, Eds. (University of Arizona Press, Tucson, 2014), pp. 643–666.

11. M. Chaussidon, M.-C. Liu, in *The Early Earth: Accretion and Differentiation,* J. Badro, M. Walter, Eds. (American Geophysical Union, Washington, D. C., 2015), pp. 1–26.

12. F. A. Podosek, P. Cassen, Theoretical, observational, and isotopic estimates of the lifetime of the solar nebula. *Meteoritics* **29**, 6–25 (1994). doi:10.1111/j.1945-5100.1994.tb00649.x

13. C. P. M. Bell, T. Naylor, N. J. Mayne, R. D. Jeffries, S. P. Littlefair, Pre-main-sequence isochrones – II. Revising star and planet formation time-scales. *Mon. Not. R. Astron. Soc.* **434**, 806–831 (2013). doi:10.1093/mnras/stt1075

14. E. E. Mamajek, in *Exoplanets and Disks: Their Formation and Diversity,* T. Usuda, M. Ishii, M. Tamura, Eds. (2009), vol. 1158, pp. 3–10.

15. K. Keil, Angrites, a small but diverse suite of ancient, silica-undersaturated volcanic-plutonic mafic meteorites, and the history of their parent asteroid. *Chem. Erde Geochem.* **72**, 191–218 (2012). doi:10.1016/j.chemer.2012.06.002

16. B. P. Weiss, J. Gattacceca, S. Stanley, P. Rochette, U. R. Christensen, Paleomagnetic records of meteorites and early planetesimal differentiation. *Space Sci. Rev.* **152**, 341–390 (2010). doi:10.1007/s11214-009-9580-z

17. L. T. Elkins-Tanton, B. P. Weiss, M. T. Zuber, Chondrites as samples of differentiated planetesimals. *Earth Planet. Sci. Lett.* **305**, 1–10 (2011). doi:10.1016/j.epsl.2011.03.010

18. B. P. Weiss, J. S. Berdahl, L. Elkins-Tanton, S. Stanley, E. A. Lima, L. Carporzen, Magnetism on the angrite parent body and the early differentiation of planetesimals. *Science* **322**, 713–716 (2008). doi:10.1126/science.1162459 Medline

19. J. H. Roberts, A. S. Rivkin, N. L. Chabot, Thermal challenges for recording an ancient core dynamo on Vesta. *Workshop on Planetesimal Formation and Differentiation* **1768**, abstract #8033 (2013).

20. M. G. Sterenborg, J. W. Crowley, Thermal evolution of early solar system planetesimals and the possibility of sustained dynamos. *Phys. Earth Planet. Inter.* **214**, 53–73 (2013). doi:10.1016/j.pepi.2012.10.006

21. S. J. McKibbin, T. R. Ireland, Y. Amelin, P. Holden, Mn-Cr dating of Fe- and Ca-rich olivine from 'quenched' and 'plutonic' angrite meteorites using Secondary Ion Mass Spectrometry. *Geochim. Cosmochim. Acta* **157**, 13–27 (2015). doi:10.1016/j.gca.2015.02.019

22. T. Mikouchi, M. Miyamoto, G. McKay, L. Le, Cooling rate experiments of quenched angrites: Approaches by crystallization experiments and cooling rate calculations of olivine xenocrysts. *Meteorit. Planet. Sci.* **36** (Suppl.), A134 (2001).

23. P. H. Warren, Stable-isotopic anomalies and the accretionary assemblage of the Earth and Mars: A subordinate role for carbonaceous chondrites. *Earth Planet. Sci. Lett.* **311**, 93–100 (2011). doi:10.1016/j.epsl.2011.08.047

24. Y. Amelin, M. Sapah, Cooling rates of plutonic angrites from pyroxene-phosphate U-Pb geochronology. *Met. Soc. Abs.* **75**, 5199 (2012).

25. A. R. Sarafian *et al.*, Wet angrites? A D/H and Pb-Pb study of silicates and phosphates. *Lunar Planet Sci. Conf. XLVI*, abs. #1542 (2015).

26. H. Busemann, S. Lorenzetti, O. Eugster, Noble gases in D'Orbigny, Sahara 99555 and D'Orbigny glass - Evidence for early planetary processing on the angrite parent body. *Geochim. Cosmochim. Acta* **70**, 5403–5425 (2006). doi:10.1016/j.gca.2006.08.015

27. Materials and methods are available as supplementary materials.

28. C. Suavet, B. P. Weiss, T. L. Grove, Controlled-atmosphere thermal demagnetization and paleointensity analyses of extraterrestrial rocks. *Geochem. Geophys. Geosyst.* **15**, 2733–2743 (2014). doi:10.1002/2013GC005215

29. J. Shaw, A new method of determining the magnitude of the palaeomagnetic field: Application to five historic lavas and five archaeological samples. *Geophys. J. Int.* **39**, 133–141 (1974). doi:10.1111/j.1365-246X.1974.tb05443.x

30. L. Tauxe, H. Staudigel, Strength of the geomagnetic field in the Cretaceous Normal Superchron: New data from submarine basaltic glass of the Troodos Ophiolite. *Geochem. Geophys. Geosyst.* **5**, Q02H06 (2004). doi:10.1029/2003GC000635

31. One Sahara 99555 subsample was stable to >145 mT. The two thermally demagnetized Sahara 99555 samples exhibited a small amount of additional unblocking (equal to 5 to 10% of NRM) up to ~375° to 425 °C.

32. G. Lesur, M. W. Kunz, S. Fromang, Thanatology in protoplanetary discs: The combined influence of Ohmic, Hall, and ambipolar diffusion on dead zones? *Astron. Astrophys.* **566**, A56 (2014). doi:10.1051/0004-6361/201423660

33. X. N. Bai, Hall-effect-controlled gas dynamics in protoplanetary disks. I. Wind solutions at the inner disk. *Astrophys. J.* **791**, 137 (2014). doi:10.1088/0004-637X/791/2/137

34. R. P. Nelson, O. Gressel, O. M. Umurhan, Linear and non-linear evolution of the vertical shear instability in accretion discs. *Mon. Not. R. Astron. Soc.* **435**, 2610–2632 (2013). doi:10.1093/mnras/stt1475

35. W. Kley, R. P. Nelson, Planet-disk interaction and orbital evolution. *Annu. Rev. Astron. Astrophys.* **50**, 211–249 (2012). doi:10.1146/annurev-astro-081811-125523

36. K. J. Walsh, A. Morbidelli, S. N. Raymond, D. P. O'Brien, A. M. Mandell, A low mass for Mars from Jupiter's early gas-driven migration. *Nature* **475**, 206–209 (2011). doi:10.1038/nature10201 Medline

37. E. R. D. Scott, in. *Annu. Rev. Earth Planet. Sci.* **35**, 577–620 (2007). doi:10.1146/annurev.earth.35.031306.140100

38. A. N. Krot, Y. Amelin, P. Cassen, A. Meibom, Young chondrules in CB chondrites from a giant impact in the early solar system. *Nature* **436**, 989–992 (2005). doi:10.1038/nature03830 Medline

39. S. J. Desch, H. C. Connolly Jr., A model of the thermal processing of particles in solar nebula shocks: Application to the cooling rates of chondrules. *Meteorit. Planet. Sci.* **37**, 183–207 (2002). doi:10.1111/j.1945-5100.2002.tb01104.x

40. F. H. Shu, H. Shang, T. Lee, Toward an astrophysical theory of chondrites. *Science* **271**, 1545–1552 (1996). doi:10.1126/science.271.5255.1545

41. W. Neumann, D. Breuer, T. Spohn, Differentiation of Vesta: Implications for a shallow magma ocean. *Earth Planet. Sci. Lett.* **395**, 267–280 (2014). doi:10.1016/j.epsl.2014.03.033

42. M. Schiller, J. N. Connelly, A. C. Glad, T. Mikouchi, M. Bizzarro, Early accretion of protoplanets inferred from a reduced inner solar system ^{26}Al inventory. *Earth Planet. Sci. Lett.* **420**, 45–54 (2015). doi:10.1016/j.epsl.2015.03.028 Medline

43. M. Prinz, K. Keil, P. F. Hlava, J. L. Berkley, C. B. Gomes, W. S. Curvello, Studies of Brazilian meteorites. III. Origin and history of Angra dos Reis achondrite. *Earth Planet. Sci. Lett.* **35**, 317–330 (1977). doi:10.1016/0012-821X(77)90134-0

44. P. H. Warren, A. M. Davis, Consortium investigation of the Asuka-881371 angrite: Petrographic electron microprobe and ion microprobe observations Meteorites. *Antarct. Meteorites* **XX**, 257 (1995).

45. D. W. Strangway, E. E. Larson, G. W. Pearce, Magnetic studies of lunar samples - breccia and fines. *Proc. Apollo 11 Lunar Sci. Conf.* **1**, 2435 (1970).

46. D. J. Dunlop, Theory and application of the Day plot (Mrs/Ms versus Hcr/Hc) 1. Theoretical curves and tests using titanomagnetite data. *J. Geophys. Res.* **107** (B3), 2056 (2002). doi:10.1029/2001JB000486

47. D. J. Dunlop, Theory and application of the Day plot (Mrs/Ms versus Hcr/Hc) 2. Application to data for rocks, sediments, and soils. *J. Geophys. Res.* **107**, 10.1029/2001JB000487 (2002).

48. P. Rochette, J. Gattacceca, M. Bourot-Denise, G. Consolmagno, L. Folco, T. Kohout, L. Pesonen, L. Sagnotti, Magnetic classification of stony meteorites: 3. Achondrites. *Meteorit. Planet. Sci.* **44**, 405–427 (2009). doi:10.1111/j.1945-5100.2009.tb00741.x

49. A. P. Roberts, C. R. Pike, K. L. Verosub, First-order reversal curve diagrams: A new tool for characterizing the magnetic properties of natural samples. *J. Geophys. Res.* **105** (B12), 28461–28475 (2000). doi:10.1029/2000JB900326

50. C. R. Pike, A. P. Roberts, K. L. Verosub, Characterizing interactions in fine magnetic particle systems using first order reversal curves. *J. Appl. Phys.* **85**, 6660–6667 (1999). doi:10.1063/1.370176

51. H. Wang, D. V. Kent, M. J. Jackson, Evidence for abundant isolated magnetic nanoparticles at the Paleocene-Eocene boundary. *Proc. Natl. Acad. Sci. U.S.A.* **110**, 425–430 (2013). doi:10.1073/pnas.1205308110 Medline

52. G. Cromwell, L. Tauxe, S. A. Halldórsson, New paleointensity results from rapidly cooled Icelandic lavas: Implications for Arctic geomagnetic field strength. *J. Geophys. Res.* **120**, 2913–2934 (2015). doi:10.1002/2014JB011828

53. R. J. Harrison, J. M. Feinberg, FORCinel: An improved algorithm for calculating first-order reversal curve distributions using locally weighted regression smoothing. *Geochem. Geophys. Geosyst.* **9**, Q05016 (2008). doi:10.1029/2008GC001987

54. T. P. Almeida *et al.*, Observing thermomagnetic stability of nonideal magnetite particles: Good paleomagnetic recorders? *Geochem. Geophys. Geosyst.* **41**, 7041 (2014).

55. T. P. Almeida, A. R. Muxworthy, A. Kovács, W. Williams, P. D. Brown, R. E. Dunin-Borkowski, Direct visualization of the thermomagnetic behavior of pseudo-single-domain magnetite particles. *Sci. Adv.* **2**, e1501801 (2016). doi:10.1126/sciadv.1501801 Medline

56. J. F. Einsle, R. J. Harrison, T. Kasama, P. Ó. Conbhuí, K. Fabian, W. Williams, L. Woodland, R. R. Fu, B. P. Weiss, P. A. Midgley, Multi-scale three-dimensional characterisation of iron particles in dusty olivine: Implications for paleomagnetism of chondritic meteorites. *Am. Mineral.* **101**, 2070–2084 (2016). doi:10.2138/am-2016-5738CCBY

57. J. A. Tarduno, R. D. Cottrell, M. K. Watkeys, A. Hofmann, P. V. Doubrovine, E. E. Mamajek, D. Liu, D. G. Sibeck, L. P. Neukirch, Y. Usui, Geodynamo, solar wind, and magnetopause 3.4 to 3.45 billion years ago. *Science* **327**, 1238–1240 (2010). doi:10.1126/science.1183445 Medline

58. A. Biggin, M. J. de Wit, C. G. Langereis, T. E. Zegers, S. Voûte, M. J. Dekkers, K. Drost, Palaeomagnetism of Archaean rocks of the Onverwacht Group, Barberton Greenstone Belt (southern Africa): Evidence for a stable and potentially reversing geomagnetic field

at ca. 3.5 Ga. *Earth Planet. Sci. Lett.* **302**, 314–328 (2011). doi:10.1016/j.epsl.2010.12.024

59. A. Yoshihara, Y. Hamano, Paleomagnetic constraints on the Archean geomagnetic field intensity obtained from komatiites of the Barberton and Belingwe greenstone belts, South Africa and Zimbabwe. *Precambrian Res.* **131**, 111–142 (2004). doi:10.1016/j.precamres.2004.01.003

60. V. V. Shcherbakova, V. P. Shcherbakov, G. V. Zhidkov, N. V. Lubnina, Palaeointensity determinations on rocks from Palaeoproterozoic dykes from the Kaapvaal Craton (South Africa). *Geophys. J. Int.* **197**, 1371–1381 (2014). doi:10.1093/gji/ggu098

61. M. Macouin, J. P. Valet, J. Besse, K. Buchan, R. Ernst, M. LeGoff, U. Scharer, Low paleointensities recorded in 1 to 2.4 Ga Proterozoic dykes, Superior Province, Canada. *Earth Planet. Sci. Lett.* **213**, 79–95 (2003). doi:10.1016/S0012-821X(03)00243-7

62. N. L. Swanson-Hysell, A. C. Maloof, B. P. Weiss, D. A. D. Evans, No asymmetry in geomagnetic reversals in 1.1-billion-year-old Keweenawan basalt flows. *Nat. Geosci.* **2**, 713 (2009). doi:10.1038/ngeo622

63. J. Wang *et al.*, Automated markerless full field hard x-ray microscopic tomography at sub-50 nm 3-dimension spatial resolution. *Appl. Phys. Lett.* **100**, 4 (2012).

64. H. Wang, J. Wang, Y.-C. K. Chen-Wiegart, D. V. Kent, Quantified abundance of magnetofossils at the Paleocene-Eocene boundary from synchrotron-based transmission x-ray microscopy. *Proc. Natl. Acad. Sci. U.S.A.* **112**, 12598–12603 (2015). doi:10.1073/pnas.1517475112 Medline

65. D. S. McKay, E. K. Gibson Jr., K. L. Thomas-Keprta, H. Vali, C. S. Romanek, S. J. Clemett, X. D. F. Chillier, C. R. Maechling, R. N. Zare, Search for past life on Mars: Possible relic biogenic activity in martian meteorite ALH84001. *Science* **273**, 924–930 (1996). doi:10.1126/science.273.5277.924 Medline

66. D. R. Baker, L. Mancini, M. Polacci, M. D. Higgins, G. A. R. Gualda, R. J. Hill, M. L. Rivers, An introduction to the application of x-ray microtomography to the three-dimensional study of igneous rocks. *Lithos* **148**, 262–276 (2012). doi:10.1016/j.lithos.2012.06.008

67. P. A. O'Day, N. Rivera Jr., R. Root, S. A. Carroll, X-ray absorption spectroscopic study of Fe reference compounds for the analysis of natural sediments. *Am. Mineral.* **89**, 572–585 (2004). doi:10.2138/am-2004-0412

68. J. L. Kirschvink, R. E. Kopp, T. D. Raub, C. T. Baumgartner, J. W. Holt, Rapid, precise, and high-sensitivity acquisition of paleomagnetic and rock-magnetic data: Development of a low-noise automatic sample changing system for superconducting rock magnetometers. *Geochem. Geophys. Geosyst.* **9**, Q05Y01 (2008). doi:10.1029/2007GC001856

69. J. L. Kirschvink, The least-squares line and plane and the analysis of palaeomagnetic data. *Geophys. J. R. Astron. Soc.* **62**, 699–718 (1980). doi:10.1111/j.1365-246X.1980.tb02601.x

70. C. H. Jones, User-driven integrated software lives: "Paleomag" paleomagnetics analysis on the Macintosh. *Comput. Geosci.* **28**, 1145–1151 (2002). doi:10.1016/S0098-3004(02)00032-8

71. A. Stephenson, Gyromagnetism and the remanence acquired by a rotating rock in an alternating field. *Nature* **284**, 48–49 (1980). doi:10.1038/284048a0

72. S. M. Tikoo, B. P. Weiss, J. Buz, E. A. Lima, E. K. Shea, G. Melo, T. L. Grove, Magnetic fidelity of lunar samples and implications for an ancient core dynamo. *Earth Planet. Sci. Lett.* **337-338**, 93–103 (2012). doi:10.1016/j.epsl.2012.05.024

73. S. M. Tikoo, B. P. Weiss, W. S. Cassata, D. L. Shuster, J. Gattacceca, E. A. Lima, C. Suavet, F. Nimmo, M. D. Fuller, Decline of the lunar core dynamo. *Earth Planet. Sci. Lett.* **404**, 89–97 (2014). doi:10.1016/j.epsl.2014.07.010

74. D. J. Dunlop, O. Özdemir, *Rock Magnetism: Fundamentals and Frontiers*. Cambridge Studies in Magnetism (Cambridge University Press, New York, 1997).

75. R. Brett, J. S. Huebner, M. Sato, Measured oxygen fugacities of the Angra dos Reis achondrite as a function of temperature. *Earth Planet. Sci. Lett.* **35**, 363–368 (1977). doi:10.1016/0012-821X(77)90139-X

76. P. L. King *et al.*, Redox history of early solar system planetesimals recorded in the D'Orbigny angrite. *Lunar Planet Sci. Conf. XLIII*, abs. #2346 (2012).

77. G. E. Lofgren, A. B. Lanier, Dynamic crystallization experiments on the Angra dos Reis achondritic meteorite. *Earth Planet. Sci. Lett.* **111**, 455–466 (1992). doi:10.1016/0012-821X(92)90196-3

78. G. S. Watson, A test for randomness. *Mon. Not. R. Astron. Soc.* **7**, 160–161 (1956). doi:10.1111/j.1365-246X.1956.tb05561.x

79. D. J. Dunlop, O. Özdemir, D. A. Clark, P. W. Schmidt, Time-temperature relations for the remagnetization of pyrrhotite (Fe_7S_8) and their use in estimating paleotemperatures. *Earth Planet. Sci. Lett.* **176**, 107–116 (2000). doi:10.1016/S0012-821X(99)00309-X

80. M. Winklhofer, K. Fabian, F. Heider, Magnetic blocking temperatures of magnetite calculated with a three-dimensional micromagnetic model. *J. Geophys. Res.* **102** (B10), 22695–22709 (1997). doi:10.1029/97JB01730

81. A. J. T. Jull, in *Meteorites and the Early Solar System II,* D. S. Lauretta, H. Y. McSween, Eds. (University of Arizona Press, Tucson, 2006), pp. 889–905.

82. Y. Amelin, The U-Pb systematics of angrite Sahara 99555. *Geochim. Cosmochim. Acta* **72**, 4874–4885 (2008). doi:10.1016/j.gca.2008.07.008

83. Y. Yu, Paleointensity determination using anhysteretic remanence and saturation isothermal remanence. *Geochem. Geophys. Geosyst.* **11**, Q02Z12 (2010). doi:10.1029/2009GC002804

84. H. Wang, D. V. Kent, A paleointensity technique for multidomain igneous rocks. *Geochem. Geophys. Geosyst.* **14**, 4195–4213 (2013). doi:10.1002/ggge.20248

85. T. Nagata, Y. Arai, K. Momose, Secular variation of the geomagnetic total force during the last 5000 years. *J. Geophys. Res.* **68**, 5277 (1963). doi:10.1029/JZ068i018p05277

86. K. Lawrence, C. Johnson, L. Tauxe, J. Gee, Lunar paleointensity measurements: Implications for lunar magnetic evolution. *Phys. Earth Planet. Inter.* **168**, 71–87 (2008). doi:10.1016/j.pepi.2008.05.007

87. L. V. de Groot, M. J. Dekkers, T. A. T. Mullender, Exploring the potential of acquisition curves of the anhysteretic remanent magnetization as a tool to detect subtle magnetic alteration induced by heating. *Phys. Earth Planet. Inter.* **194**, 71–84 (2012). doi:10.1016/j.pepi.2012.01.006

88. B. M. Moskowitz, Methods for estimating Curie temperatures of titanomaghemites from experimental Js-T data. *Earth Planet. Sci. Lett.* **53**, 84–88 (1981). doi:10.1016/0012-821X(81)90028-5

89. G. W. Pearce, G. S. Hoye, D. W. Strangway, B. M. Walker, L. A. Taylor, Some complexities in the determination of lunar paleointensities. *Proc. Lunar Planet. Sci. Conf.* **7**, 3271 (1976).

90. E. Von Ludwig, G. Tschermak, XII. Der Meteorit von Angra dos Reis. *Zeitschrift für Kristallographie. Mineralogie und Petrographie* **8**, 341 (1887).

91. P. A. Selkin, J. S. Gee, L. Tauxe, W. P. Meurer, A. J. Newell, The effect of remanence anisotropy on paleointensity estimates: A case study from the Archean Stillwater Complex. *Earth Planet. Sci. Lett.* **183**, 403–416 (2000). doi:10.1016/S0012-821X(00)00292-2

92. V. Jelinek, Characterization to the magnetic fabric of rocks. *Tectonophys.* **79**, T63–T67 (1981). doi:10.1016/0040-1951(81)90110-4

93. H. Palme, D. C. Hezel, D. S. Ebel, The origin of chondrules: Constraints from matrix composition and matrix-chondrule complementarity. *Earth Planet. Sci. Lett.* **411**, 11–19 (2015). doi:10.1016/j.epsl.2014.11.033

94. J. Bollard, J. N. Connelly, M. Bizzarro, The absolute chronology of the early solar system revisited. *77th Annual Meteoritical Society Meeting*, abstract #5234 (2014).

95. L. Schrader *et al.*, Testing the distribution of 26Al in the protoplanetary disk using CR chondrules. *76th Annual Meteoritical Society Meeting*, abstract #5141 (2013).

96. C. Hayashi, Structure of the solar nebula, growth, and decay of magnetic fields and effects of magnetic and turbulent viscosities on the nebula. *Prog. Theor. Phys. Suppl.* **70**, 35–53 (1981). doi:10.1143/PTPS.70.35

97. M. A. Morris, L. A. J. Garvie, L. P. Knauth, New insight into the solar system's transition disk phase provided by the metal-rich carbonaceous chondrite Isheyevo. *Astrophys. J.* **801**, L22 (2015). doi:10.1088/2041-8205/801/2/L22

98. B. C. Johnson, D. A. Minton, H. J. Melosh, M. T. Zuber, Impact jetting as the origin of chondrules. *Nature* **517**, 339–341 (2015). doi:10.1038/nature14105 Medline

99. J. Bollard, J. N. Connelly, M. Bizzarro, Pb-Pb dating of individual chondrules from the CBa chondrite Gujba: Assessment of the impact plume formation model. *Meteorit. Planet. Sci.* **50**, 1197–1216 (2015). doi:10.1111/maps.12461 Medline

100. J. Gattacceca, B. P. Weiss, M. Gounelle, New constraints on the magnetic history of the CV parent body and the solar nebula from the Kaba meteorite. *Earth Planet. Sci. Lett.* **455**, 166–175 (2016). doi:10.1016/j.epsl.2016.09.008

101. A. V. Smirnov, J. A. Tarduno, Thermochemical remanent magnetization in Precambrian rocks: Are we sure the geomagnetic field was weak? *J. Geophys. Res.* **110** (B6), B06103 (2005). doi:10.1029/2004JB003445

102. X. N. Bai, J. Goodman, Heat and dust in active layers of protostellar disks. *Astrophys. J.* **701**, 737–755 (2009). doi:10.1088/0004-637X/701/1/737

103. M. Ilgner, R. P. Nelson, On the ionisation fraction in protoplanetary disks. II. The effect of turbulent mixing on gas-phase chemistry. *Astron. Astrophys.* **445**, 223–232 (2006). doi:10.1051/0004-6361:20053867

104. M. Ilgner, R. P. Nelson, On the ionisation fraction in protoplanetary disks. III. The effect of X-ray flares on gas-phase chemistry. *Astron. Astrophys.* **455**, 731–740 (2006). doi:10.1051/0004-6361:20065308

105. M. Ilgner, R. P. Nelson, On the ionisation fraction in protoplanetary disks. I. Comparing different reaction networks. *Astron. Astrophys.* **445**, 205–222 (2006). doi:10.1051/0004-6361:20053678

106. T. P. Fleming, J. M. Stone, J. F. Hawley, The effect of resistivity on the nonlinear stage of the magnetorotational instability in accretion disks. *Astrophys. J.* **530**, 464–477 (2000). doi:10.1086/308338

107. C. F. Gammie, Layered accretion in T Tauri disks. *Astrophys. J.* **457**, 355 (1996). doi:10.1086/176735

108. T. Takeuchi, S. Okuzumi, Radial transport of large-scale magnetic fields in accretion disks. II. Relaxation to steady states. *Astrophys. J.* **797**, 132 (2014). doi:10.1088/0004-637X/797/2/132

109. X. N. Bai, J. M. Stone, Local study of accretion disks with a strong vertical magnetic field: Magnetorotational instability and disk outflow. *Astrophys. J.* **767**, 30 (2013). doi:10.1088/0004-637X/767/1/30

110. O. Gressel, R. P. Nelson, N. J. Turner, U. Ziegler, Global hydromagnetic simulations of a planet embedded in a dead zone: Gap opening, gas accretion, and formation of a protoplanetary jet. *Astrophys. J.* **779**, 59 (2013). doi:10.1088/0004-637X/779/1/59

111. R. P. Nelson, J. C. B. Papaloizou, The interaction of a giant planet with a disc with MHD turbulence – II. The interaction of the planet with the disc. *Mon. Not. R. Astron. Soc.* **339**, 993–1005 (2003). doi:10.1046/j.1365-8711.2003.06247.x

112. M. Flock, J. P. Ruge, N. Dzyurkevich, T. Henning, H. Klahr, S. Wolf, Gaps, rings, and non-axisymmetric structures in protoplanetary disks: From simulations to ALMA observations. *Astron. Astrophys.* **574**, A68 (2015). doi:10.1051/0004-6361/201424693

113. S. A. Balbus, J. F. Hawley, A powerful local shear instability in weakly magnetized disks. 1. Linear-analysis. *Astrophys. J.* **376**, 214 (1991). doi:10.1086/170270

114. G. Lesur, M. W. Kunz, S. Fromang, Thanatology in protoplanetary discs: The combined influence of Ohmic, Hall, and ambipolar diffusion on dead zones. *Astron. Astrophys.* **566**, A56 (2014). doi:10.1051/0004-6361/201423660

115. X. N. Bai, J. M. Stone, Wind-driven accretion in protoplanetary disks. I. Suppression of the magnetorotational instability and launching of the magnetocentrifugal wind. *Astrophys. J.* **769**, 76 (2013). doi:10.1088/0004-637X/769/1/76

116. R. D. Blandford, D. G. Payne, Hydromagnetic flows from accretion disks and the production of radio jets. *Mon. Not. R. Astron. Soc.* **199**, 883–903 (1982). doi:10.1093/mnras/199.4.883

117. M. Wardle, Magnetic fields in protoplanetary disks. *Astrophys. Space Sci.* **311**, 35–45 (2007). doi:10.1007/s10509-007-9575-8

118. K. Fricke, Instabilität stationärer rotation in Sternen. *Z. Astrophys.* **68**, 317 (1968).

119. P. Goldreich, G. Schubert, Differential rotation in stars. *Astrophys. J.* **150**, 571 (1967). doi:10.1086/149360

120. H. Klahr, A. Hubbard, Convective overstability in radially stratified accretion disks under thermal relaxation. *Astrophys. J.* **788**, 21 (2014). doi:10.1088/0004-637X/788/1/21

121. W. Lyra, Convective overstability in accretion disks: Three-dimensional linear analysis and nonlinear saturation. *Astrophys. J.* **789**, 77 (2014). doi:10.1088/0004-637X/789/1/77

122. P. S. Marcus, S. Pei, C.-H. Jiang, J. A. Barranco, P. Hassanzadeh, D. Lecoanet, Zombie vortex instability. I. A purely hydrodynamic instability to resurrect the dead zones of protoplanetary disks. *Astrophys. J.* **808**, 87 (2015). doi:10.1088/0004-637X/808/1/87

123. P. S. Marcus, S. Pei, C. H. Jiang, P. Hassanzadeh, Three-dimensional vortices generated by self-replication in stably stratified rotating shear flows. *Phys. Rev. Lett.* **111**, 084501 (2013). doi:10.1103/PhysRevLett.111.084501 Medline

124. N. I. Shakura, R. A. Sunyaev, Black holes in binary-systems: Observational appearance. *Astron. Astrophys.* **24**, 337 (1973).

125. P. J. Armitage, Dynamics of protoplanetary disks. *Annu. Rev. Astron. Astrophys.* **49**, 195–236 (2011). doi:10.1146/annurev-astro-081710-102521

126. M. K. Lin, A. N. Youdin, Cooling requirements for the vertical shear instability in protoplanetary disks. *Astrophys. J.* **811**, 17 (2015).

127. N. Raettig, W. Lyra, H. Klahr, A parameter study for baroclinic vortex amplification. *Astrophys. J.* **765**, 115 (2013). doi:10.1088/0004-637X/765/2/115

128. P. S. Marcus, S. Pei, C.-H. Jiang, J. A. Barranco, Zombie vortex instability. II. Thresholds to trigger instability and the properties of zombie turbulence in the dead zones of protoplanetary disks. arXiv preprint 1605.07635 (2016).

129. L. Hartmann, N. Calvet, E. Gullbring, P. D'Alessio, Accretion and the evolution of T Tauri disks. *Astrophys. J.* **495**, 385–400 (1998). doi:10.1086/305277

130. X. N. Bai, Hall effect controlled gas dynamics in protoplanetary disks. II. Full 3d simulations toward the outer disk. *Astrophys. J.* **798**, 84 (2015). doi:10.1088/0004-637X/798/2/84

131. C. Espaillat *et al.*, in *Protostars and Planets VI,* H. Beuther, R. S. Klessen, C. P. Dullemond, T. Henning, Eds. (University of Arizona Press, Tucson, 2014), pp. 497–520.

132. A. Sicilia-Aguilar, T. Henning, L. W. Hartmann, Accretion in evolved and transitional disks in Cep OB2: Looking for the origin of the inner holes. *Astrophys. J.* **710**, 597–612 (2010). doi:10.1088/0004-637X/710/1/597

133. D. Fedele, M. E. van den Ancker, T. Henning, R. Jayawardhana, J. M. Oliveira, Timescale of mass accretion in pre-main-sequence stars. *Astron. Astrophys.* **510**, A72 (2010). doi:10.1051/0004-6361/200912810

134. L. Ingleby, N. Calvet, E. Bergin, A. Yerasi, C. Espaillat, G. Herczeg, E. Roueff, H. Abgrall, J. Hernández, C. Briceño, I. Pascucci, J. Miller, J. Fogel, L. Hartmann, M. Meyer, J. Carpenter, N. Crockett, M. McClure, Far-ultraviolet emission from circumstellar disks. *Astrophys. J.* **703**, L137–L141 (2009). doi:10.1088/0004-637X/703/2/L137

135. S. M. Andrews, J. P. Williams, Circumstellar dust disks in Taurus-Auriga: The submillimeter perspective. *Astrophys. J.* **631**, 1134–1160 (2005). doi:10.1086/432712

136. S. J. Wolk, F. M. Walter, A search for protoplanetary disks around naked T Tauri stars. *Astron. J.* **111**, 2066 (1996). doi:10.1086/117942

137. K. L. Luhman, P. R. Allen, C. Espaillat, L. Hartmann, N. Calvet, The disk population of the taurus star-forming region. *Astrophys. J. Suppl. Ser.* **186**, 111–174 (2010). doi:10.1088/0067-0049/186/1/111

138. S. J. Kenyon, L. Hartmann, Pre-main-sequence evolution in the taurus-auriga molecular cloud. *Astrophys. J. Suppl. Ser.* **101**, 117 (1995). doi:10.1086/192235

139. D. L. Padgett, L. Cieza, K. R. Stapelfeldt, N. J. Evans II, D. Koerner, A. Sargent, M. Fukagawa, E. F. van Dishoeck, J.-C. Augereau, L. Allen, G. Blake, T. Brooke, N. Chapman, P. Harvey, A. Porras, S.-P. Lai, L. Mundy, P. C. Myers, W. Spiesman, Z. Wahhaj, The Spitzer c2d survey of weak-line T Tauri stars. I. Initial results. *Astrophys. J.* **645**, 1283–1296 (2006). doi:10.1086/504374

140. B. Ercolano, C. J. Clarke, J. J. Drake, X-ray irradiated protoplanetary disk atmospheres. II. Predictions from models in hydrostatic equilibrium. *Astrophys. J.* **699**, 1639–1649 (2009). doi:10.1088/0004-637X/699/2/1639

141. J. E. Owen, B. Ercolano, C. J. Clarke, R. D. Alexander, Radiation-hydrodynamic models of x-ray and EUV photoevaporating protoplanetary discs. *Mon. Not. R. Astron. Soc.* **401**, 1415–1428 (2010). doi:10.1111/j.1365-2966.2009.15771.x

142. U. Gorti, D. Hollenbach, Photoevaporation of circumstellar disks by far-ultraviolet, extreme-ultraviolet and x-ray radiation from the central star. *Astrophys. J.* **690**, 1539–1552 (2009). doi:10.1088/0004-637X/690/2/1539

143. C. J. Clarke, A. Gendrin, M. Sotomayor, The dispersal of circumstellar discs: The role of the ultraviolet switch. *Mon. Not. R. Astron. Soc.* **328**, 485–491 (2001). doi:10.1046/j.1365-8711.2001.04891.x

144. S. K. Banerjee, J. P. Mellema, New method for determination of paleointensity from arm properties of rocks. *Earth Planet. Sci. Lett.* **23**, 177–184 (1974). doi:10.1016/0012-821X(74)90190-3

145. R. L. Hartstra, Grain-size dependence of initial susceptibility and saturation magnetization-related parameters of four natural magnetites in the PSD-MD range. *Geophys. J. R. Astron. Soc.* **71**, 477–495 (1982). doi:10.1111/j.1365-246X.1982.tb05998.x

146. R. L. Hartstra, TRM, ARM and Isr of two natural magnetites of MD and PSD grain-size. *Geophys. J. R. Astron. Soc.* **73**, 719–737 (1983). doi:10.1111/j.1365-246X.1983.tb03342.x

147. S. Levi, R. T. Merrill, A comparison of ARM and TRM in magnetite. *Earth Planet. Sci. Lett.* **32**, 171–184 (1976). doi:10.1016/0012-821X(76)90056-X

148. D. J. Dunlop, K. S. Argyle, Thermoremanence anhysteretic remanence and susceptibility of submicron magnetites: Nonlinear field dependence and variation with grain size. *J. Geophys. Res.* **102** (B9), 20199–20210 (1997). doi:10.1029/97JB00957

149. A. R. Muxworthy, E. McClelland, The causes of low-temperature demagnetization of remanence in multidomain magnetite. *Geophys. J. Int.* **140**, 115–131 (2000). doi:10.1046/j.1365-246x.2000.00000.x

150. R. S. Coe, S. Gromme, E. A. Mankinen, Geomagnetic paleointensities from radiocarbondate lava flows on Hawaii and the question of the Pacific nondipole low. *J. Geophys. Res.* **83** (B4), 1740–1756 (1978). doi:10.1029/JB083iB04p01740

151. G. A. Paterson, L. Tauxe, A. J. Biggin, R. Shaar, L. C. Jonestrask, On improving the selection of Thellier-type paleointensity data. *Geochem. Geophys. Geosyst.* **15**, 1180–1192 (2014). doi:10.1002/2013GC005135